

2009

## X-ray diffraction study of dysprosium single crystal samples in a Diamond Anvil Cell (DAC)

Ognjen Grubor-Urosevic  
University of Nevada Las Vegas

Follow this and additional works at: <https://digitalscholarship.unlv.edu/thesesdissertations>

 Part of the [Condensed Matter Physics Commons](#), and the [Mineral Physics Commons](#)

---

### Repository Citation

Grubor-Urosevic, Ognjen, "X-ray diffraction study of dysprosium single crystal samples in a Diamond Anvil Cell (DAC)" (2009). *UNLV Theses, Dissertations, Professional Papers, and Capstones*. 87.  
<https://digitalscholarship.unlv.edu/thesesdissertations/87>

This Thesis is protected by copyright and/or related rights. It has been brought to you by Digital Scholarship@UNLV with permission from the rights-holder(s). You are free to use this Thesis in any way that is permitted by the copyright and related rights legislation that applies to your use. For other uses you need to obtain permission from the rights-holder(s) directly, unless additional rights are indicated by a Creative Commons license in the record and/or on the work itself.

This Thesis has been accepted for inclusion in UNLV Theses, Dissertations, Professional Papers, and Capstones by an authorized administrator of Digital Scholarship@UNLV. For more information, please contact [digitalscholarship@unlv.edu](mailto:digitalscholarship@unlv.edu).

X-RAY DIFFRACTION STUDY OF DYSPROSIUM (Dy)  
SINGLE CRYSTAL SAMPLES IN A  
DIAMOND ANVIL CELL (DAC)

by

Ognjen Grubor-Urošević

Bachelor of Science in Physics  
Purdue University Calumet, Hammond  
2004

A thesis submitted in partial fulfillment of  
the requirement for the

**Master of Science Degree in Physics  
Department of Physics and Astronomy  
College of Sciences**

**Graduate College  
University of Nevada, Las Vegas  
December 2009**

Copyright by Ognjen Grubor-Urošević 2010  
All Rights Reserved



THE GRADUATE COLLEGE

We recommend that the thesis prepared under our supervision by

**Ognjen Grubor-Urošević**

entitled

**X-Ray Diffraction Study of Dysprosium (Dy) Single Crystal Samples in a Diamond Anvil Cell (DAC)**

be accepted in partial fulfillment of the requirements for the degree of

**Master of Science**

Physics

Lon Spight, Committee Co-Chair

Oliver Tschauner, Committee Co-Chair

Stephen Lepp, Committee Member

Davic Schiferl, Committee Member

Clemens Heske, Graduate Faculty Representative

Ronald Smith, Ph. D., Vice President for Research and Graduate Studies  
and Dean of the Graduate College

**December 2009**

## ABSTRACT

### **X-Ray Diffraction Study of Dysprosium (Dy) Single Crystal Samples in a Diamond Anvil Cell (DAC)**

by

Ognjen Grubor-Urošević

Dr. Oliver Tschauner, Examination Committee Co-Chair  
Assistant Research Professor

Dr. Lon Spight, Examination Committee Co-Chair  
Assistant Professor

University of Nevada, Las Vegas

X-ray diffraction is the basis of crystallography, the study of the structure of crystals. It uses X-rays of a wavelength on the order of the size of atoms, so it can resolve the positions of individual atoms in a crystal. Illuminating the crystal with a well-collimated X-ray beam produces X-rays diffracted in a certain direction for a specific crystal orientation. By analyzing the relative phase of the incoming and outgoing scattered X-rays, the unique arrangements of atoms can be determined and the structure of the crystal can be solved.

There is a long standing controversy regarding the crystal structures and densities of high pressure (HP) phases of rear-earth metals. Over the last couple of decades the dysprosium (Dy) structure has been obtained by polycrystalline diffraction from samples in the DACs (Diamond Anvil Cells). Due to HP powder diffraction issues of deviatoric stress and pressure gradient, the structures found are controversial. These experimental controversies have as a present consequence lack of accurate lanthanides phase diagram.

In the experimental work conducted for this thesis, dysprosium was studied using high pressure single crystal X-ray diffraction method. Single crystals of Dy were flux grown. The experiment was conducted at Advanced Photon Source (APS) synchrotron radiation beam line at Argonne National Lab (ANL). The experimental results reported were for the twinned crystal symmetry indexed in 0.7-3.8 GPa pressure region.

## ACKNOWLEDGMENTS

I would like to acknowledge late Dr. Malcolm Nicol, and my advisers: Prof. Oliver Tschauner, and Dr. David Schiferl for helping me get through a bit of peculiar and not so pleasant at times personal experience I had as a graduate student. These three individuals also provided all the needed professional guidance and direction, which allowed me to learn and excel in my work. Prof. Lon Spight's advice and guidance was crucial in navigating all the requirements in the course of my studies. Acknowledgment goes to both of my committee members: Prof. Stephen Lepp and Prof. Clemens Heske, for all of their involvement and assistance, as well as Prof. Barbara Lavina for sharing her insights and expertise. I, also, acknowledge all of my HiPSEC peers (honorable non-HiPSEC peer mention Ćelo), but especially survivors of C.F.I. group: Kozak, Boki, Rage, and Zveki. It goes without saying that all the professional and research staff of the UNLV Physics Department was instrumental in helping me complete my studies, in particular: Cara, Nataša, Gail, Amo, Jim, and Bill.

This thesis is dedicated to my family, in particular my Mom and Minha Gata, as well as two of my late friends: Pašolino and Baba Mira.

## TABLE OF CONTENTS

ABSTRACT .....	iii
ACKNOWLEDGMENTS .....	v
LIST OF TABLES .....	vii
LIST OF FIGURES .....	viii
CHAPTER 1 LANTHANIDES .....	1
Electronic and Crystallographic Structure.....	1
Equation of State .....	5
CHAPTER 2 EXPERIMENTAL SET-UP AND PROCEDURES.....	8
X-Ray Diffraction .....	8
Experimental Concept .....	9
Diamond Anvil Cell .....	11
Gasket Preparation.....	18
Ruby Pressure Scale.....	20
Sample Preparation and DAC Loading.....	22
Pr Crystal Growth .....	23
Dy Crystal Growth .....	26
X-Ray Diffraction Experimental Details.....	30
CHAPTER 3 THEORY AND DATA ANALYSIS .....	37
Crystal Lattice.....	37
The Geometry of X-Ray Diffraction.....	40
Calibration .....	44
Analysis of Pr Data .....	50
Analysis of Dy Data .....	52
Manual Indexing for the Dy Sample from 0 to 4 GPa .....	61
Manual Indexing for the Dy Sample from 6 to 9 GPa .....	64
CHAPTER 4 DISCUSSION .....	71
Diffraction Peaks Splitting.....	71
Reported Results.....	80
Results for Manual Indexing .....	80
Results for Indexing in Jade .....	85
Conclusions .....	91
Summary .....	100
REFERENCES .....	104
VITA .....	106



## LIST OF TABLES

Table 1	Crystal Systems.....	38
Table 2	Calculated Pseudo-Hexagonal Unit Cell Constants.....	64
Table 3	Ratios of Reciprocal Space Vectors .....	69
Table 4	Manual Indexing for 0.70 GPa Diffraction Pattern .....	81
Table 5	Manual Indexing for 1.74 GPa Diffraction Pattern .....	82
Table 6	Manual Indexing for 2.74 GPa Diffraction Pattern .....	83
Table 7	Manual Indexing for 3.80 GPa Diffraction Pattern .....	84
Table 8	Indexing in Jade for 0.70 GPa Diffraction Pattern.....	86
Table 9	Indexing in Jade for 1.74 GPa Diffraction Pattern.....	87
Table 10	Indexing in Jade for 2.74 GPa Diffraction Pattern.....	88
Table 11	Indexing in Jade for 3.80 GPa Diffraction Pattern.....	89

## LIST OF FIGURES

Figure 1	Flow Diagram of X-ray Experiment.....	10
Figure 2	Gasket Concept in a High Pressure Experiment .....	12
Figure 3	Schematics of Four Pin Diamond Anvil Cell (DAC) .....	15
Figure 4	DAC Backing Plates .....	16
Figure 5	Jig for Diamond Mounting.....	16
Figure 6	Assembled DAC .....	17
Figure 7	Indented Gasket.....	20
Figure 8	Ruby Fluorescence Set-Up .....	21
Figure 9	Praseodymium (Pr) Sample in DAC .....	25
Figure 10	Quartz Ampoule .....	28
Figure 11	Quartz Ampoule with Dysprosium (Dy) Crystals.....	28
Figure 12	Dy Sample Crystal.....	29
Figure 13	APS 16-ID-B Experimental Hutch.....	32
Figure 14	X-Ray Scattering in A Crystal Lattice.....	40
Figure 15	Bragg's Law.....	43
Figure 16	Silicon X-Ray Diffraction Pattern .....	45
Figure 17	FIT2D Calibrant Menu .....	46
Figure 18	FIT2D Experimental Geometry Form.....	47
Figure 19	X-Ray Beam Centering in FIT2D.....	48
Figure 20	Calibrant Two-Theta Scan in FIT2D .....	49
Figure 21	Powder Cell Display of Calibrant Two-Theta Scan.....	50
Figure 22	Pr Diffraction Pattern .....	51
Figure 23	GSE_ADA Calibration File.....	52
Figure 24	Dy Diffraction Pattern .....	53
Figure 25	Initial Dy Diffraction Peaks Choice in GSE .....	54
Figure 26	Step Scan in Omega .....	55
Figure 27	Final Dy Diffraction Peaks Choice in GSE.....	56
Figure 28	Lattice Representation in RSV .....	57
Figure 29	Initial Lattice Refinement in RSV .....	58
Figure 30	Final Lattice Refinement in RSV.....	60
Figure 31	Initial Manual Indexing of Twinned Dy Crystal.....	63
Figure 32	Dy Multi-Crystal Sample .....	65
Figure 33	Manual Indexing of Dy Multi-Crystal Sample.....	67
Figure 34	Initial Choice of Dy Diffraction Peaks for Indexing in Jade .....	72
Figure 35	Display of Dy Diffraction Peak Triplet in FIT2D .....	73
Figure 36	Two-Theta Scan of Dy Diffraction Peak Triplet in FIT2D.....	74
Figure 37	Two-Theta Scan of Dy Diffraction Peak Triplet in Jade .....	75
Figure 38	Initial Indexing of Dy Diffraction Peak Triplet in Jade .....	76
Figure 39	Group-Subgroup Lattice .....	78
Figure 40	Final Indexing of Dy Diffraction Peak Triplet in Jade .....	79
Figure 41	Manually Indexed Dy Diffraction Pattern for 2.74 GPa .....	85
Figure 42	Dy Diffraction Pattern for 2.74 GPa Indexed in Jade .....	90
Figure 43	Plot of $c/a$ vs. P for the Pseudo-Hexagonal Lattice .....	93
Figure 44	Plot of $a$ , $c$ -axes vs. P for the Pseudo-Hexagonal Lattice.....	94

Figure 45 Pseudo-Hexagonal Lattice Pressure-Volume Fit to BM3 EOS .....	96
Figure 46 Plot of $a$ , $b$ , $c$ -axes vs. $P$ for Monoclinic Lattice .....	97
Figure 47 Plot of $\beta$ vs. $P$ for Monoclinic Lattice.....	97
Figure 48 Monoclinic Lattice Pressure-Volume Fit to BM3 EOS.....	99

## CHAPTER 1

### LANTHANIDES

#### Electronic and Crystallographic Structure

The lanthanides, lanthanum (La) to lutetium (Lu), are members of transition group IIIA within the Periodic Table. The ground-state electronic configurations for scandium (Sc) - argon core +  $3d^14s^1$ , yttrium (Y) - krypton core +  $4d^15s^2$ , lanthanum (La) - xenon core +  $5d^16s^2$ , and actinium (Ac) - radon core +  $6d^17s^2$ , indicate that the elements usually listed in the IIIA group are the first members of the four *d*-type transition series. After scandium and yttrium, electrons are added, respectively, to the  $3d$  and  $4d$  levels, resulting in the elements of the first transition metals series, from scandium to zinc, as well as the second transition metals series, from yttrium to cadmium. However, after lanthanum the energy of the  $4f$  level falls below that of the  $5d$  level, and the subsequent electrons are added to the inner, shielded  $4f$  orbitals. There are seven such orbitals, each with a capacity of two electrons; a total of fourteen elements of this inner or *f*-type transition series may result before the  $5d$  orbitals can fill again regularly. Although it is implied that the  $4f$  orbitals are occupied regularly, observation showed that this is not exactly right [1]. Instead, there is a distinct tendency for the *f* orbitals to be occupied in preference of maintaining  $4f^n5d^1$  arrangement. This tendency is due to increased electronic stability associated with complete single,  $4f^7$  or complete double,  $4f^{14}$  occupancy of any set of orbitals. Therefore, the  $4f^7$  and  $4f^{14}$  arrangements are achieved per Hund's rules, in the series with europium and ytterbium. Whether the fundamental configuration is  $4f^n5d^16s^2$  or

$4f^{n+1}6s^2$  is of no chemical significance, since the energy differences between the  $4f$  and  $5d$  bands are too small to alter many chemical properties, ranging from 0.01 eV for lanthanum to 0.32 eV for lutetium [1, 2, 3].

The size of atoms and ions are determined both by nuclear charge and by the number and degree of occupancy of electronic shells. Ergo, among either the metals Sc, Y, and La or the ions  $Sc^{3+}$ ,  $Y^{3+}$ , and  $La^{3+}$  there is a steady increase in size along with an increase in atomic number, reflecting the fact that addition of electrons to higher and higher energy levels overcomes increasing contractive effects that result from the enhanced attraction produced by the larger nuclear charge. But in the series La-Lu, or  $La^{3+}$ - $Lu^{3+}$ , a general decrease in size with an increase in atomic number results because addition of electrons to the shielded  $4f$  orbitals cannot compensate for the effect of increased nuclear charge. A similar but more limited trend characterizes the non-trivalent cations, like  $Sm^{2+}$ ,  $Eu^{2+}$ ,  $Tm^{2+}$ ,  $Yb^{2+}$ ,  $Ce^{4+}$ ,  $Pr^{4+}$ , and  $Tb^{4+}$  [4]. These decreases are known as the *Lanthanide Contraction*.

At room temperature and pressure, elements from gadolinium to lutetium (with exception of ytterbium) assume the hexagonal close-packed structure with AB, AB, etc. stacking sequence [1]. Lanthanum, praseodymium, neodymium, and promethium assume the double hexagonal structure with the stacking sequence ABAC, ABAC, etc [1]. Cerium and ytterbium have face-centered cubic structure with ABC, ABC, etc. stacking sequence [1]. The structure of samarium is rhombohedral with stacking sequence ABABCBCAC, ABABCBCAC, etc [1]. Europium has the body-centered cubic structure [1]. This structure is more open

than the other four close-packed structures mentioned, so the europium structure is not related to the other lanthanides close-packed structures.

Except for cerium, europium, and ytterbium, the regular rare earths (lanthanides and yttrium) show a common sequence of structural transitions with increasing pressure at room temperature: hexagonal close-packed (hcp) -> Sm-type -> double-hexagonal close-packed (dhcp) -> face-centered cubic (fcc) -> distorted fcc (d-fcc) [4]. The first four phases are all close-packed and represent stacking variants of hexagonal layers such as the ABC, ABC, etc. versus AB, AB, etc. order in fcc and hcp, respectively. There has been considerable discussion about the last phase [1, 3, 5, 6]. All or the later part of this general phase sequence is observed under pressure in each of the regular rare earths. The valence electrons in these metals may be viewed as being compressed either by the applied pressure or by reducing the atomic number at fixed pressure. So, the lighter members of the series enter into the generalized sequence at successively later points for ambient pressure room temperature phases: hcp (gadolinium), Sm-type (samarium), dhcp (promethium, neodymium, praseodymium, and cerium). The close-packed and relatively high symmetry structures of the regular rare earth sequence are contrasted to the low symmetry and open-packed structures seen at pressures just above the volume-collapse transition in praseodymium (orthorhombic alpha-Uranium structure, 9% collapse above 20 GPa) and gadolinium (body-centered monoclinic, 11% collapse above 59 GPa). Cerium also exhibits isostructural fcc -> fcc (same structure on both sides of the phase transition) volume-collapse (15% collapse above 0.9 GPa) [7].

Many of the trivalent rare earth metals undergo a dramatic transformation in physical properties under compression, which is generally believed to arise from a change in the degree of  $4f$  electron correlation [8]. The  $f$  electrons participate in the crystal bonding in the compressed, more weakly correlated regime, but not at larger volumes where correlation effects are more dominant. *Duthie and Pettifor* showed that in the regime where correlation effects dominate, lanthanide structures are controlled by the electron occupancy of  $d$  level [9]. The terms itinerant and localized, respectively, are commonly used to describe the differing  $f$  electron behavior in these two regimes.

Theoretically, it is hard to correctly predict the actual atomic arrangement a specific element adopts once it forms a solid. To predict this in metals, as well as non-metals, the density functional theory (DFT) is used [5]. The problem of dealing with a system of  $N$  interacting electrons in an external potential  $V(r)$  is expressed by the  $3N$ -dimensional Schrödinger equation for the wave-function  $\Psi(r_1, r_2, \dots, r_N)$ . DFT treats this problem in terms of the electronic density distribution,  $n(r)$  and a universal functional of the density  $E[n(r)]$ . The problem of approximately solving the many electron Schrödinger equation is replaced by the problem of finding sufficiently accurate approximations to  $E[n(r)]$  and then solving appropriate single electron equations. Although the DFT calculations are used in investigating the rare earth elements, it remains particularly challenging to predict correct structures of rare earths under compression [7]. As mentioned, some rare earths under compression undergo a large volume collapse at phase transition, when compared to normal crystalline phase transitions in metallic

systems. These changes involve the nature of the  $f$  electrons and their transformation between localized non-bonding magnetic moments and strong metal bonds. DFT is unable to treat the strong electron correlation that takes place during the change in behavior of the  $f$  electrons from localized to itinerant.

Almost all lanthanides have been studied for the last twenty years by means of high pressure X-ray diffraction [10]. But different experimenters have reported sharply different findings on transition pressures and phase identity [4]. This is due to the kinetics of the transitions among the various lanthanide phases. Also, powder X-ray diffraction, which is used to identify different crystal structures under pressure, has limitations (the limitations of the powder diffractions are discussed in CHAPTER 2) that are the cause of substantial disagreement in reported transition densities [11]. Hence, presently, an accurate lanthanides phase diagram is not formulated.

### Equation of State (EOS)

The thermodynamic state of a system is usually defined by three variables: absolute temperature  $T$ , pressure  $p$ , and specific volume  $V$ . Only two of these variables are independent, since there is a functional relationship between  $T$ ,  $p$ , and  $V$ : the equation of state (EOS). An equation of state is one of the most important characteristics of a material [2].

EOS data provides a link between macroscopic thermodynamic descriptions of the materials and microscopic quantum mechanical models [6]. A system with a fixed number of particles  $N$  confined to a volume  $V$  in thermal equilibrium



characterized by the temperature  $T$  has all static thermodynamic equilibrium properties incorporated in the partition function  $Z$ :

$$Z(V, T, N) = \sum_n e^{\left(\frac{-E(n)}{kT}\right)} \quad (1)$$

where  $E(n)$  is a particular energy of a corresponding quantum state described with set of quantum numbers  $n$ . Once  $Z(V, T, N)$  is known, the free energy  $F(V, T, N)$  of a system can be obtained:

$$F(V, T, N) = -kT \ln Z(V, T, N) \quad (2)$$

Formula (2) allows the possibility of calculating the thermodynamic variables and functions for the system where discrete energy levels are known. For instance:

$$\text{the entropy: } S = -\left(\frac{\partial F}{\partial T}\right)_{V, N}$$

$$\text{the pressure: } p = -\left(\frac{\partial F}{\partial V}\right)_{T, N}$$

$$\text{the chemical potential: } \mu = \left(\frac{\partial F}{\partial N}\right)_{V, T}$$

$$\text{internal energy: } E = F + TS$$

$$\text{enthalpy: } H = F + TS + pV$$

$$\text{Gibbs energy: } G = F + pV \quad (3)$$

Since  $F(V, T, N)$  with  $V$ ,  $T$ , and  $N$  thermodynamic variables offers a complete thermodynamic description of the system, it is considered the “thermodynamic potential” of the system. Similarly, with respect to their different thermodynamic variables  $E(V, S, N)$ ,  $H(p, V, N)$ , and  $G(p, T, N)$  are thermodynamic potentials, that also determine by their partial derivatives all the other thermodynamic variables. Nevertheless,  $p(V, T, N)$  alone gives only an incomplete description of the system, since partial integration of  $p dV$  doesn't determine the part involved in the integration for the entropy,  $S dT$ . Similarly  $E(V, T, N)$  provides an incomplete characterization of the system, missing the term:  $\left(\frac{\partial S}{\partial V}\right)_{T,N}$ . This term could only be determined if:

$$p(V, T, N) = -\left(\frac{\partial E}{\partial V}\right)_{T,N} + \left(\frac{\partial S}{\partial V}\right)_{T,N} \quad (4)$$

would be known in addition.

This incomplete characterization of a thermodynamic system in general is considered an “equation of state”. Historically [12], the distinction was made between thermal (TEOS) and caloric (CEOS) equations of state referring to  $p(V, T, N)$  and  $E(V, T, N)$  respectively. Recently, [13, 14, 15] the term EOS is restricted in its meaning to the  $p$ - $V$ - $T$  relation.

## CHAPTER 2

### EXPERIMENTAL SET-UP AND PROCEDURES

#### X-Ray Diffraction

The objective of an X-ray diffraction experiment is to determine the structure of a material and for a crystalline material this means determining the unit cell parameters, the unit cell symmetry, and the precise location of all of the atoms or molecules in the unit cell. In broad terms, the size and symmetry of the unit cell are found by determining the position of the Bragg peaks, while the nature of the basis and the position of the atoms or molecules within the cell determine the Bragg peak intensities. Depending on the circumstances, the crystalline material could either be in the form of a single crystal or a powder.

Single crystal X-ray diffraction allows solving the structures with more confidence than powder X-ray diffraction because single crystal X-ray data represent the three-dimensional reciprocal space, as opposed to powder diffraction, in which the three-dimensional reciprocal space is mapped in one dimension. Thus, there is a strict overlap of Bragg reflections at the same  $2\theta$  angle, as well as an effective overlap of reflection separation by a narrow  $2\theta$  increment, which is experimentally not resolved. Also, powder diffraction is based on a sample that has a fully random distribution of crystallites of equal size. If the poly crystalline aggregate is strained, there is a deviation from random distribution (texture), which affects the intensity of Bragg peaks and more importantly, the corresponding peak shape; this in turn causes an incorrect solution to crystal symmetry and unit cell constants. The issue of texture

occurring in the poly crystalline aggregate is not present in the single crystal sample, due to a single specimen used. Moreover, the powder diffraction limitations discussed play a great role in the equation of state (EOS) controversies for the Lanthanides, as the calculations of EOS for all of the elements of the Lanthanide family is done from volumes (densities) obtained from unit cell parameters acquired by powder diffraction [2].

### Experimental Concept

In this work crystal structure analysis is based on an X-ray diffraction experiment. The single crystal samples were grown either by flux method or by laser annealing. The sample is compressed in a diamond anvil cell (DAC) and placed in an X-ray beam to generate a diffraction pattern, which is recorded by an area detector. The steps of single crystal experimental procedure done for this thesis are given in the flow diagram in Figure 1, next page. The details of the experimental procedure steps are discussed in the following sections of this chapter.

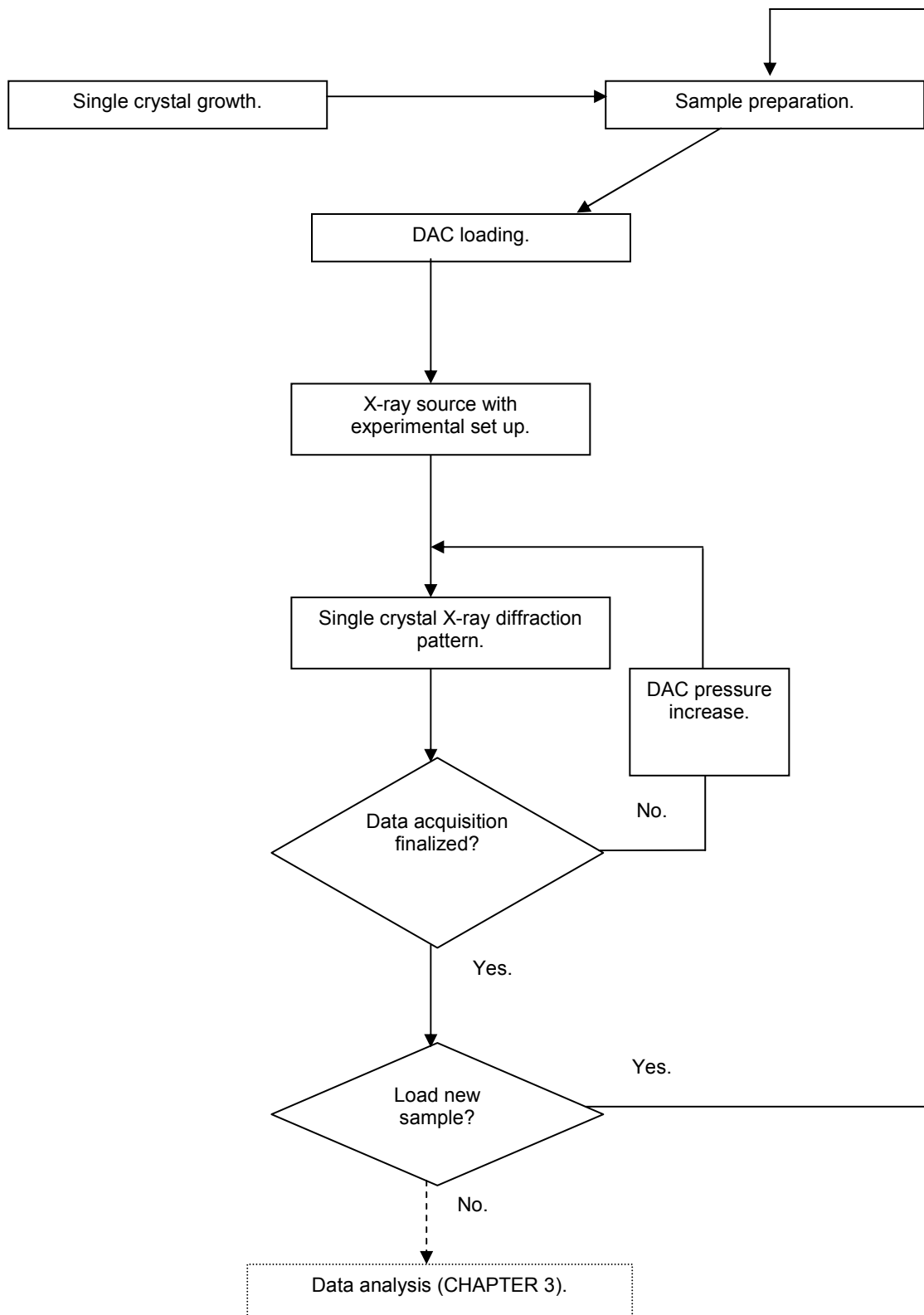


Figure 1. Flow diagram of the single crystal X-ray diffraction experimental procedure implemented in this thesis.

## Diamond Anvil Cell

In the thesis work, diamond anvil cells were used to pressurize praseodymium (Pr) and dysprosium (Dy) samples. The idea of high-pressure devices used in X-ray crystallography is rather simple and was introduced by Jamieson *et al.* (1959) from the University of Chicago for high-pressure (HP) X-ray powder diffraction studies, and independently by Weir *et al.* (1959) at the National Bureau of Standards (USA) for infrared absorption measurement. The principle was the compression of a sample between two diamond anvils. Pressure is defined as the force applied per given area. Thus, to increase pressure, the force being applied should be increased, or the area on which force is applied should be decreased. Therefore in a DAC, by exerting a large amount of force on a small diamond anvil area, the net pressure equivalent the pressures at Earth's center [2], might be obtained.

Diamond is used in DAC, because it is the hardest material with the highest plasticity limit. Therefore the diamond anvils can sustain extreme pressures of up to 350 - 450 GPa [2]. Diamond has the important property of being transparent to most of the spectrum of electromagnetic radiation, including  $\gamma$ -ray, X-ray, part of ultraviolet (230+ nm), visible, and most of the infrared region. Because of diamond transparency, the sample may be examined *in situ* (inside DAC), at elevated pressure using various techniques including optical microscopy, Raman, Infrared, Brillouin spectroscopy, and X-ray diffraction. There are two types of diamonds used in DACs: type I and II. In this experiment only type I diamonds were used. Type I diamonds have an inclusion of Nitrogen

impurities that are trapped in a crystal during the growth giving these type of diamonds an observable yellow hue. The anvils used in DACs are diamonds of different cuts: brilliant, regular, Bohler – Almax, etc., ranging in mass from 0.2 to 0.5 carats, where 1 carat = 200 milligrams [16]. The anvils tips are removed to allow for the culets of certain diameters, usually from 0.1 mm to 1 mm.

As previously noted, only powder samples were suitable for use in DACs at first, because the single crystal samples could be destroyed between diamonds. A revolution in high-pressure DAC use happened due to introduction of a metal gasket between diamond anvils (Van Valkenburg, 1965). Some of the suitable materials for gaskets are: Inconel X750, tempered stainless steel, Rhenium, etc. To prepare the gasket, a metal foil is placed between the flat surfaces of the anvils and the opposite anvils are tightened to obtain a footprint of the needed thickness on the foil. A hole, drilled at the center of the indentation made by the anvil face, forms a high-pressure chamber for a sample, Figure 2.

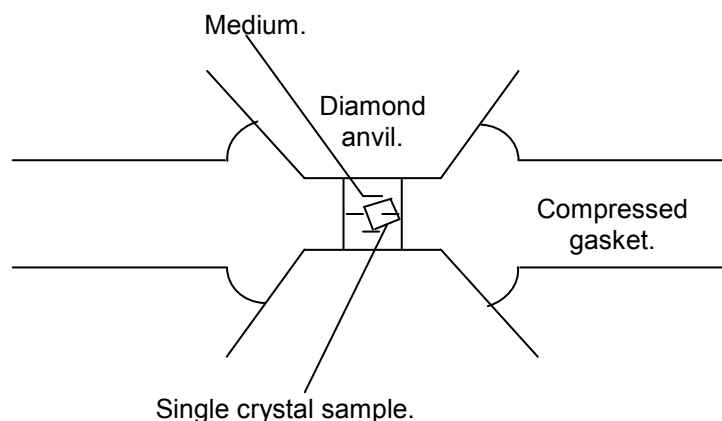


Figure 2. Metal gasket compressed between anvils with a sample in the high-pressure chamber.

In a DAC, the gasket is set on a flat top (culet) of the lower diamond in the same orientation it had when indentation was made. The hole is filled with a hydrostatic medium (methanol-ethanol, neon, etc). The single crystal is placed on the upper anvil. By placing the upper anvil on the gasket the single crystal is placed in a hole and the hole is sealed. Thus the hole filled with the medium forms a small, high-pressure chamber. The opposing anvils, pushed by a force towards each other, deform the gasket, thereby reducing the volume of the hole and generating pressure inside the chamber. The gasket also serves to contain the pressure medium and being extruded around the diamonds, acts as a supporting ring preventing failure of the anvils, due to concentration of stresses at the edges of the anvil culets.

There are several constructions of the DACs, which differ by mechanisms for generating the load. Regardless of a DAC type, the load must be applied gradually and uniformly. For the proper transfer of the load from anvils to a sample, the diamond alignment plays the main role. The diamond anvils must stay coaxial and parallel during loading to avoid either complete destruction of the gasket or cracking of the anvils.

In this study, the so called "Four Pin" DAC was used because it provided an optical aperture sufficiently large for single crystal X-ray diffraction experiments. In some cases a couple of different cell types were also used: long and short piston and Merrill and Bassett [15]. Experiments done with these cells are not a part of the thesis. The Four Pin cell was designed by Prof. Oliver Tschauner and



machining of the cell body was done at the UNLV Physics Department machine shop.

The schematic and operating principle of the Four Pin cell is given in Figure 3, page 15. The body is made from Vascomax 300, a tough, precipitation-hardened steel. This cell features a central conical aperture of  $70^\circ$ , which is reduced by the aperture of the gasket hole and the thickness of the diamond anvils. For standard design anvils the angular access to the sample is  $30^\circ$  and for Boehler – Almax anvils it is  $64^\circ$ . The cell allows for tilt and translation adjustment of the anvils. Upon loading the two parts, the top and bottom of the cell are guided by hard steel posts. The top and bottom part of the cell contain the backing plates. The top plate has tilt adjustment via axial seat holder, while the bottom plate has translational adjustment via set screws, used in aligning anvils. The plates bottom opening or optical aperture, provides optical, as well as X-rays access to a sample inside the gasket chamber. The anvils are seated and glued by an epoxy resin to the backing plates. The mechanical load in the cell is generated by a set of drive screws, Allen cap type.

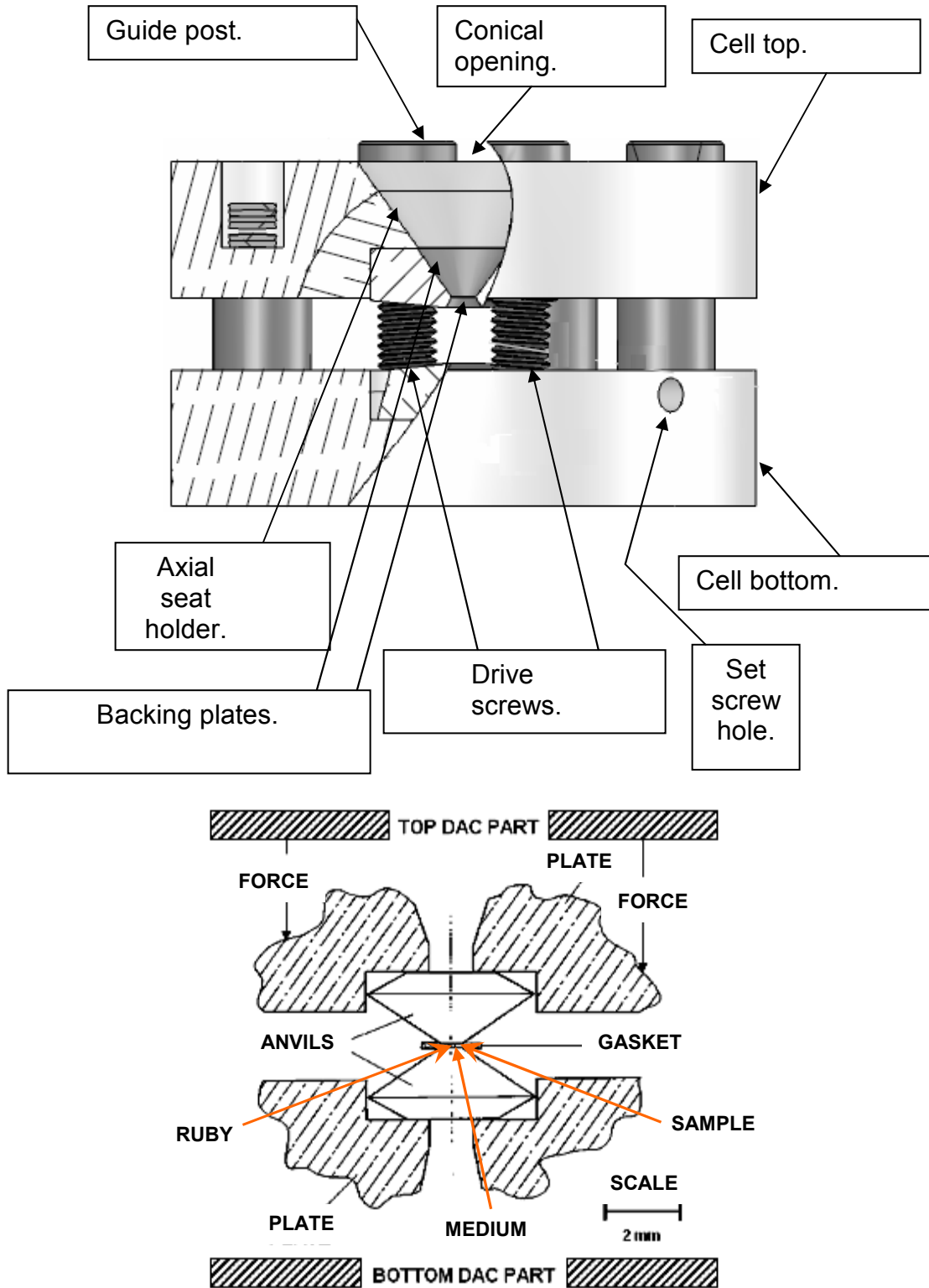


Figure 3. Top: The “Four Pin” Cell drawing, without the diamond anvils. Courtesy of Jim Norton, UNLV physics department machine shop. Bottom: vertical cross-section of the anvils, gasket, and sample chamber in the cell.

For the experiments, the Boehler – Almax (B-A) anvils with 300+  $\mu\text{m}$  diameter culets and 3 mm diameter of a surfaces parallel to anvils, or tables are used. These dimensions correspond to 0.2 carat standard cut of the anvil. Thus, load on the backing plate is multiplied by a factor of ten [16]. The backing plate pressures, generated by the mechanical load, ranged up to 2 GPa. The anvils are mounted and inserted in the cone of the seat on the carbide backing plates. The schematics of backing plates are shown in Figure 4.



Figure 4. Left: bottom backing plate. Right: top backing plate. Drawings courtesy of Jim Norton.

The anvils are adjusted in the seats by a diamond jig, Figure 5. The jig allows for minimizing tilt of B-A anvils mounted on the backing plates. The adjusted anvils are fixed by Stycast 300 epoxy resin to the backing plate.



Figure 5. Disassembled diamond jig.

Before the sample is loaded, the Four Pin cell, shown in Figure 6, is aligned. To align the DAC, touching culets should have coaxial and parallel overlap.



Figure 6. Top picture - Front left: Four pin DAC, bottom part with the Re gasket covering the bottom culet. Front right: Four pin DAC, top part with top culet. Rear left and right: Load screws with Belleville washers. Bottom picture – Assembled DAC.

Both culets were cleaned with Kim wipes dipped in ethanol. The bottom part of the cell is placed on a microscope stage with transmitted lighting. The cell's top part, under the microscope objective, was slid down the guide pins, until the culets touched. One of the culets was covered by a thin film of grease, thus protecting the anvils from direct contact prior to alignment. Once the culets approached a point of contact, any signs of misalignment are checked under the microscope. The misalignment could be either lateral (culets not coaxial) indicated by asymmetric overlap edge to edge or tilt (culets not parallel) indicated by Newtonian fringes in the thin gap between the anvils. Set screws, which move the bottom backing plate, are used to rectify lateral misalignment. Tilt is corrected by four vertical screws, which retain the axial seat holder that houses top backing plate.

### Gasket Preparation

First the gasket, 6 by 6 mm<sup>2</sup> square and 300 μm in thickness, is cut from the sheet of Re. Re gasket is a material of high enough strength allowing for sufficient sample chamber height and exhibiting enough elastic yields under load to allow for elastic bending of the anvils. The gasket is cleaned with ethanol. It is put over the bottom anvil, leveled with and touching the culet. The gasket is kept in place with dental wax. A small notch in the gasket is aligned with a similar mark on the body of the cell bottom. This is done in order to retain initial position of the gasket whenever the gasket is placed on the anvils. The cell is closed, with the culets separated by the gasket. Upon closing, the load screws with the

washers are tightened by hand. The screws were turned once with hex keys about  $\frac{1}{16}$  th of a turn. This applied a pressure of about  $\frac{1}{5}$  th of a GPa to a gasket<sup>1</sup>. Applying this pressure causes a shallow indentation to the gasket. Next the cell is opened and using the tip of a needle, ruby chips are put inside the indentation. The cell was closed again and the screws are again tightened by hand. The screws were turned with hex keys and pressure in the cell is ramped up until the pressure reached ~12+ GPa, which translated to the gasket pre-indent of ~70+  $\mu\text{m}$ . After every half a turn of the screws, the pressure inside the cell was checked by the ruby fluorescence (ruby pressure scale is explained in the next section). Afterward, the gasket was removed from the cell and the thickness of the indent was measured with a micrometer. The set of pictures in Figure 7, page 20 shows increasing gasket indentation, as the pressure was ramped up in the cell.

The gasket was put in an ethanol bath and cleaned ultrasonically for a few minutes. A process of shaping the object using electrical discharges was used to drill through the center of the gasket indent to make a pressure (sample) chamber. An electric discharge machine (EDM) from Hylozoic Products was used. Gasket holes of 150 – 170  $\mu\text{m}$  in diameters were drilled.

---

<sup>1</sup> The connection of a number of turns to a pressure generated in GPa is found by trial and error.

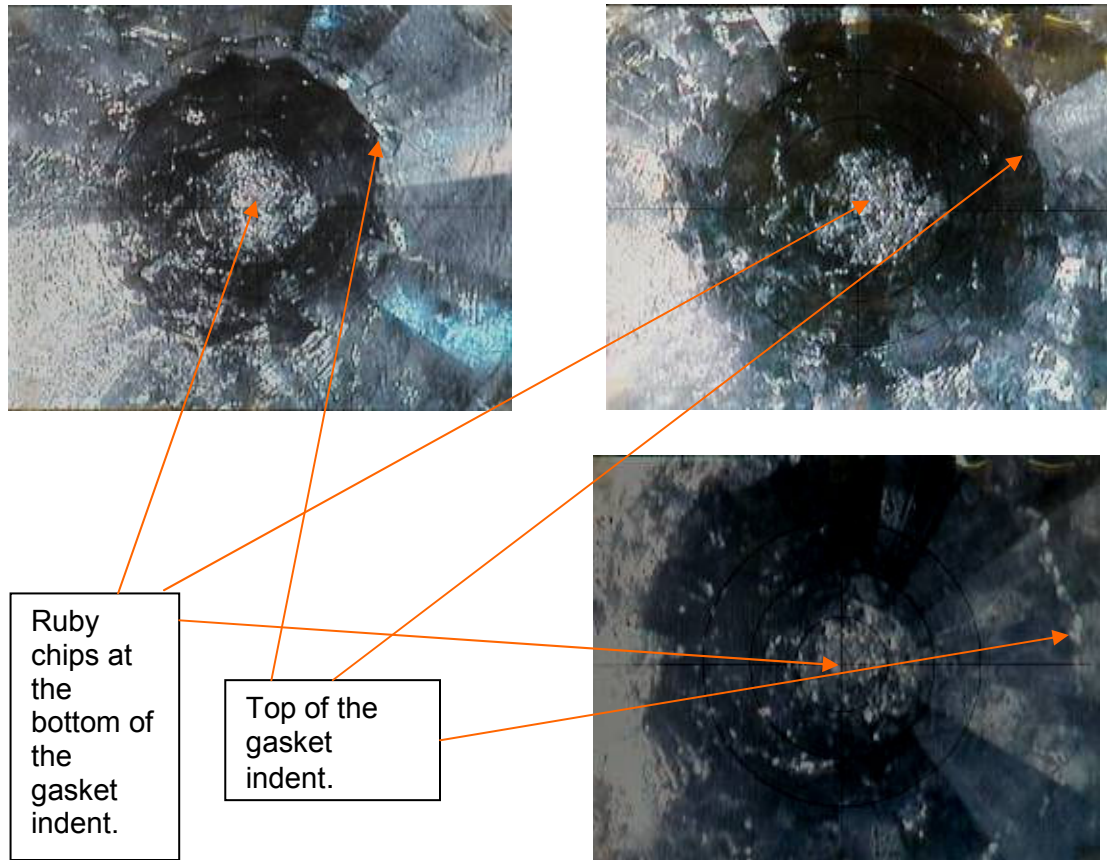


Figure 7. Images from left to right clockwise: The first image is the gasket indentation at ~2+ GPa, the second image is the gasket indentation at ~5+ GPa, and the third image is the gasket indentation at ~12+ GPa. The indentations are seen through the top diamond anvil.

### Ruby Pressure Scale

The ruby gauge is commonly used for pressure determination. Barnett *et al.* (1973) and Piermarini *et al.* (1975) introduced the ruby gauge, which was calibrated against the Decker equation of state for NaCl up to 19.5 GPa. Barnett and Piermarini found that the wavelength of the ruby fluorescence shifted linearly from the normal atmospheric pressure. The shift in pressure is almost linear with  $d\lambda/dP = 0.365(9) \text{ nm GPa}^{-1}$  [17]. In the ruby fluorescence method, pressure is

measured through the wavelength position of a ruby fluorescence emission of  $R_1$  and  $R_2$  lines, excited by absorption of laser lines of suitable wavelength. The  $R_1$  and  $R_2$  ruby fluorescence emission lines have respective wavelengths of 694.25  $\mu\text{m}$  and 692.74  $\mu\text{m}$  at ambient pressure and temperature [3]. These emissions are very narrow, with a high fluorescence quantum yield and maintaining these characteristics with increasing pressure. The advantage of using the ruby fluorescence technique to determine pressures is that the ruby crystal used for these measurements is up to  $\sim 20$  microns in size and thus occupies a very small proportion of the limited pressure chamber volume in a DAC and contributes little diffracted intensity. The set up used to measure pressure in DAC using the ruby crystal fluorescence, is shown below in Figure 8, below.

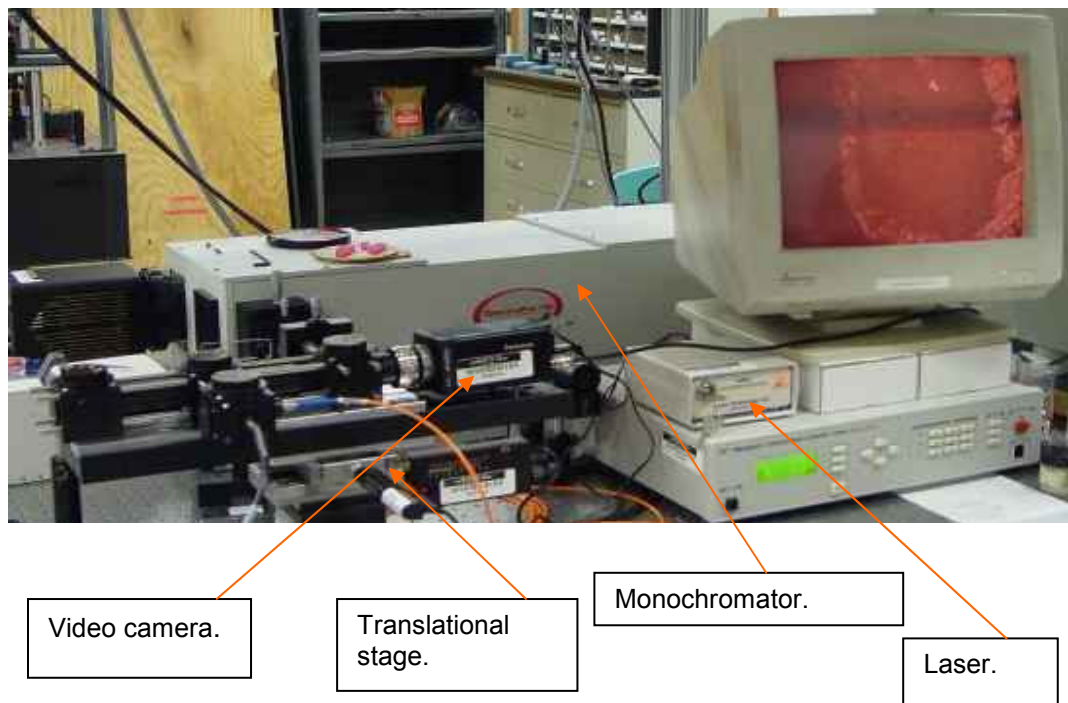


Figure 8. Instrumental set up for the measurement of a pressure in DAC by ruby fluorescence.



The excitation source is a 404 nm diode laser. Excitation light is brought to the sample by a series of optical fibers, beam splitters and mirrors. The sample in a DAC is located with white-light source and a Panasonic video camera display. The fine alignment and focusing on the sample is done remotely with x, y, and z translational stages. Ruby emission is collected and filtered using an optical fiber connected to a 0.75 m Acton 750i single monochromator with a 1200 lines per mm grating. The emission is recorded by a Princeton Instruments 5 stage thermoelectrically cooled CCD camera with 512 x 2048 pixels<sup>2</sup> resolution. The fluorescence wavelength shift is analyzed by WinSpec software.

#### Sample Preparation and DAC Loading

Commercially available Pr and Dy powder samples, 99.9% purity each, from Alpha Aesar and Sigma – Aldrich are initially used. The first step in the sample preparation was to try to grow a single crystal(s) sample from the crystalline powder, for each element. The crystal growth for Pr was done in situ, i.e. in the DAC, while under high pressure. The Dy crystal growth is accomplished through a flux growth of two solids inside the quartz tube at ambient pressure. The chemical analysis of the powder samples is done with an electron microprobe analyzer (EMPA) or electron microprobe (EMP). An EMPA is an electron micro beam instrument used for the non-destructive chemical analysis of solid samples down to 1  $\mu\text{m}$ . It operates under the principle that if a solid material is bombarded by an accelerated and focused electron beam, the incident electron beam has sufficient energy to cause emission of the X-rays characteristic of the

element analyzed. X-rays generated by electron interactions do not lead to volume loss of the sample, so it is possible to re-analyze the same materials more than once. The sample chemical composition is tested using JOEL JXA Superprobe 8900 probe at the UNLV Electron Microanalysis and Imaging Lab (EMIL) [18]. The powder sample is flattened into a  $\sim 30 \mu\text{m}$  rectangular section. The sample is polished to avoid the interference of surface imperfections with electron-sample interaction. To avoid electrical charging of the sample under the direct electron beam, the sample is coated with a thin film of carbon. The operating conditions for EMPA were: 20 keV accelerating voltage, a 10 nA beam current, and a  $5 \mu\text{m}$  beam. The sample is probed by a beam and X-rays are generated. A single wavelength X-rays are selected using an analytical crystal with specific lattice spacing. These X-rays are reflected from a crystal into a spectrometer where characteristic X-ray peak intensity is counted for 30 seconds. This sample characteristic X-ray peak is compared with the standard characteristic X-ray peak profiles. The standards used were synthetic rare earth phosphates, like  $\text{DyPO}_4$ ,  $\text{CePO}_4$ ,  $\text{PrPO}_4$ , etc. Comparing absorption corrected intensity profiles of X-ray peaks of the phosphates and the sample, the atomic weight percentage of the standard in the sample can be found.

### Pr Crystal Growth

Cunningham *et al.* [19] showed that the pressurized Pr powder sample in DAC transforming to alpha-uranium ( $\alpha\text{-U}$ ) phase exhibited multi crystal growth. Also, Baer *et al.* [20] reported a Pr phase diagram that indicated that a

polycrystalline sample, after undergoing  $\alpha$ -U phase transition at 23 GPa and high temperature (above  $\frac{1}{3}$  of the Pr melting temperature), showed a tendency to anneal along several preferred orientations. Therefore, the Pr crystal growth is attempted *in situ* from the Pr powder sample at the pressure and temperature of the  $\alpha$ -U phase. The potassium bromide (KBr) sample of 99.9% purity from Alpha Aesar was used as a pressure medium. A KBr crystal is picked with the needle tip and before it is loaded in the pressure chamber, the crystal size is checked under the microscope. If the crystal is slightly longer than the diameter of the sample chamber it is put over the sample chamber. Then, the cell is closed and the top anvil plastically deforms and packs the crystal into the sample chamber. Afterwards, the cell is opened and the sample chamber is checked under the microscope. If the chamber is filled with KBr throughout, a shallow indent with the needle tip is bored in KBr filling. A Pr crystallite, anywhere from 20+ - 50+  $\mu\text{m}$  in length is placed in the indent. An annealed ruby sphere [14] of 10 - 20  $\mu\text{m}$  in diameter is placed few microns outside the indent in the KBr filling. A thin plate of KBr of  $\sim 15$   $\mu\text{m}$  thickness, prepared in a separate DAC, is placed on top of the KBr filling. Upon closing the cell, the KBr is deformed plastically and uniformly encapsulates both the Pr sample and the ruby. The pressure is gradually increased and checked with ruby fluorescence. The sample is pressurized just over the reported pressure value for a phase transition. The cell is checked again under the microscope, Figure 9, next page.

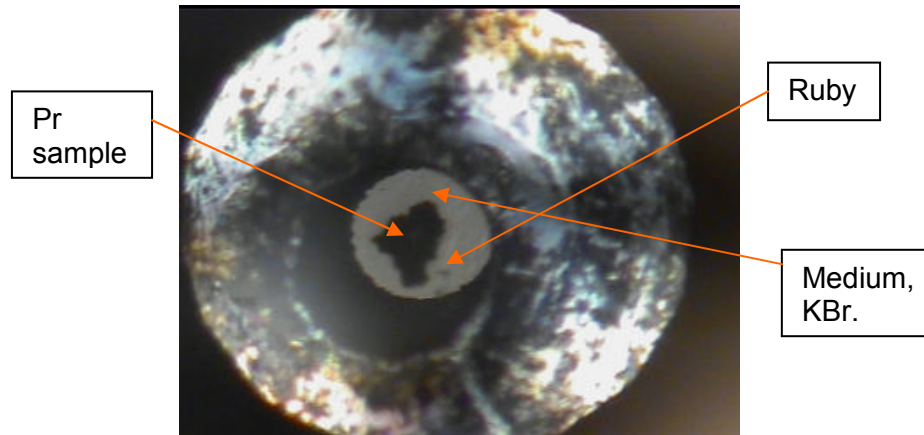


Figure 9. Pr sample in KBr medium at 4 GPa. This is a view under microscope through the diamond anvil. Conical light convergence is due to lens effect of culet strain.

Next, the wax stabilizing the gasket is removed with the needle and the sample is annealed at  $\alpha$ -U phase pressure in DAC. To generate the high temperature needed to grow Pr crystals *in situ*, direct CO<sub>2</sub> laser heating is used. In order to heat the Pr sample efficiently with a minimal temperature gradient, the laser beam is defocused. The sample, embedded in a non-transmitting heat pressure medium allowed for insulation from heat sinks like DAC anvils and gasket. A few different heating temperatures and rates of cooling are tried for annealing samples in the DACs. In one heating experiment the sample was heated until it radiated  $\sim 2300$  K for a couple of minutes, then it was cooled down at a rate of  $\sim 100$  K for 30 seconds until the sample reached a temperature of 1300 K. Finally, the laser is gradually turned off and the sample is cooled down at the same rate. In another experiment the sample was heated and kept at  $\sim 600$  K for an hour, after which it was cooled down at a rate of  $\sim 100$  K per

minute. In the final experiment, the sample was heated to ~2500 K for a minute and quenched with a rate of cooling of ~100 K per minute. Once the sample annealing is done, integrity of the sample chamber is checked under the microscope and the sample pressure is measured.

### Dy Crystal Growth

When melting solids together, complete mixing of insoluble phases occurs and recrystallization takes place in the subsequent cooling of the melt.

Crystallization of melts is a valuable method for growing single crystals since, in the presence of the liquid phase and in the absence of too many crystal nuclei, large crystals grow readily. In order to employ crystallization from melt, knowledge of the relevant eutectic phase diagram is necessary, since the phase diagram provides a diagrammatic representation of the conditions of temperature and composition of crystal growth. Dy melts at 1412° Celsius [1], but crystals can be grown in eutectic systems at much lower temperatures. The melting point of a mixture of two or more solids depends on the relative proportions of its phases. An eutectic is a mixture of two or more immiscible or only partially miscible phases at a composition that has the lowest melting point and where the phases simultaneously crystallize at this temperature.

Flux method crystal growth in a simple binary eutectic system A-B is consisting of mixing two immiscible solids, heating them up and cooling with the idea of growing crystals of solid A in a flux of the solid B. The effect of adding a certain amount of solid B used as a flux is to drastically reduce the melting

temperature of solid A and to cause melting to occur over a range of temperatures. The melting of the A-B mixture is going to happen from the eutectic temperature and is not complete until a temperature is reached where A-B mixture is partially melted. Hence, over the range of these temperatures, the partially melted mixture contains crystals of A and a liquid which composition changes with temperature. In order to obtain crystals of A, the mixture may be cooled slowly through the temperature range. While cooling to an ambient temperature, the remaining liquid crystallizes to give a fine grained eutectic structure containing small crystals of A and B. Embedded in the eutectic structure are the larger crystals of A that grew as the primary phase at high temperature.

The flux growth of Dy crystals is done in potassium chloride (KCl) flux. The 770° C melting point of KCl [1] allows for a sufficiently lower eutectic point of the binary system, so the Dy crystals flux growth could be done in a commercial grade furnace. KCl powder of 99.9% purity is purchased from Alfa Aesar. Because the binary eutectic phase diagram for A-B system, where A = Dy and B = neutral salt, could not be found in the literature, the flux growth is done for a few different mixes of Dy and KCl. Dy and KCl were mixed with a pestle and mortar. The total weight of the mix was kept at 100 mg, while varying the contribution of Dy by weight in 0.50, 0.33, 0.25, 0.20, and 0.17 parts. The binary mix is placed in the evacuated and argon-filled quartz tubes from Technical Glass Co. The tubes are sealed with a propane/oxygen torch. One such tube is shown in Figure 10, next page.

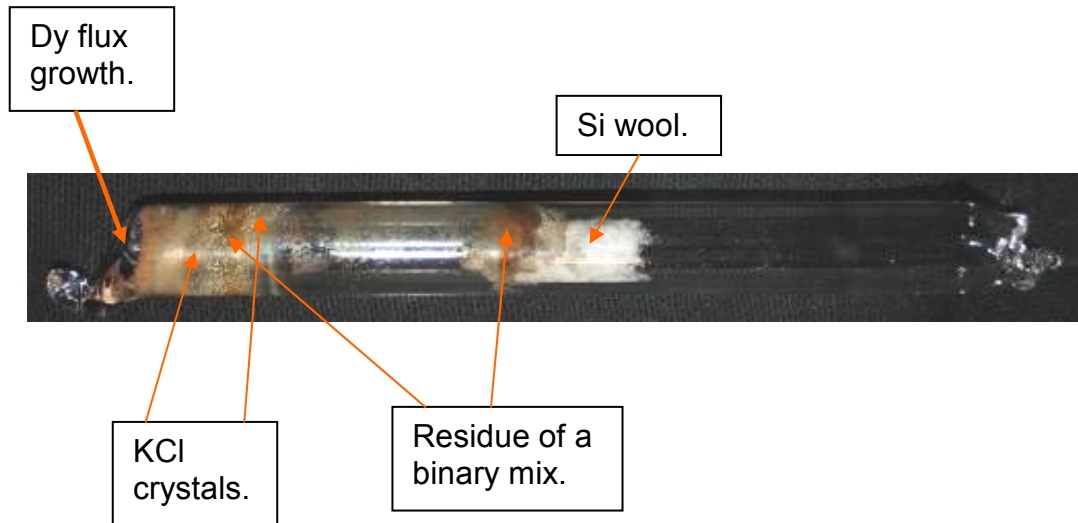


Figure 10. Sealed quartz tube after the flux Dy crystals growth. The short piece of silicon wool is put inside the tubes to prevent the binary mix from migrating too far along the tube walls.

The tubes are heated for 25 hours at 700° C in a commercially available muffle furnace. Figure 11, below, shows the KCl flux grown Dy crystals.

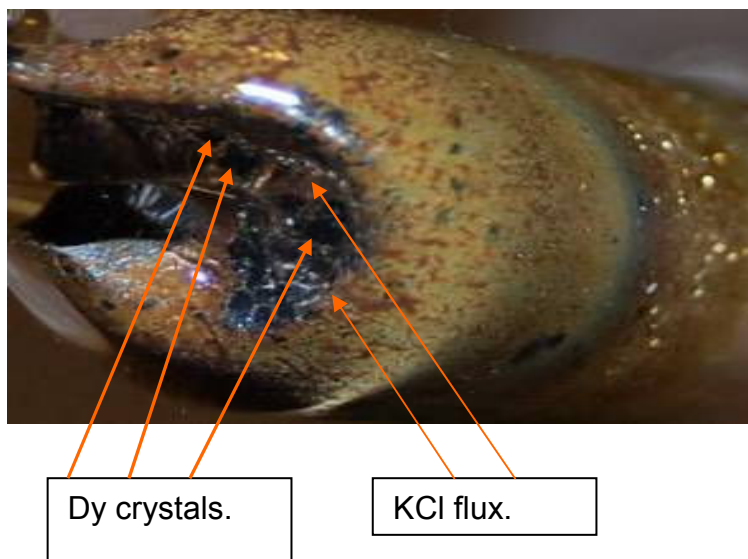


Figure 11. Bottom of a quartz tube with 0.33 and 0.66 mix of Dy and KCl by weight, upon the flux growth.

Using X-ray diffraction, the quality of the crystals grown from all the different batches of the Dy-KCl mix was checked. The best quality crystals grown, which were used in single crystal diffraction experiments, were from the mix where the mass ratio of the binary system of Dy and KCl was ~50% KCl and ~50% Dy powder by weight.

Upon the Dy crystal growth, the quartz tubes are opened using a Tungsten-Carbide scribe. The KCl flux with Dy crystals is, carefully, scraped with a sharp, plastic toothpick off of the quartz tube walls and bottom into a clean, clear, plastic container. Recovered samples are kept on glass slides in a desiccator. Each crystal is covered with a droplet of Dow-Corning 200 Silicone fluid, shown in Figure 12, below.

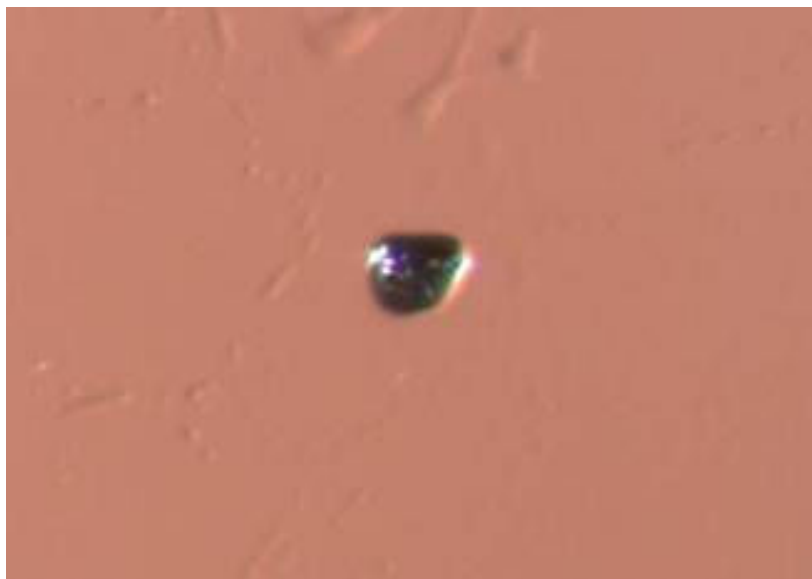


Figure 12. Dy crystal on a glass slide, enveloped in Dow-Corning 200 Silicone fluid. The crystal is ~40  $\mu\text{m}$  long and ~1  $\mu\text{m}$  thick.



## X-Ray Diffraction Experimental Details

Limited angular access to the small size sample in DAC yields limited structural data obtained by X-ray diffraction. But in the case of a synchrotron beam, high energy and high brilliance allow for the use of X-ray diffraction to collect structural data from the samples in DAC. Therefore, the high pressure X-ray diffraction measurements for both Dy and Pr samples in a DAC are done at a synchrotron radiation source. In a synchrotron radiation source (storage ring) electrons or positrons are injected in a very large evacuated loop and kept circulating at relativistic velocities by energy delivered from radio-frequency sources. In the storage ring, synchrotron radiation is produced either in the bending magnets needed to keep the electrons in a closed orbit, or in insertion devices such as wigglers or undulators placed in the straight sections of the storage ring. In the insertion devices an alternating magnetic field forces the electrons to follow oscillating paths. In a wiggler the amplitude of oscillation is large, and the radiations from different wiggles add incoherently. In an undulator the small-amplitude oscillations from the passage of a single electron produce a coherent addition of the radiation from each oscillation. The required wavelength of the radiation is usually selected by a crystal monochromator. The monochromatization here is usually the diffraction by a crystallographic plane with the highest Bragg reflectivity. The monochromated beam is focused using X-ray mirrors. The mirror surface is usually coated with a heavy material like gold in order to obtain a large electron density. This produces a large critical angle for total reflection, thereby reducing the required length of the mirror. By

curving a mirror, the focusing optical element for the X-rays is provided. The radiation from the ring is delivered into beam line hutches that are tangent to the storage ring. The X-ray diffraction data at the synchrotron source is recorded with an area detector. The types of area detector used in this experiment were a charge coupled device (CCD) and an image plate (IP). A CCD detector, similar to those found in video cameras, is activated by the X-rays falling on a thin layer of material which then fluoresces in the visible region. The IP detector surface layer is made of X-ray storage phosphor of barium-europium halides. A phosphor is photo-stimulated by X-rays and the photo-electrons form color centers where the information relating to the incident X-ray quanta is stored. Exposing the plate to a laser beam causes the color centers to reemit in the visible region.

Single crystal diffraction data was collected at the 16-ID-B (insertion device beam line) of the High Pressure Collaborative Access team (HP-CAT) at the Advanced Photon Source (APS) of Argonne National Laboratory (ANL)<sup>2</sup>. This is an undulator beam line. The X-rays are delivered to ID-B hutch from ID-A hutch. High heat-load slits, double crystal monochromator (water cooled diamond 111), and the branching monochromator (Si 220) from ID-A hutch delivered a monochromatic X-ray beam with 30 keV energy into ID-B hutch [21]. The beam in the ID-B hutch is focused with K-B mirrors by total reflection in a focal spot, few microns in size. A 30  $\mu\text{m}$  diameter pinhole is used to suppress parasitic scattering from the upstream slits. Diffraction patterns are collected with either

---

<sup>2</sup> An experiment was performed at the Cornell High Energy Synchrotron Source-CHESS. The beam line is a bending magnet one, with an unfocused beam monochromated by a Si 220 crystal.

MAR165 (CCD) or MAR345 (IP) area detectors. The beam line is controlled by a distributed control system set of software tools and applications called EPICS. Data is acquired on Windows XP and Linux operating systems workstations, running display and control software written in Java, IDL, and Motif graphical user interface. 16-ID-B hutch is shown in Figure 13, below.

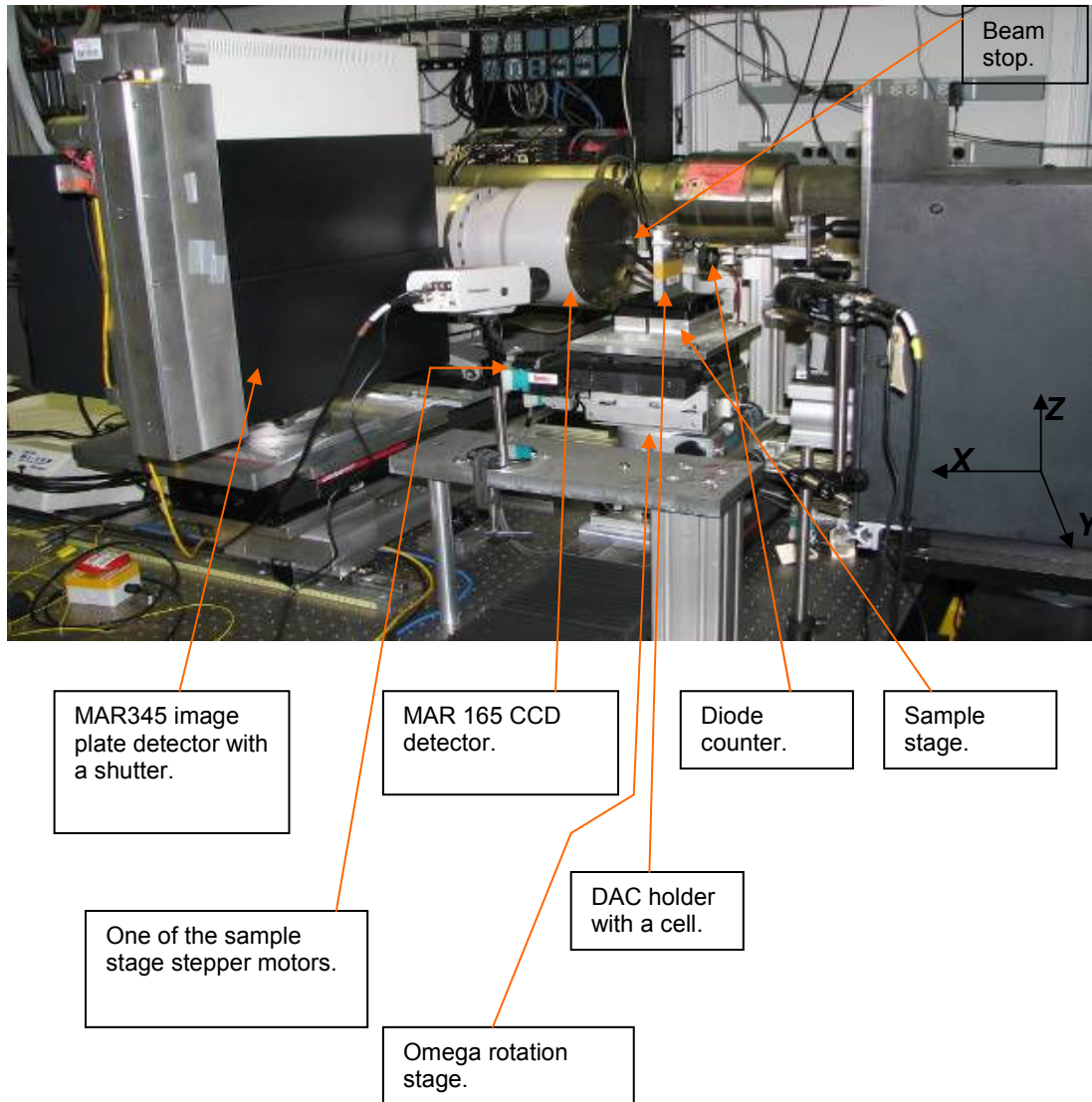


Figure 13. Experimental hutch for 16-ID-B at APS. Picture courtesy of Stanislav Sinogeikin from APS. The hutch coordinate system is labeled in the lower right corner of a figure.

The hutch experimental set-up is conceptually based on the principle of four-circle single-crystal diffractometer geometry. The diffractometer has three computer controlled circles ( $\chi$ ,  $\omega$ ,  $\varphi$ ), which rotation axes intersect with one another to an accuracy of about 10  $\mu\text{m}$ . The crystal is centered at this point. With the use of micro stepping motors, the crystal is then oriented to the incident X-ray beam so that the Bragg condition is met and the reflection occurs in the horizontal plane, in which the fourth circle ( $2\theta$ ) brings the counter to the appropriate position for measuring the reflection. In 16-ID-B hutch two diffractometer “circles” are available, as virtual angular coordinates:  $\chi$  and  $2\theta$  (plane of a detector), while  $\omega$  (DAC) rotation stage providing third angular dimension. Using a two-dimensional position sensitive device, like an area detector, allows for the recording of the diffraction information on an array of peak positions simultaneously, instead of just a single point at a time, as with the diffractometer. As in the case of the diffractometer, the sample in DAC is centered in the X-ray beam prior to data collection.

To obtain the diffraction geometry the diffraction pattern of a standard is taken. The standard pattern provides the sample to detector distance, detector inclination angle to the beam, and the coordinates of the X-ray beam center. The procedure of obtaining diffraction geometry from a standard pattern is explained in CHAPTER 3. The standard was either Cerium dioxide ( $\text{CeO}_2$ ) or Silicon (Si) powder. The standard powder used is one exhibiting homogeneous crystallite size and absence of any strains, as per NIST (National Institute of Science and Technology, USA) specifications. The powder is packed in a retainer sample

chamber of  $\sim 200 \mu\text{m}$  in diameter provided by the beam line. The initial set of Cartesian coordinates of a standard are needed before the standard is centered in a beam. The hutch axes are defined in an orthogonal lab system, with positive x-axis pointing downstream from the beam, positive y-axis at a right angle to x-axis in horizontal plane, clockwise as viewed from above, and positive z-axis upwards. To obtain an initial set of orthogonal coordinates “off-axes” system is used. The reference position of the beam line and the “off-axes” system are identical, as they are set in relation to the same point, namely the center of the tungsten wire crosshair. The “off-axes” system provided an optical centering of a standard, using a camera with a monitor display with x, y, and z translational stages driven by micro stepper motors. Upon obtaining the initial coordinates the retainer with standard is mounted on the omega stage in the hutch. The stage with a retainer is driven by stepper motors to the initial coordinates, stepper motor stage in Figure 13, page 32. A diode is used as an X-ray counter, by recording X-ray transmission through the standard, while the retainer is moved in 5 - 10  $\mu\text{m}$  steps through the beam along the y-axis, then z-axis. The coordinates in y and z, which corresponded to the maximum values for the transmitted X-ray peak counts are recorded. The stepper motors then move the retainer to the recorded y-z coordinates. Afterwards the retainer is rotated on an omega stage at two different angular values. For each of the omega values ( $\omega > 0^\circ$  and  $\omega < 0^\circ$ ) the retainer is moved along the y coordinate. Each y coordinate value for the maximum X-ray peak counts at  $\pm\omega$  is found and in accordance with previously obtained maximum y coordinate for  $\omega = 0^\circ$ , is used to triangulate the retainer x

coordinate, so that the standard is focused in the beam. Once the standard is centered in the beam, the counter diode is removed and the powder diffraction pattern is recorded by the area detector for a duration of 10-15 seconds.

After the diffraction pattern of a standard is collected, the DAC with a sample at ambient pressure is located and centered in the beam, sample stage in Figure 13, page 32. The procedure of centering the DAC in the beam was similar to centering the standard, except that due to the high atomic weight of both Pr and Dy samples, the centering is based on the X-ray absorption of the sample, rather than transmission.

The diffraction data is collected in two parts. To record a large fraction of the reflections which cross the sphere of reflection, a sweep scan is done. In this scan the cell in a beam is rotated on the omega stage throughout the available angle of opening for the X-ray diffraction. In the case of a Four Pin cell with B-A anvils, the backing plate cone of opening was  $64^\circ$ , so the rotation is executed from  $\omega = -32^\circ$  to  $\omega = 32^\circ$  for 64 seconds. The sweep scan recording of a diffraction pattern contained the  $\chi$  and  $2\theta$  information for each diffracting peak. The sweep scan pattern is, also, used to control and screen the quality of a crystal by examining the profile of some reflections. The sweep scan pattern did not contain the  $\omega$  information for the peaks. Therefore a step scan was needed, where the cell is stepped through  $\Delta\omega$  steps, and at each step the cell is oscillated for a small, predetermined value in  $\pm\omega$  for tens of seconds. As the sample oscillated about a fixed position in  $\omega$  step scan, reciprocal-lattice points pass back and forth through the sphere of reflection, while their average intensities are

recorded in the individual detector frames. Because of the low angular resolution (due to set instrumental individual pixel size) given by area detector geometry for a peak size recorded, the diffraction peak profiles are spread over more than one pixel causing large uncertainty in the  $\omega$  information of the peaks recorded.

Therefore, to average the uncertainty in  $\omega$  information of the peaks, the small angle of oscillation is executed for each step scan. Also, the longer duration of sampling of a fraction of the total available reciprocal volume potentially allows for peaks that were weak or non-existent in the sweep scan to be recorded in a step scan. Once the diffraction peaks of the first frame are recorded, the cell is driven to the next oscillating point, such that the new oscillating range slightly overlaps the previous one. For the Four Pin cell the oscillating points were  $1^\circ$  apart, with an oscillating range of  $\pm 0.5^\circ$ . The step scan started at  $\omega = -31.5^\circ$  and ended at  $\omega = 31.5^\circ$  because of the available angular opening of  $64^\circ$ . The duration of each scan was 15 seconds.

Upon finishing all the scans, the cell is removed from the hutch and the pressure is raised in small,  $\sim 1$  GPa, steps. After measuring the pressure with ruby fluorescence, the cell is placed back in the hutch and centered in the beam. Another set of scans is done and the corresponding diffraction patterns are recorded. This experiment is continued until the X-ray diffraction data for all the pressure points is recorded in the interval of interest.

CHAPTER 3  
THEORY AND DATA ANALYSIS

Crystal Lattice

A crystal is a solid object in which a basic pattern of atoms is periodically repeated throughout in all three dimensions. To describe the structure of a crystal, it is thus only necessary to know the simplest repeating pattern, as well as the lengths and directions of the three vectors. These vectors together describe pattern repetition in space. Crystal constituent atoms, molecules or ions represent building blocks of such a pattern. Normally, the pattern consists of several such blocks, which may be converted into one another by symmetry operations. The three vectors **a**, **b**, **c** describing the translations of the pattern in space are called the basis vectors. By their operation one upon another, a lattice is generated. Any point in such a lattice may be described by a vector **r**,

$$\vec{r} = n_1\vec{a} + n_2\vec{b} + n_3\vec{c} \quad (5)$$

where  $n_1$ ,  $n_2$ , and  $n_3$  are integers. The concept of the lattice is an abstract mathematical one, which allows for its origin to be chosen more or less arbitrarily in the crystal.

The smallest repeating volume of the lattice is called the unit cell. It is characterized by the lengths of the basis vectors, the three lattice constants  $a$ ,  $b$ ,  $c$  and by the three angles  $\alpha$ ,  $\beta$ ,  $\gamma$  which separate these vectors from one another. By definition,  $\alpha$  is the angle between the basis vectors **b** and **c**,  $\beta$  between **a** and



**c**, and  $\gamma$  between **a** and **b**. The positions of atoms are described in terms of the basis vectors axes and are given in terms of  $x, y, z$  coordinates with lattice constants as units [22].

In addition to the three dimensional periodicity, a further very important property of nearly all crystals is their symmetry. Full consideration of the possible symmetries for the lattice gives rise to seven possibilities, the seven crystal systems. They are distinguished from one another by their shape-the geometry of the lattice that is required by the underlying symmetry elements. The table describing seven crystal systems is given in Table 1, below.

Table 1. The seven crystal systems and the symmetry requirements for each of the corresponding unit cells.

Crystal System	Geometric Requirements in	
	Cell Edges	Cell Angles
triclinic	none	none
monoclinic	none	$\alpha = \gamma = 90^\circ$
orthorhombic	none	$\alpha = \beta = \gamma = 90^\circ$
tetragonal	$a = b$	$\alpha = \beta = \gamma = 90^\circ$
rhombohedral	$a = b = c$	$\alpha = \beta = \gamma \neq 90^\circ$
trigonal/hexagonal	$a = b$	$\alpha = \beta = 90^\circ, \gamma = 120^\circ$
cubic	$a = b = c$	$\alpha = \beta = \gamma = 90^\circ$

In the description of a lattice, the smallest possible basis vectors should be chosen for the crystal. The smallest possible basis vectors represent the smallest possible volume unit in the lattice, the unit cell. This is called a primitive cell. For the primitive cell, there could be few choices available describing a single lattice, all with the same volume. The choice of a single unit cell out of few possible for the description of a crystal structure, will be the cell that exhibits the highest possible symmetry. There are also cases in which all variants of a primitive unit cell are oblique, but a larger, non-primitive cell, with 2, 3 or 4 times the volume may be chosen, which corresponds to a crystal system of higher symmetry. When lattices are described by these larger cells, eight centered lattices must be added to the six primitive lattices. Together these fourteen different lattices are known as Bravais lattices, named after Auguste Bravais who first listed them in 1850 [22]. The characteristic symmetry elements, like rotations, reflections, and inversions, relating the points of an assemblage, within a closed set, are known as the crystallographic point group or crystal class. There are 32 possible crystal classes. Each one falls under one of the seven crystal systems. It was shown, in the latter part of the nineteenth century that combining the 32 point groups with the 14 Bravais lattices leads to 230 unique arrangements of points in space. These are the 230 space groups that describe the only ways in which identical objects can be arranged in an infinite 3D lattice.

## The Geometry of X-Ray Diffraction

When radiation with a wavelength of the order of the lattice spacings interacts with the crystal, one would expect to observe characteristic interference phenomena, since a crystal is a periodic, 3D array, described by its lattice. In 1912 [22], Max von Laue showed that crystals are based on a three dimensional lattice, by scattering X-rays with a wavelength in the vicinity of interatomic distances,  $\lambda = 50 - 300$  pm (pico meters).

Every atom in any crystal has the 3D arrangement of the lattice points of the crystal. The actual crystal is built by placing together as many identical lattices as there are atoms in the unit cell, all displaced from one another as the individual atoms are. A crystal consisting of a single atom in the unit cell will then consist of a lattice with a single scattering center at each lattice point. A single row from such a lattice, pointing along the **a**-axis is shown in Figure 14.

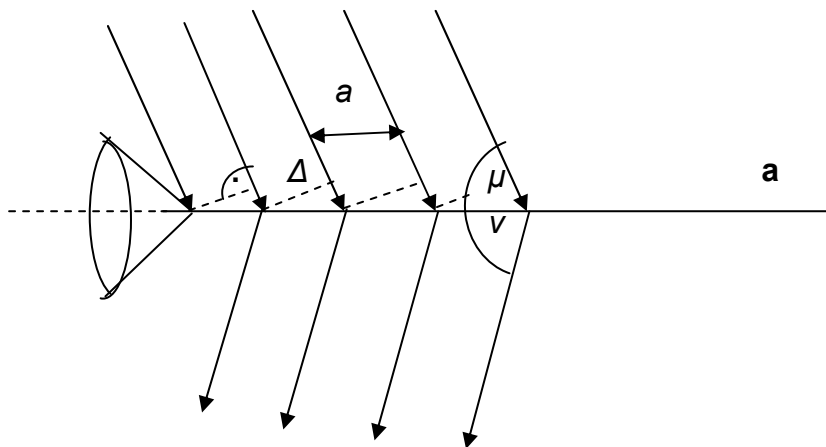


Figure 14. Scattering by a row of atoms along the **a**-axis,  $\mu =$  X-ray angle of incidence  $\equiv \nu =$  X-ray angle of scattering. Constructive interference occurs in the directions of a Laue cone with a cone angle of  $2\nu$  and a path difference  $\Delta = n\lambda$ .

The path difference,  $\Delta$ , between waves scattered by two neighboring points will be related to the angle of incidence  $\mu$  and the angle of scattering  $\nu$  by the equation:

$$a(\cos \mu_a) + a(\cos \nu_a) = n_1 \lambda \quad (6)$$

For any given angle of incidence  $\mu$  and any given order  $n_1$ , there will be a precisely defined scattering angle  $\nu$  at which a scattered beam can be observed. Since waves are scattered in all directions, the locus of these observable waves will be a cone about the row of points with a half angle  $\nu$ . For each value of  $n$  there will be one such cone, and this coaxial set is called Laue cones. If the interaction of the same ray with a second row of atoms, not parallel to the first, along **b**-axis is considered, the same reasoning as before will lead to the equation:

$$b(\cos \mu_b) + b(\cos \nu_b) = n_2 \lambda \quad (7)$$

This second row of atoms will then give rise to a second set of coaxial cones indicating the directions in which observable waves are scattered. Picking the third row of atoms along the **c**-axis will lead to the equation:

$$c(\cos \mu_c) + c(\cos \nu_c) = n_3 \lambda \quad (8)$$

The third row of atoms will in turn give rise to a third set of coaxial cones indicating scattering of the observable waves. Therefore these three equations, (6), (7), and (8), so called Laue equations, must be fulfilled at the same time for the direction of an incident and diffracted ray. This condition requires that the three Laue cones intersect one another into a line. Because this condition in the experiment is only met when X-rays from a very specific direction fall upon the crystal, its probability of occurring is very low. Therefore the more a crystal is displaced in space, while in the X-ray, provides one a better opportunity for observing a diffraction pattern.

The diffraction in three dimensions could also be described as a reflection by a plane defined by three points of the lattice. If the Laue conditions are met for this reflection, a reflection is observable. The planes that give rise to such reflections are called lattice planes. The orientation of the planes relative to the lattice is defined by Miller indices, after William Hallows Miller, with the values  $hkl$ . Every plane passing through points of the lattice is one of group of parallel planes, such that every lattice point will be placed in one of the planes from the group. These planes intercept **a**, **b**, and **c**-axes of the unit cell and are defined as the reciprocals of the fractional intercepts which the plane makes with the crystallographic axes. These reciprocals, which are integers, are the  $hkl$  values.

As shown from the Laue equations, for constructive interference a reflection condition must be met for a set of lattice planes where the angle of incidence must equal the angle of reflection. This angle must have such a value that the conditions of the three Laue equations are met and the entire set of planes in the

lattice must be scattering in the phase. Father and son, W.H. and W.L. Bragg showed that the reflection angle could be calculated in terms of the path difference between a ray reflected by one plane and that reflected by the next plane after it in the lattice, Figure 15.

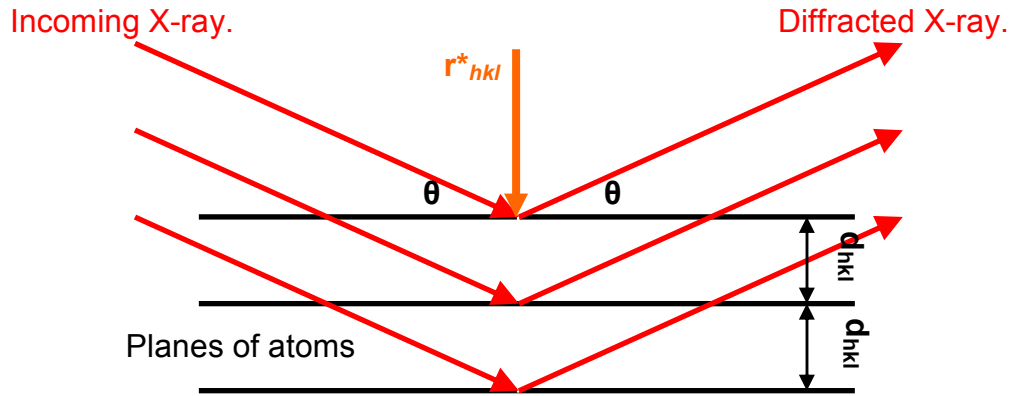


Figure 15. Derivation of the Bragg equation using path difference between rays reflected from a lattice planes. The lattice spacing is labeled by  $d$ .  $\theta$  is an angle of incidence/reflection of the X-rays off of atoms in the planes. Atoms are represented here by black lines. The reciprocal space vector (orange arrow) is shown in reference to a lattice planes in direct space, signifying equivalence between Bragg's Law and Laue condition description of X-ray diffraction.

Only those angles  $\theta$  are allowed where the path difference  $2d(\sin\theta)$  is an integral multiple of the wavelength:

$$2d_{hkl}(\sin\theta_{hkl}) = n\lambda \quad (n = 1, 2, 3, \dots) \quad (9)$$

where  $n$  is the order of diffraction.

The equivalence of Laue's and Bragg's formulation of X-ray diffraction follows from the relationship between points in scattering space and planes in reflection space. This relationship allows describing each set of lattice planes by a vector,  $\mathbf{r}^*$ , which direction is normal to the planes and magnitude being the reciprocal of plane spacing. Then each observed diffraction spot would be located at the end point of this vector in the unit cell. Therefore all of these vectors would terminate within the unit cell. Thus a vector  $\mathbf{r}^*$  could be defined in a coordinate system of reciprocal unit vectors:  $\mathbf{a}^*$ ,  $\mathbf{b}^*$ , and  $\mathbf{c}^*$ , such as:

$$\vec{r}^* = h\vec{a}^* + k\vec{b}^* + l\vec{c}^* \quad (10)$$

Since the indices  $hkl$  are all integers, the representation of all lattice planes by the ends of the  $\mathbf{r}^*$  vectors gives another true lattice, resulting from 3D repetition of the three basis vectors  $\mathbf{a}^*$ ,  $\mathbf{b}^*$ , and  $\mathbf{c}^*$ . The smallest repeating 3D unit may be called the reciprocal unit cell, while the lattice the reciprocal lattice. Similarly, the lattice defined by the basis vectors  $\mathbf{a}$ ,  $\mathbf{b}$ , and  $\mathbf{c}$  is often called the direct or real lattice. The reciprocal of the reciprocal lattice is the direct lattice.

### Calibration

Before any data was analyzed, the data had to be calibrated. The calibration consisted of fitting powder diffraction pattern from a standard calibrant sample. Using a standard calibrant with accurately known  $d$ -spacings allowed for refining the individual parameters of the diffraction geometry: X-ray beam center, the

sample to detector distance, and detector tilt. Here the tilt referred to a possible non-orthogonal position of a detector to the beam. Either cerium dioxide ( $\text{CeO}_2$ ) or silicon (Si), were used as the calibrants. These are standard reference materials used in quantitative X-ray diffraction analysis and certified by the American National Institute of Standard and Technology (NIST). The lattice parameters of the standards are determined to the 7<sup>th</sup> significant digit. To fit the powder diffraction of a standard and refine the parameters of the diffraction geometry, FIT2D, 2-D data analysis software [23] was used. An example of an input image in FIT2D POWDER DIFFRACTION (2-D) interface for the Si powder diffraction pattern was given in the Figure 16, below.

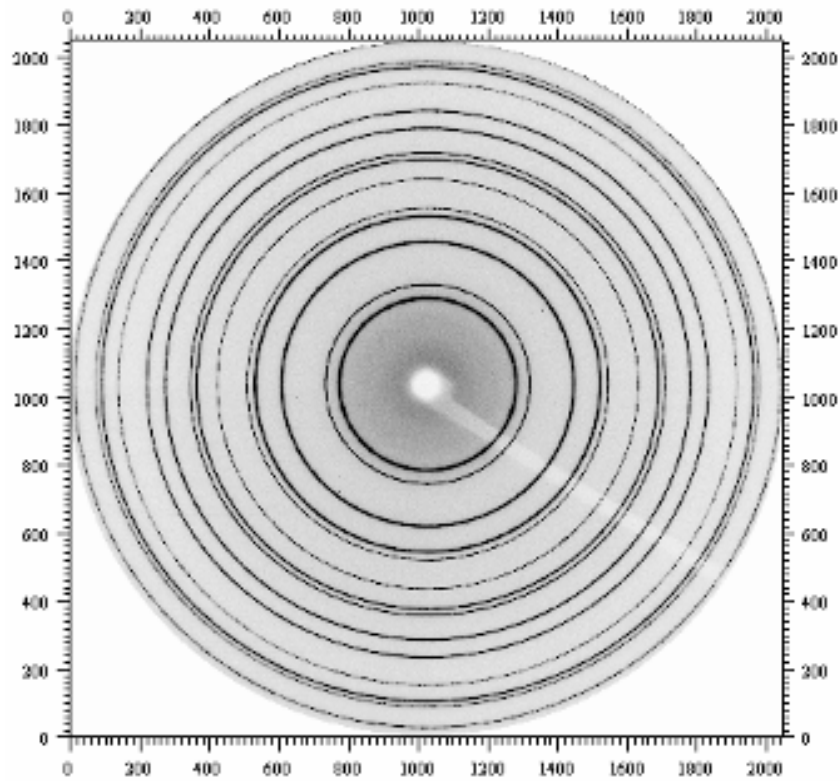


Figure 16. Diffraction pattern (rings) of the Si powder sample displayed in FIT2D. The white shadow across the image is the beam stop. The image size in pixels is 2048X2048.



Once the powder pattern is displayed in FIT2D POWDER DIFFRACTION (2-D) CALIBRANT interface, the SELECT CALIBRATION SAMPLE choice menu would appear, see Figure 17. To proceed, one would click on a box with a standard name that matched calibrant used in this thesis experiment, SILICON.



Figure 17. The SELECT CALIBRATION SAMPLE choice menu in FIT2D.

After the calibrant was selected the CALIBRANT PATTERN REFINEMENT control form appeared, shown in Figure 18, page 47. The known wavelength of the X-ray beam was input in the control form. The measured, approximate sample to detector distance was entered, too. The refined parameters, in this order, were: X-ray beam center, sample to detector distance, and tilt of a detector.

O.K.	CANCEL	?	HELP	INFO
DESCRIPTIONS		VALUES	CHANGE	
SAMPLE TO DETECTOR DISTANCE (MM) (STARTING)		315.0000	DISTANCE	
WAVELENGTH (ANGSTROMS) (STARTING)		1.540000	WAVELENGTH	
SIZE OF HORIZONTAL PIXELS (MICRONS)		100.0000	X-PIXEL SIZE	
SIZE OF VERTICAL PIXELS (MICRONS)		100.0000	Y-PIXEL SIZE	
NUMBER OF AZIMUTHAL SECTIONS		90	ANGULAR SECTIONS	
REFLECT OUT-LYING POSITIONS AND RE-REFINE		YES	REFLECT OUTLIES	
REFLECT LIMIT FROM IDEAL (STANDARD DEVIATIONS)		4.000000	REFLECT LIMIT	
OUTPUT FULL INFORMATION		YES	FULL INFO	
REFINE X/Y BEAM CENTRE		YES	REFINE BEAM X/Y	
REFINE SAMPLE TO DETECTOR DISTANCE		YES	REFINE DISTANCE	
REFINE X-RAY WAVELENGTH		YES	REFINE WAVELENGTH	
REFINE DETECTOR NON-ORTHOGONALITY		YES	REFINE TILT	
FIT INTERMEDIATE NUMBER OF RINGS		NO	EXTRA ITERATIONS	

Figure 18. The CALIBRANT PATTERN REFINEMENT control form. The columns on the left-hand side described diffraction geometry parameters. The corresponding values of the parameters were given in the middle column. The buttons for changing the parameters were in the right-hand column. The descriptions of all the parameters are given in the left-hand column. The refinement was done on X-ray beam center, sample to detector distance, and tilt.

Upon loading the data in the control form, determination of an initial X-ray beam center position was done. The determination was done by means of a least square fit of a circle to an outer diffraction ring. An initial beam center fit is shown in Figure 19, page 48.

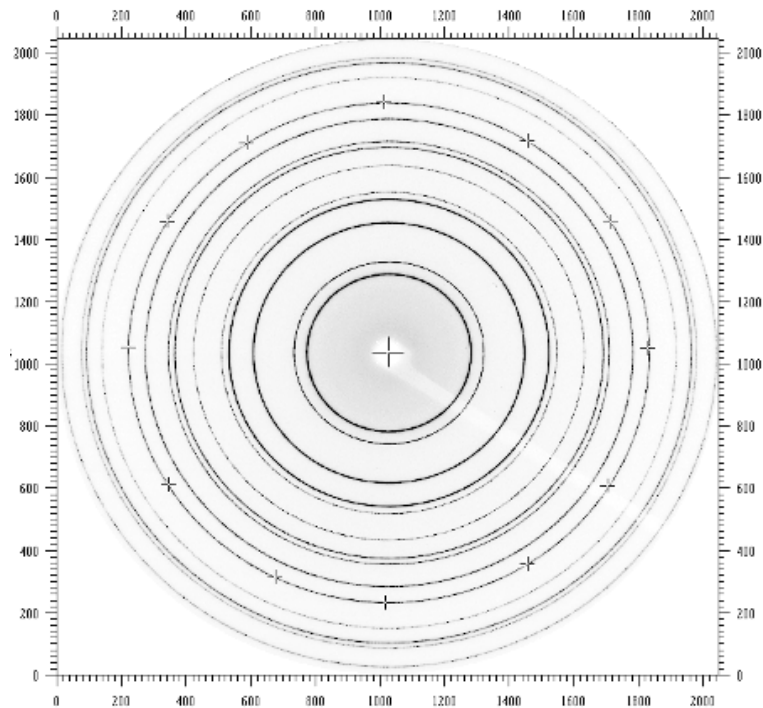


Figure 19. The initial beam center refinement for the Si diffraction pattern. The cross mark in the middle of the image is the center of the circle, i.e. initial X-ray beam centre. The least square fit of the circle was done to twelve coordinates, which were defined by twelve cross hairs on an outer diffraction ring.

Thereafter, sample to detector distance and tilt are refined. All three parameters would continually be refined independently of each other, until the values for each of these parameters converged to respective individual minimum. After refinement, the INTEGRATE command in the POWDER DIFFRACTION (2-D) menu was used, to integrate the 2-D powder diffraction pattern to a 1-D two-theta scan. An example of the two-theta scan generated in FIT2D is shown below in Figure 20, page 49.

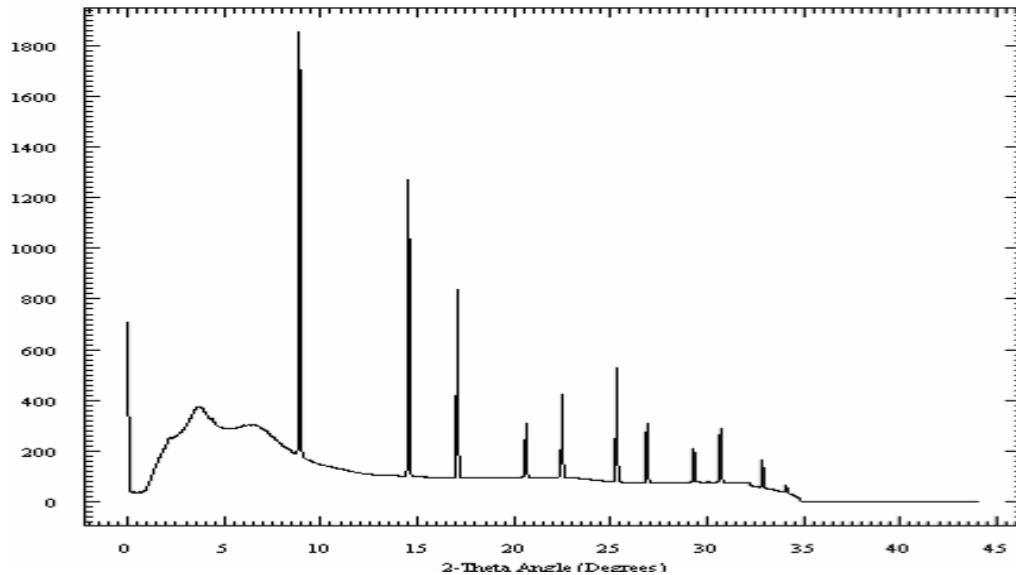


Figure 20. Integrated diffraction pattern of the calibrant into two-theta scan. The integration was done with INTEGRATE command of the FIT2D's POWDER DIFFRACTION (2-D) interface.

After generating the two-theta scan, it is exported to American Standard Code Information Interchange (ASCII) file format. This file is loaded into the Powder Cell software [24]. This software is used for the structure model analysis. It provides graphical comparison of two or more integrated standard diffraction patterns generated by FIT2D. The  $d$ -spacings and  $hkl$  indices for reflections in each of the diffraction patterns are also provided. The two-theta scans from the calibrant and NIST standard diffraction patterns are overlaid in Powder Cell in order to identify any possible zero-offset in the scans as distortion not corrected by FIT2D, as shown in Figure 21, page 50.

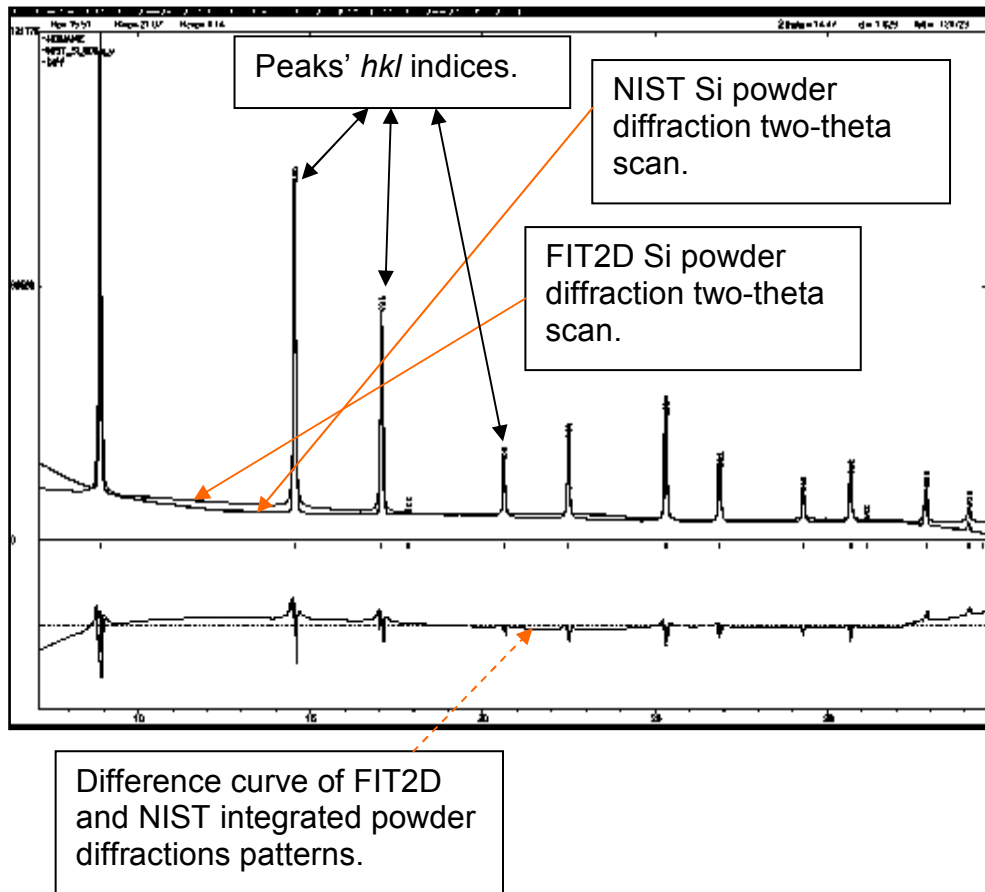


Figure 21. Powder Cell zoomed in display of the calibrant integrated diffraction patterns from NIST and FIT2D. The relevant two-theta scans with a few  $hkl$  indices for the peaks and a scans residual are indicated by the arrows.

Once the check on quality of the calibration is done, the software analysis of Pr and Dy diffraction data is performed.

#### Analysis of Pr Data

The Pr samples of crystals grown were grained aggregates of multi-crystals. All attempts of indexing one or several of the multi-crystals failed. A typical Pr sample diffraction pattern on the MAR345 image plate is shown in Figure 22,

below. Along the diamonds reflections, powder pattern rings with individual reflections belonging to several Pr single crystals were present in the diffraction image.

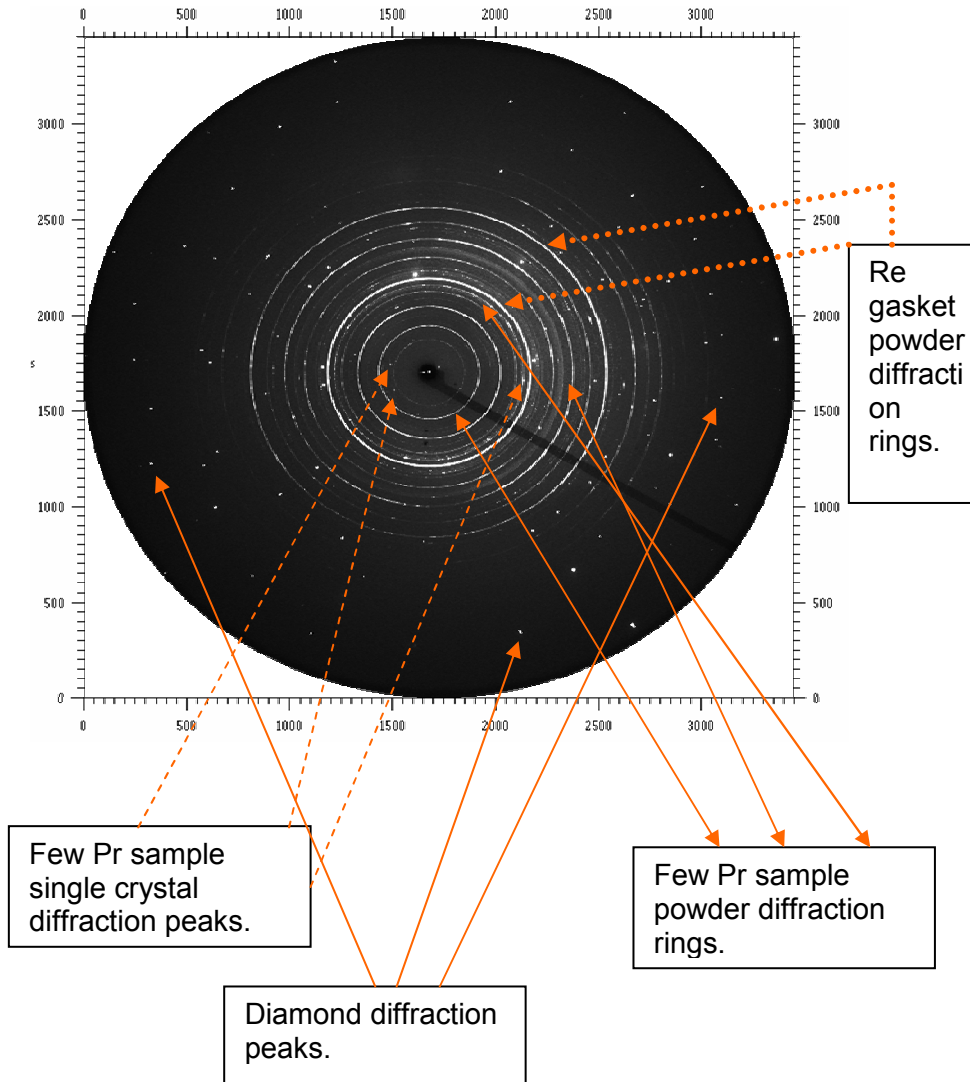
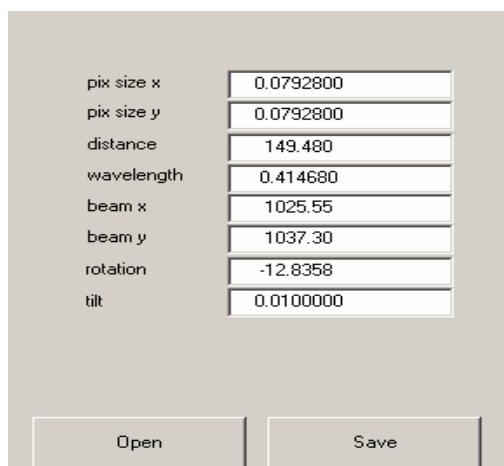


Figure 22. MAR3450 image plate frame, 3450X3450 pixels<sup>2</sup>, of the diffraction pattern of Pr crystal in the DAC at 4.95GPa displayed in FIT2D. This image was obtained by rotating DAC in the X-ray beam around the  $\omega$  axis, so this was an image of a sweep scan in  $\omega$ . The  $\omega$  range was 14°, from -7° to 7°, relative to the DAC backing plate cone of opening. The relevant diffraction patterns are indicated by different sets of orange arrows. The dark, rectangular image across is a shadow from the X-ray beam stop. Ruby crystal and KBr powder diffraction peaks and rings respectively are present, too.

## Analysis of Dy Data

The Dy single crystal diffraction patterns collected either with CCD or image plate detector were processed in Przemyslaw Dera's software suites, GSE (GeoSoilEnviro)\_ADA (GSE in further text) and RSV (Reciprocal Space Viewer). The GSE suite manipulated the 2-D images of the single crystal diffraction pattern. It allowed for determining the angular coordinates ( $2\theta$ ,  $\omega$ , and  $\chi$ ) for each diffraction peak and conversion to Cartesian coordinates of laboratory coordinate system (CHAPTER 2). The initial peak identification and fitting is done in GSE, too. The RSV suite accepted as an input GSE Cartesian coordinates of the peaks and calculated corresponding  $d$ -spacings list and displayed and manipulated the undistorted array of diffraction peaks in reciprocal space. The RSV allowed for determining and refining of the orientation matrix.

Before the diffraction pattern image is uploaded in GSE, the diffraction geometry parameters obtained from calibration in FIT2D had to be input and saved in GSE file format, shown in Figure 23, below.



The screenshot shows a software interface with a list of parameters and their corresponding values in input fields. At the bottom, there are two buttons labeled 'Open' and 'Save'.

pix size x	0.0792800
pix size y	0.0792800
distance	149.480
wavelength	0.414680
beam x	1025.55
beam y	1037.30
rotation	-12.8358
tilt	0.0100000

Open Save

Figure 23. Input for calibration file in GSE.

After the calibration file was saved in GSE, a Dy diffraction pattern frame image was uploaded in the main viewing window of the software suite, Figure 24.

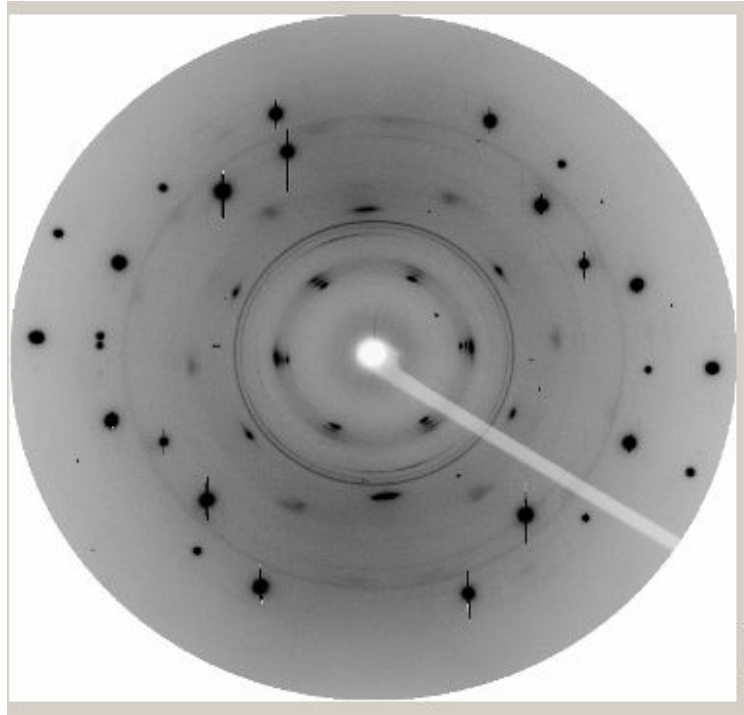


Figure 24. CCD image of the diffraction pattern of Dy crystal in the DAC at 2.74 GPa displayed in GSE. This image was obtained by rotating DAC in the X-ray beam around the omega axis, so this was an image of a sweep scan in  $\omega$ . The  $\omega$  range was  $64^\circ$ , from  $-32^\circ$  to  $32^\circ$ , relative to the DAC backing plate cone of opening. The peaks that are rounded and saturated are the diamond diffraction pattern. Small peaks are from the ruby diffraction pattern. All the other peaks are the diffraction pattern from Dy. The smooth rings are the diffraction pattern from the Re gasket. The white, rectangular image across is a shadow from the X-ray beam stop.

To start the analysis in GSE an initial set of diffraction peaks was picked from the  $\omega$  sweep scan image. The peaks initially chosen were those that could be distinguished visually from the background and other, spurious diffraction peaks.



Automatic peak fit and centering by GSE was within twenty pixels wide square area. The peak fitted pattern is shown in Figure 25, below.

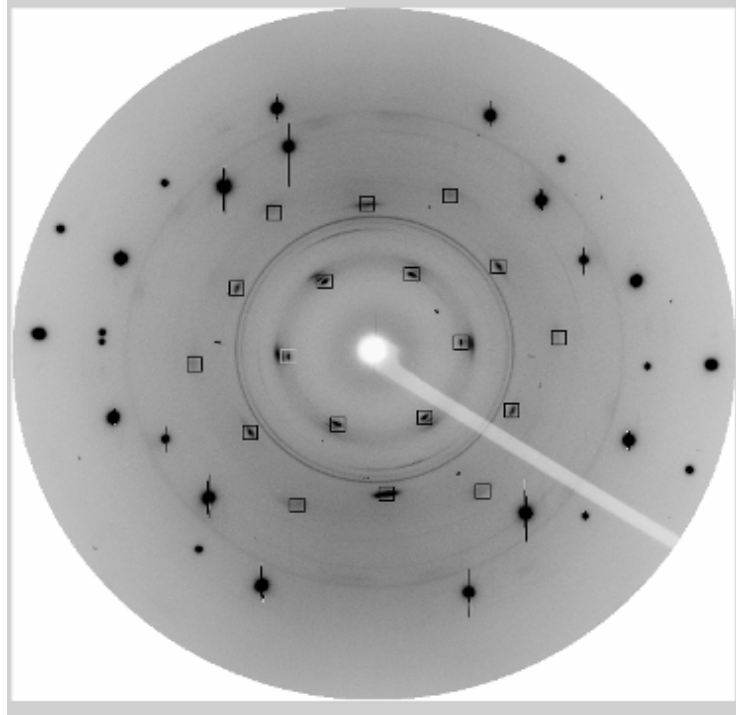


Figure 25. Initial choice of the Dy diffraction peaks in GSE. The peaks were chosen with 20 pixels wide squares. Each square was centered on a peak using the Peak fit automated option. The peaks selected were saved in a file.

Upon peak selection, the peak list with accompanying two angular coordinates is saved in a file. Then, the  $\omega$  oscillation diffraction image (step scan), for  $\omega = -31.5^\circ$ , is loaded in the GSE viewing window as shown in Figure 26, page 55. This is the first angle that allowed for the primary beam to diffract from the sample, as discussed in detail in CHAPTER 2.

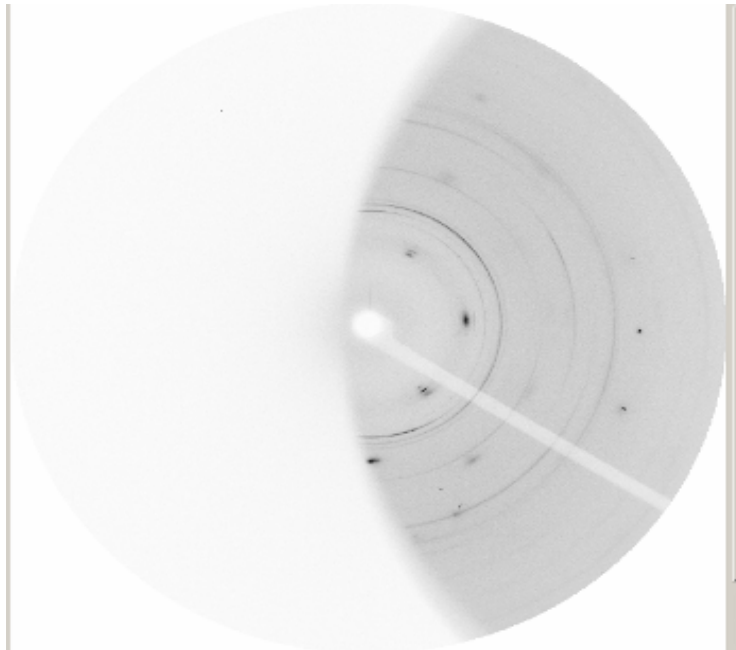


Figure 26. Diffraction pattern of Dy sample in the DAC, with DAC rotated  $-31.5^\circ$  into the X-ray beam, displayed in GSE. The DAC was oscillated  $\pm 0.5^\circ$  around initial value of  $\omega = -31.5^\circ$ , for 15 seconds. Therefore this is the first  $\omega$  step scan.

The peaks found from the first step scan that were observed in sweep scan are saved, so the  $\omega$  coordinates of the peaks are recorded. Also, because the sample oscillation allows for unique Bragg's diffraction conditions to be fulfilled peaks not present in the initial peak file are found and saved in a new file. Next, this new file and initial peak choice file are opened and laid over a sweep scan from Figure 25, page 54. This way, if any new peaks were found not included in the initial peak choice, the check is performed to see if those peaks belonged to the same lattice and if they should be kept. Also, the more intense peaks (new peak maxima) from the new peak file were kept over the same, but weaker peaks from the initial peak choice. Afterwards both the initial peak choice file and the

new file were saved with the corresponding angular coordinates in a single peak file. Then, diffraction patterns for each of the step scans are checked in a sequence. Each time, the peak file was updated with new peaks. Once all the step scans were checked, diffraction peaks that presumably might belong to the same lattice are obtained, as shown in Figure 27.

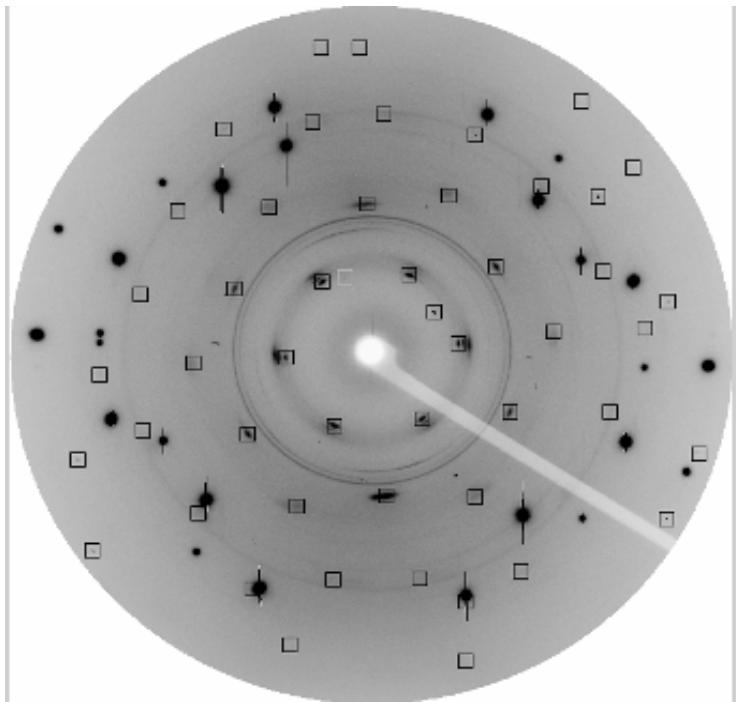


Figure 27. Final choice of Dy diffraction peaks in GSE.

The peak file from GSE was loaded into RSV. RSV provided a lattice representation of the peaks picked, Figure 28, page 57.

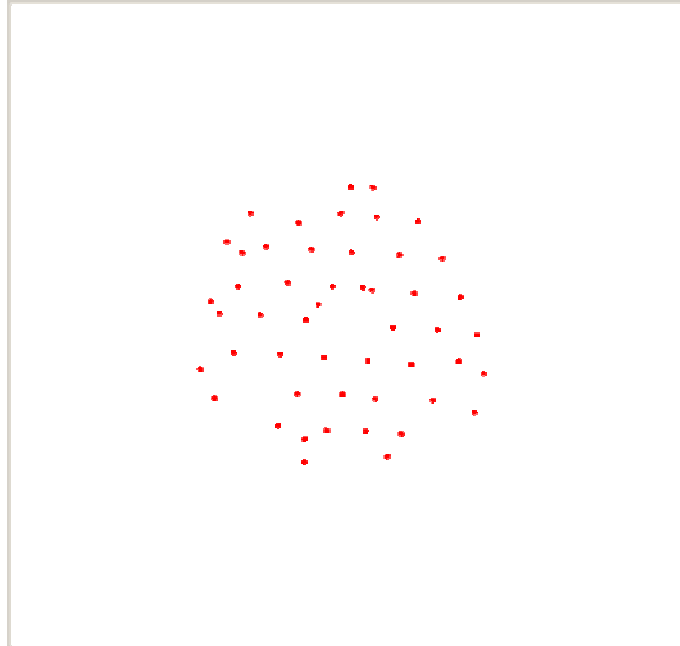


Figure 28. RSV lattice representation of CCD recorded diffraction peaks.

Once the initial peak list was loaded in RSV, one could try fitting the trial cell for the diffraction pattern observed. It is reported [4, 25, 26] that at ambient conditions Dy assumes hexagonal symmetry, which is, also apparent from the 2.74 GPa observed diffraction pattern. Therefore, the natural choice of a trial metric would be hexagonal, too. To get the trial cell constants, three, non-coplanar, short, reciprocal space vectors from the crystal lattice in RSV were picked. This should, in principle, allow for the definition of sufficiently small 3D rhomb that can be used to recreate the primitive lattice. Four reflections points in RSV are selected, where one point is fixed, while the other three were used to define reciprocal space axes. Once the reciprocal axes were defined, the RSV provided **UB** matrix and initial cell constants. The **UB** matrix established

correspondence between coordinates of reciprocal lattice points in orthogonal coordinate systems of an X-ray beam and the oblique system of the Dy sample. The **UB** matrix and initial unit cell are then transformed in separate Bruker Co. software using the standard hexagonal cell settings:  $a = b < c$ ,  $\alpha = \beta = 90^\circ$ , and  $\gamma = 120^\circ$ . The transformed matrix is re-loaded in RSV. The length threshold of 0.15-0.2 Å for the reciprocal space vectors is defined and a check was made for a number of reflections inside the threshold. Reflection statistics for an initial **UB** matrix and cell constants fit is shown in Figure 29.

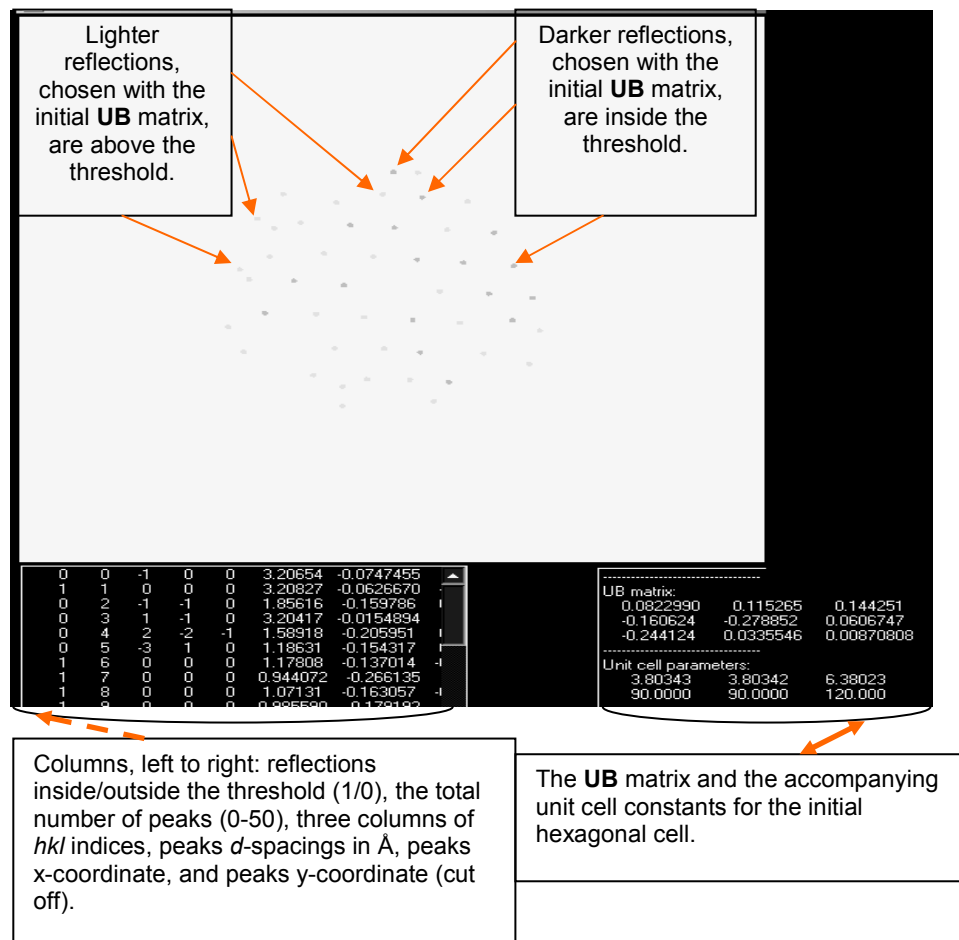


Figure 29. Lattice constants and reflections chosen in RSV for the initial fit of a hexagonal unit cell.

The peak list and corresponding **UB** matrix with initial cell constants were saved in separate files in RSV. The peak list saved was then laid over the sweep scan diffraction image in GSE.

With the new peak file loaded in GSE, the initial  $\omega$  values for each of the peaks chosen was displayed. This meant one could go to an individual frame of the respective  $\omega$  oscillation diffraction pattern (step scan), where peak maxima occurred and verify that the maxima really occurred in that frame and not in the neighboring frames. Also, one could check if there were any peaks in the respective individual frames that one did not select beforehand that belonged to a crystal lattice. Afterwards refinement of  $\omega$  on all the peaks chosen is done using the GSE  $\omega$  refinement automatic option. This refined peak list was saved and loaded back into RSV.

Once in RSV, the initial choice for the unit cell was refined, using the least square fit routines for the peaks Cartesian coordinates. Because of small statistical sample of reflections indexed and large uncertainties in refined unit cell constants, for all four pressure points, 0-4 GPa, for this Dy sample, the automatic indexing was considered inconclusive. Therefore, the manual indexing was attempted to index diffraction reflections and calculate unit cell constants. The final refinement for the unit cell of a Dy sample at 2.74 GPa is shown in Figure 30, page 60.

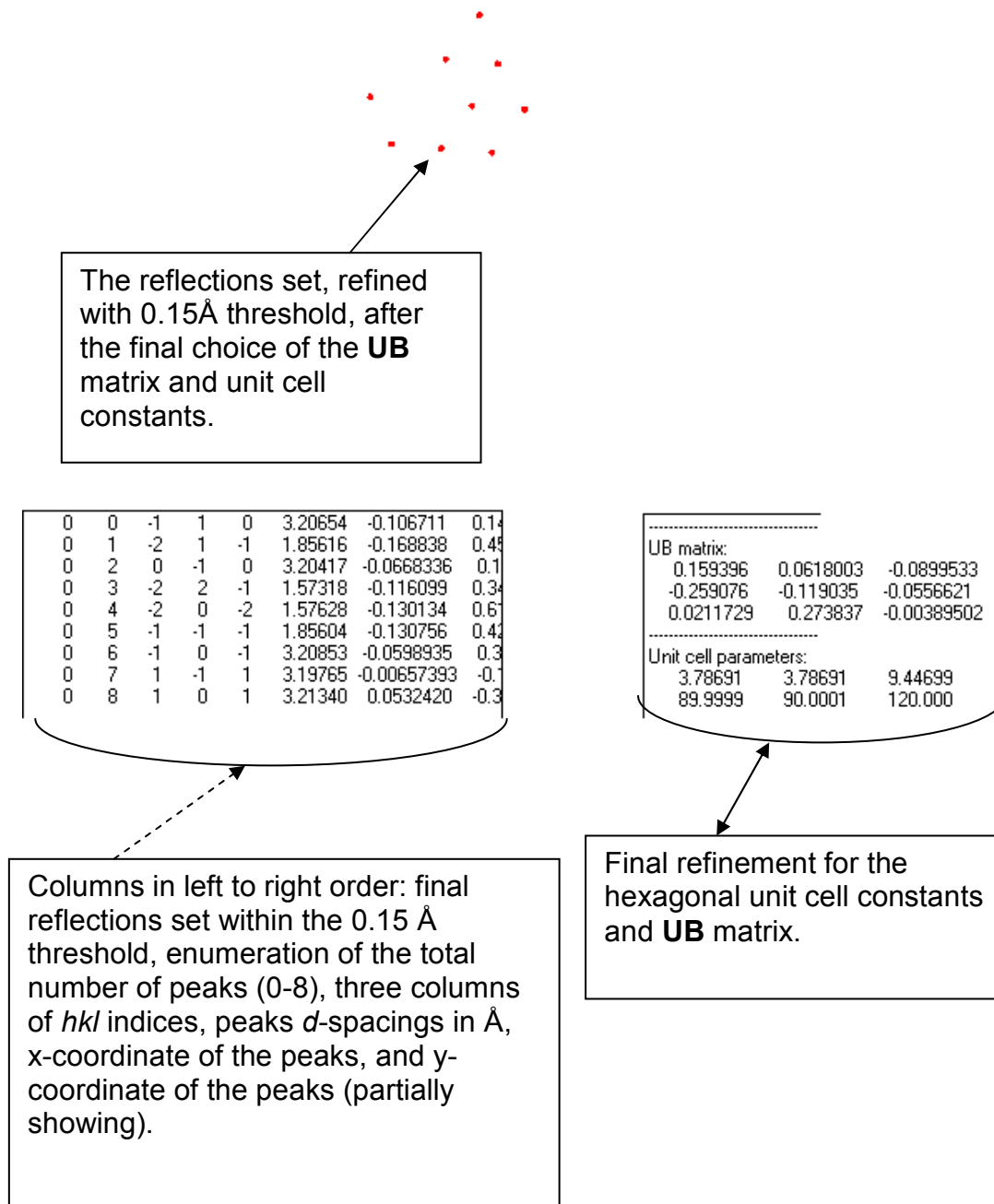


Figure 30. Lattice constants and reflections chosen in RSV for the final fit of a hexagonal cell. The final lattice reflection set with a refinement threshold of 0.15 Å is marked by the solid arrow. The table on the lower left hand side is indicated by the dashed arrow and explained in the accompanying text box. The entries on the lower right hand side are the final unit cell constants for the Dy diffraction pattern at 2.74 GPa and are indicated by the double arrow.

Refinement of the unit cell in GSE and RSV was, also, tried for new Dy sample, with the diffraction pattern taken in 1 GPa increments, for pressures ranging from 0-9 GPa. For the unit cell constants in the 0-5 GPa range, the values obtained for this sample were comparable to values from the previous sample for the similar pressure range of 0-4 GPa. The crystal quality of the new sample deteriorated with the pressures above 5 GPa, which was apparent in further broadening and splitting of peaks. This reflection broadening is a result of a coarse mosaic structure of the sample. It is, also a cause of an appearance of partial rings in the sample diffraction pattern, characteristic to powder diffraction. Also, poor peak shapes due to the crystal mosaicity reduced the accuracy of the cell parameters and of the orientation matrix. Therefore, using GSE and RSV, did not allow for refinement of any unit cell constants for the 6-9 GPa pressures. The manual refinement of the unit cell constants for these pressures is also tried, which is reported on later in the text.

#### Manual Indexing for the Dy Sample from 0 to 4 GPa

As stated in the previous section, at first, all of the diffraction patterns of this sample were analyzed in GSE and RSV software. This analysis yielded ambient pressure Dy unit cell constants indicating double hexagonal close packing structure. These unit cell values were in disagreement with the reported hexagonal unit cell values [27]. For this reason, a manual indexing on 0-4 GPa Dy data sets was tried to check the ambient unit cell constants obtained from refining with RSV software.



To manually index this crystal, it was necessary to use GSE and Powder Cell. The GSE/RSV software provided  $d$ -spacing values for each of the diffraction peaks from the CCD image. The Powder Cell software provided  $d$ -spacings and the accompanying  $hkl$  indices allowing to reconstruct reciprocal space vectors,  $\mathbf{r}_{hkl}$ , for the Dy powder diffraction standard. Using a quadratic form of the Bragg equation for a hexagonal crystal lattice which relates the  $d$ -spacing of diffracted peaks, the accompanying  $hkl$  indices, and the unit cell constants, one could calculate the constants using:

$$\frac{1}{d^2} = \frac{4}{3} \left[ \frac{(h^2 + k^2 + hk)}{a^2} \right] + \left( \frac{l^2}{c^2} \right) \quad (11)$$

Manual indexing was started by choosing reciprocal space hexagonal coordinate axes  $\mathbf{a}$  and  $\mathbf{b}$  ( $\mathbf{a}_1$  and  $\mathbf{a}_2$  in hexagonal notation),  $120^\circ$  apart, and drawing them on the print out of the 2.74GPa Dy crystal diffraction pattern, as shown in Figure 31, page 63. The CCD pattern had enough diffraction information to start manual indexing on  $\mathbf{a}$ ,  $\mathbf{b}$ -axes. From there on, one could add the reciprocal space vectors of the two reflections and follow it to a third one for the reflections that had  $hk.0$ ,  $h0.0$ , or  $0k.0$  indices, full arrows in Figure 31, page 63. The information for  $\mathbf{c}$ -axis, which is perpendicular to the  $\mathbf{a}$ - $\mathbf{b}$  plane, could not be readily identified from the diffraction pattern. Therefore one had to look in diffraction pattern for the peaks that were off of the  $\mathbf{a}$ - $\mathbf{b}$  grid. If one did find a diffraction peak that was just off either  $\mathbf{a}$  or  $\mathbf{b}$ -axis, like the peaks pointed to by

dashed arrows in Figure 31, below, this peak is considered a candidate for the reflection with a possible **c**-axis index. Because there was limited *d*-spacing information in the **a-b** plane, **c**-axis information from the diffraction pattern had to be limited, too. After a few peaks were picked, the observed *d*-spacings of these peaks are compared to the reported peaks *d*-spacings, from the standard pattern, with *hkl* indices where *l* is not zero. If the observed and reported *d*-spacings of the peaks matched within the error in broadness of the peaks, which was within one in thirty parts, one had an *l* index for the chosen peaks. After all the available peaks are indexed, the unit cell constants are calculated.

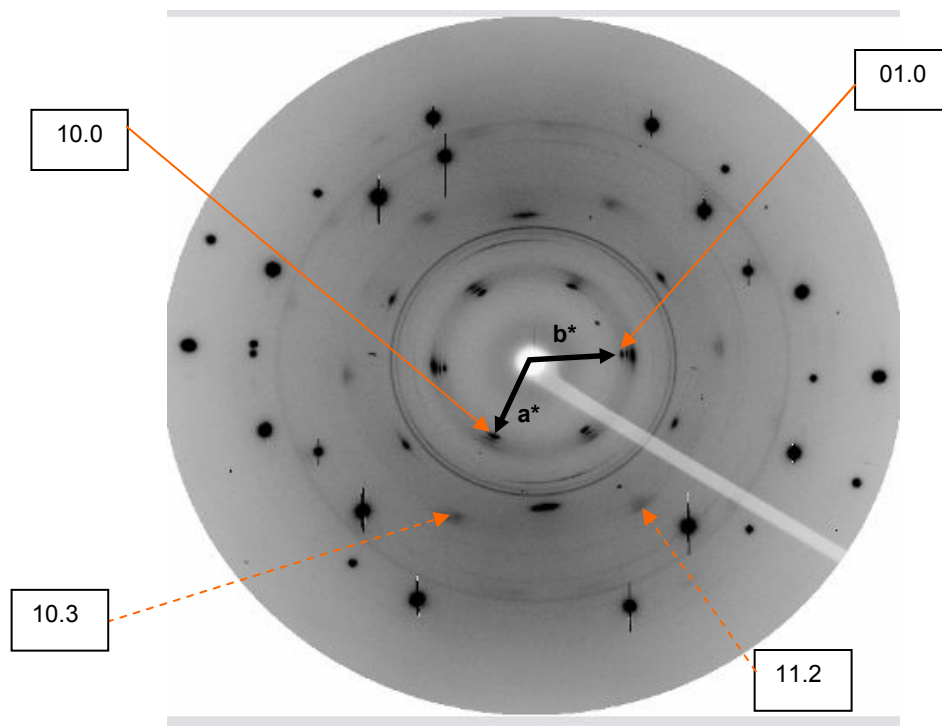


Figure 31. CCD image of diffraction pattern of Dy crystal in the DAC at 2.74GPa with a few indexed peaks. The **a\*** and **b\***-axes are defined, as shown. The peaks that lie on the axes are pointed to by arrows. The peaks that have **c\***-axis component are pointed to by the dashed arrows.

To calculate  $a$  and  $c$  values for an ambient phase Dy unit cell the formula (11) was used. The few calculated values for  $a$  and  $c$  were presented in Table 2. The calculated and least square refined unit cell constants for Dy ambient phase from all the manually indexed peaks in 0-4 GPa diffraction patterns are presented in CHAPTER 4, Reported Results section.

Table 2. Calculated unit cells constants with the accompanying errors from few indexed peaks for hexagonal metric of 2.74 GPa diffraction pattern.

$hkl$	Calculated $a$ (Å)	Reported $a$ (Å)	Error in $a$ ( $\sigma$ )
10.0	3.615	3.5903	0.007
11.0	3.70	3.5903	0.03
20.0	3.67	3.5903	0.02
$hkl$	Calculated $c$ (Å)	Reported $c$ (Å)	Error in $c$ ( $\sigma$ )
00.2	5.74	5.6475	0.02
10.3	5.58	5.6475	0.02
11.2	5.56	5.6475	0.02

#### Manual Indexing for the Dy Sample from 6 to 9 GPa

The indexing of the diffraction patterns in this pressure range with GSE and RSV software did not produce any reasonable unit cell refinements. So manual indexing was tried for the first reported high pressure phase of Dy, which forms between 6-7 GPa [1, 4, 25]. This phase is of the Sm (Samarium)-type, a rhombohedral unit cell symmetry. A 7.8 GPa diffraction pattern was picked for

manual indexing, as, upon visual inspection, exhibited the sharpest peak definition, compared to the other three diffraction patterns at 6, 8, and 9 GPa. This particular Dy sample was not the same as the one for which manual indexing was done for the ambient phase. This sample was bigger, about 50+ microns in length and consisted of at least 5-6 crystals of different orientation. The sample had very broad, poorly constrained reciprocal space profiles of diffraction peaks, as shown in Figure 32, below. Due to the broadness of peaks, unfavorable sample orientation, and the presence of more than one crystal in the sample, one couldn't readily observe the unit cell of the crystal structure in an CCD image.

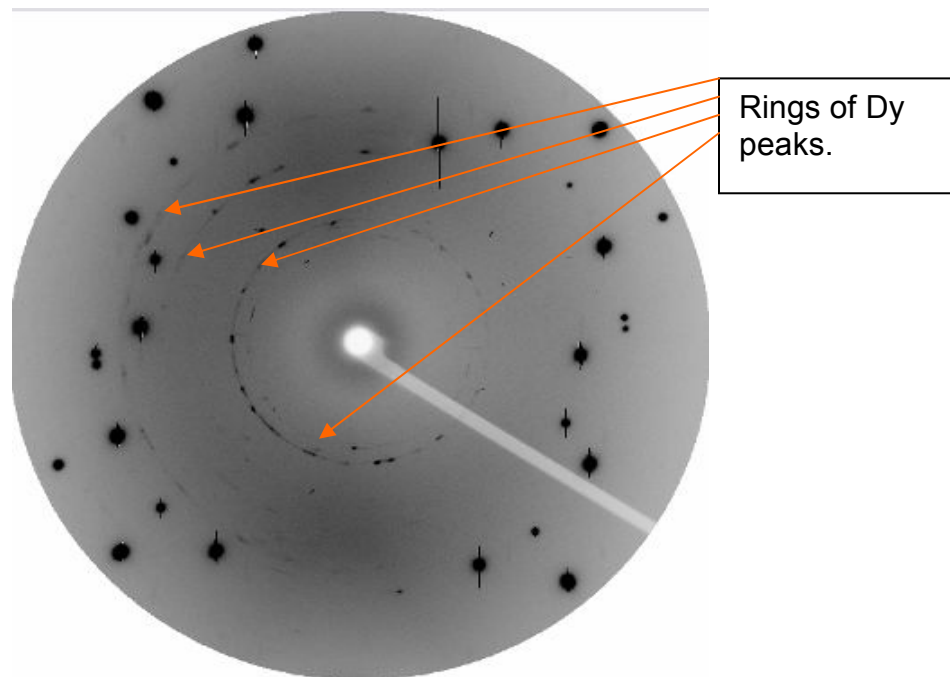


Figure 32. CCD image of the diffraction pattern of multi Dy crystal sample at 7.8GPa. Rings of Dy peaks are labeled by arrows. The round, oversaturated dots are the diffraction pattern from the diamonds. The small peaks are the diffraction pattern of ruby. The white, rectangular shape across is a shadow of the beam stop.

The idea for manual indexing was the same as for the ambient phase: Find the **a** and **b**-axes and add reciprocal space vectors  $\mathbf{r}^*_{hkl}$  to get as many as possible peaks with *hk* information. Afterwards, look for peaks that might have a **c**-axis component. From *Shen et al* publication [25], corresponding *d*-spacings for the powder diffraction data around 7GPa are obtained. These *d*-spacings were used to cross check the *d*-spacings observed from my pattern. Because rhombohedral and hexagonal unit cells define the same three-dimensional mathematical lattice, one could choose which set of crystallographic axes to use for the indexing. The hexagonal lattice reciprocal axes convention was chosen.

Before starting manual indexing, to get preliminary *hkl* indices accompanying the observed peaks *d*-spacing values, the observed *d*-spacings were compared with the published powder diffraction *d*-spacings. Upon comparing, in general, a large disagreement with the published *d*-spacings was noted. That was especially evident for the *d*-spacings  $> 2\text{\AA}$ , for which there was no agreement whatsoever with the published data.

Because of this disagreement, one did not know what unit cell symmetry could be fitted to diffraction pattern, so unit cells for all the seven crystal classes possible were considered for a fit. Triclinic and monoclinic cells were immediately eliminated as manual indexing candidates, because due to the low symmetry of these lattices many fits for the unit cell constants would be possible and therefore unreliable. The first unit cell for which manual indexing was tried was the orthorhombic one. To fit a unit cell for the orthorhombic lattice, six sets of peaks were picked, each set having two peaks of similar *d*-spacings, for a total

of twelve peaks, as shown in Figure 33, below. Two peaks of similar  $d$ -spacings were picked for better error statistics. Next, all of the twelve reciprocal space vectors were squared, i.e. reciprocal of  $d$ -spacings was squared for the twelve reflections picked from Figure 33, below. Then, any two reciprocal space vectors,  $\mathbf{r}^*_{hkl}$  and  $\mathbf{r}^*_{HKL}$  from the set of twelve  $\{\mathbf{r}^*_1, \dots, \mathbf{r}^*_{12}\}$ , were picked. Using Pythagorean Theorem,  $\mathbf{r}^*_{hkl}$  and  $\mathbf{r}^*_{HKL}$  were subtracted to see if a result would be a third reciprocal space vector that belonged to the set.

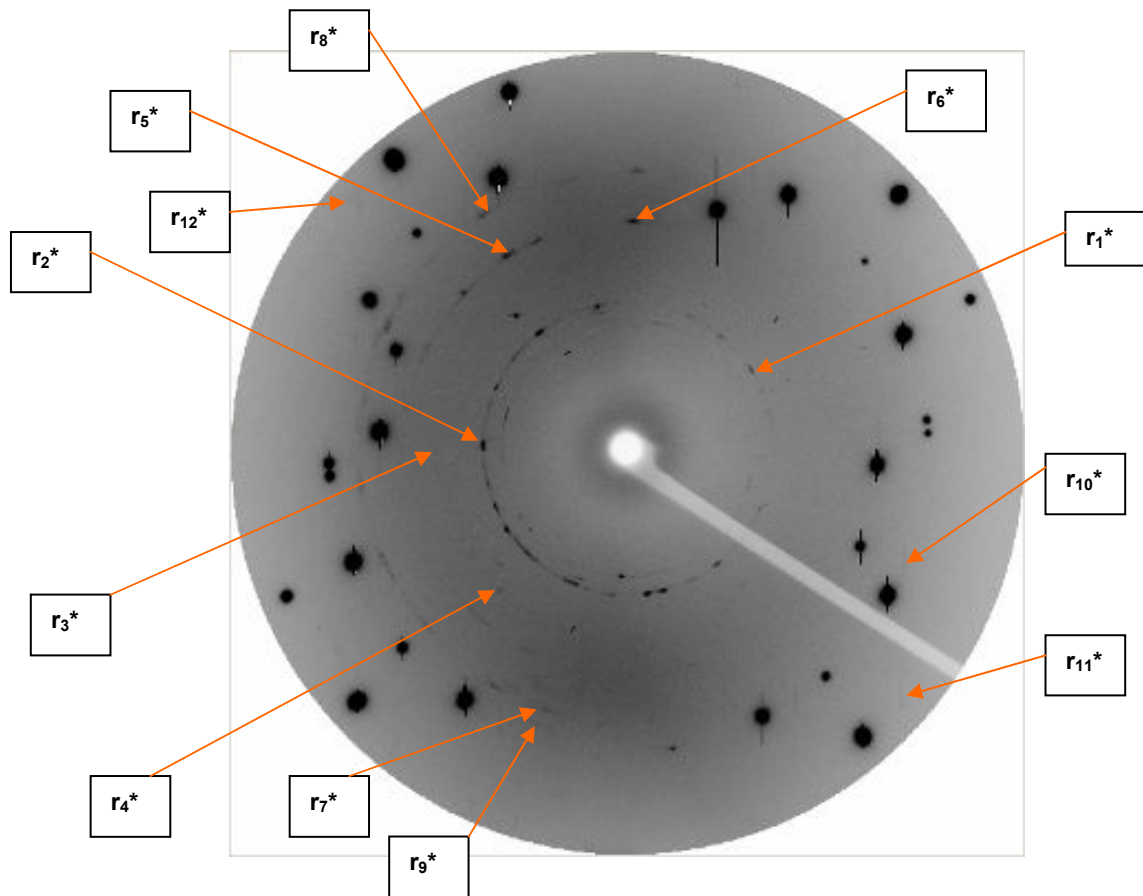


Figure 33. The set of peaks used in the manual indexing of the 7.8GPa diffraction pattern. Each peak has associated  $\mathbf{r}^*$  indicated. The round peaks are diamond diffraction pattern. The small peaks are ruby diffraction pattern. The rings interspersed with peaks are the diffraction pattern from the Dy sample.

So one reciprocal space vector, for example  $\mathbf{r}_{hkl}^*$  would be subtracted from the other eleven, with each resulting vector from the subtractions checked to see if it belonged in the set. This was repeated for the rest of the vectors in the set, until all the possible vector differences were exhausted. All the vectors' differences were then compared for equality. If any of these differences were the same, this meant that there was a single reciprocal space vector resulting from the subtraction of different couples of vectors, for ex.  $(hkl)_1 \equiv (230) - (HKL)_2 \equiv (120) = h-H, k-K, l-L$   $(110) = (hkl)_3 \equiv (310) - (HKL)_4 \equiv (200)$ , etc. Finding such differences also could provide  $hkl$  indices for the reflections associated with the set of vectors  $\{\mathbf{r}_{1}^*, \dots, \mathbf{r}_{12}^*\}$ . At the end no such identical differences were found from subtraction of the vectors belonging to the  $\{\mathbf{r}_{1}^*, \dots, \mathbf{r}_{12}^*\}$  set. Geometrically, the orthorhombic lattice is a base for higher symmetry lattices: tetragonal and cubic. This meant that one could disqualify tetragonal and cubic systems as possible unit cells for the single crystals of this sample.

Next, manual indexing was tried for both hexagonal and rhombohedral unit cells. Having a lot of individually oriented crystals in the sample prevented one from finding different  $hk$  spots from the  $\mathbf{a}-\mathbf{b}$  plane of a single crystal, when the manual indexing for the hexagonal cell was tried. The rhombohedral unit cell defined on hexagonal axes has the reflection constraint, which, in turn could make examined diffraction pattern more tractable for manual indexing. The constraint was:  $(-h + k + l) = 3 * n$ , where  $l = 0$  and  $n$  is an integer. So for a given rhombohedral unit cell on hexagonal axes it was found [28] that only two reflections could be observed with  $\frac{(-h + k)}{3} = n$ , namely: 11.0 and 30.0. This

meant that on the diffraction pattern a majority of the peaks had some type of **c**-axis information in them. As in the case of the ambient phase, one needed to first define the **a-b** plane before one could try to work on determining the **c** component of the peaks. So, one of the reciprocal space vectors was picked, for ex.  $\mathbf{r}_1^*$  and ratios of it with the rest of the eleven vectors were calculated, i.e.  $\mathbf{r}_1^*/\mathbf{r}_2^*$ ,  $\mathbf{r}_1^*/\mathbf{r}_3^*$ , etc., Table 3.

Table 3. Ratios of  $|\mathbf{r}_1^*|/|\mathbf{r}_1^*|, \dots, |\mathbf{r}_{12}^*|$  for the twelve peaks chosen.

$i$	$(\mathbf{r}_1^*)^2 = (d_i)^{-2} (\text{\AA})^{-2}$
$(\mathbf{r}_1^*)^2$	1
$(\mathbf{r}_2^*)^2$	0.9881
$(\mathbf{r}_3^*)^2$	0.5689
$(\mathbf{r}_4^*)^2$	0.5940
$(\mathbf{r}_5^*)^2$	0.4291
$(\mathbf{r}_6^*)^2$	0.4332
$(\mathbf{r}_7^*)^2$	0.3037
$(\mathbf{r}_8^*)^2$	0.3022
$(\mathbf{r}_9^*)^2$	0.2764
$(\mathbf{r}_{10}^*)^2$	0.2568
$(\mathbf{r}_{11}^*)^2$	0.1770
$(\mathbf{r}_{12}^*)^2$	0.1703



The ratios were obtained for each of the twelve  $\mathbf{r}^*$  vectors. Once all the ratios were calculated, all of the ratios were checked if any were integer multiple of three. Because of the constraint mentioned before, any such ratio would point to peaks lying in  $\mathbf{a-b}$  plane with allowed  $h$  and  $k$  indices satisfying

$$\frac{h^2 + k^2 + hk}{H^2 + K^2 + HK} = 3n .$$
 No such a ratio was noted. This meant that one couldn't

proceed any further in manual indexing, as there was not enough  $\mathbf{a-b}$  interplanar angular information to identify peaks of a single crystal out of six or so present in my sample.

Because manual indexing on the 7.8 GPa diffraction pattern didn't work, the decision was made not to pursue any more manual indexing for 6, 8, and 9 GPa diffraction patterns. Although manual indexing provided no constrain on cell parameters for the 7.8 GPa pressure point, from data analysis tried and comparison of the diffraction patterns at 6 GPa and 0-5 GPa of the same sample it was reasonable to conclude that some type of a phase change was taking place after 6 GPa. But due to substantial disagreements between observed  $d$ -spacings and the published ones, one can't even speculate on the nature of an apparent phase transition which might or might not be Sm-type.

## CHAPTER 4

### DISCUSSION

#### Diffraction Peaks Splitting

Neither manual nor automatic single crystal data analysis provided indexing for a majority of the diffraction peaks because most of the peaks observed for 0-4 GPa diffraction patterns were split into doublets and triplets, Figure 34, page 72. This indicated that the Dy sample used in the diffraction experiment was a twinned crystal. To index the split peaks, the two-theta angular dimension of each of the observed peaks is used to obtain two-theta scans. Two-theta scans (described in CHAPTER 3) are two dimensional diffraction images integrated into one dimensional peak intensities as a function of diffraction angle. Indexing of the observed peaks was done in Jade, a commercially available indexing and unit cell refinement software from Materials Data Inc., customarily used for analyzing powder X-ray diffraction patterns. To index the peaks  $d$ -spacing is used, obtained from individual peaks two-theta scans. To index all observed peaks and reproduce twinning, a distorted Sm cell was constructed by subgroup chains. The symmetry metric fitting the structural distortion was found to be monoclinic. The monoclinic unit cell constants were derived according to the 1<sup>st</sup> Landau and Lifshiz criterion. The details of an indexing procedure are given in the further text.

According to the literature [1, 2, 3, 5, 9] the initial structure of the elemental Dy at ambient temperature is a regular hexagonal close-packed form where atomic positions in hexagonal cell are: (0.333, 0.666, 0.250) and (0.666, 0.333,

0.750) [12]. The Dy structure transforms  $\sim 7$  GPa [25] into the Sm-type structure. Because the indexing with hexagonal metric could not account for all the observed peaks, the Sm cell was chosen as an initial cell model for indexing all the peaks observed. To go from the  $P6_3/mmc$  to R-3m cell, the size of the **a**-axis of the hexagonal cell is kept while the **c**-axis of rhombohedral cell is increased four and a half times that of the hexagonal cell, with cell atomic positions at: (0, 0, 0), (0.222, 0.222, 0.222), and (-0.222, -0.222, -0.222) [10]. The **c**-axis increase in going from hexagonal to rhombohedral unit cell is a result of centering a rhombohedral cell at 0.333, 0.666, and 0.666 points in a hexagonal setting.

To start indexing, the set of doublet and triplet peaks is chosen from a diffraction pattern at 2.74 GPa (being a pattern with the most peaks observed), shown below.

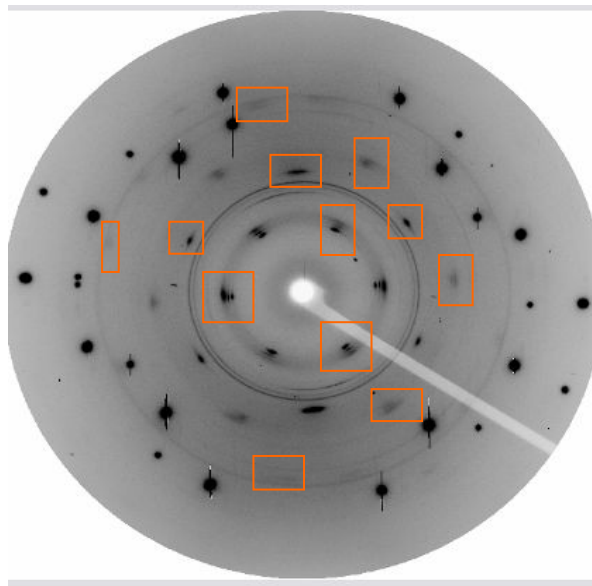


Figure 34. CCD image of a diffraction pattern of Dy crystal in the DAC at 2.74GPa with a few peak doublets/triplets chosen for indexing in Jade and indicated by with the boxes.

FIT2D software (described in CHAPTER 3) was used to generate the two-theta scans for each of the chosen peak doublets and triplets. The set of peak doublets/triplets is loaded into the FIT2D graphics viewing window. Then, using the ZOOM IN option available in the FIT2D window a smaller graphical display region was defined through the peak doublets/triplets. The zooming in is done to assure smooth integrated peak profiles in the two-theta scan. One such display is shown in Figure 35.

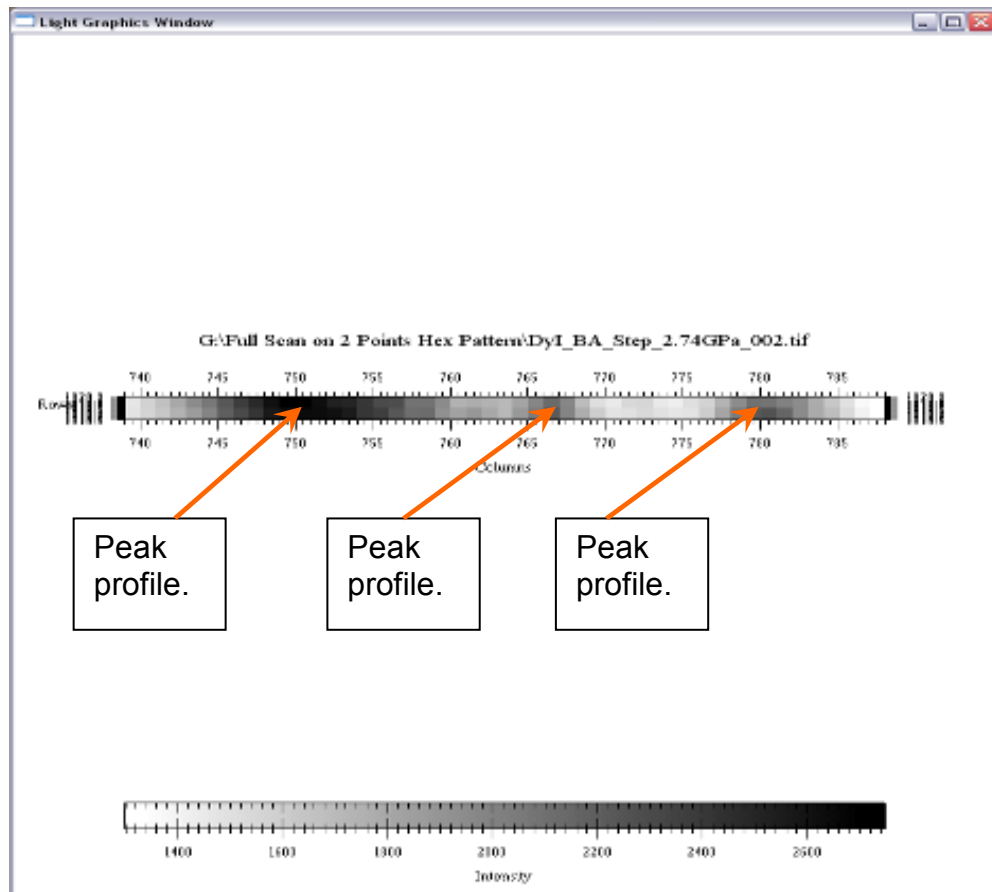


Figure 35. Small graphical display region in FIT2D of triplet of peaks from a diffraction pattern of the Dy crystal in the DAC at 2.74GPa. The peaks are labeled by text boxes.

Next, the diffraction geometry parameters obtained from calibration (described in CHAPTER 3) are loaded. The FIT2D INTEGRATE command is used to generate and display a two-theta scan for the peak triplet from Figure 35, page 73. The observed  $d$ -spacings for the peaks were determined. The two-theta scan is then exported to ASCII file format. Figure 36 shows the two-theta scan for the peaks from Figure 35.

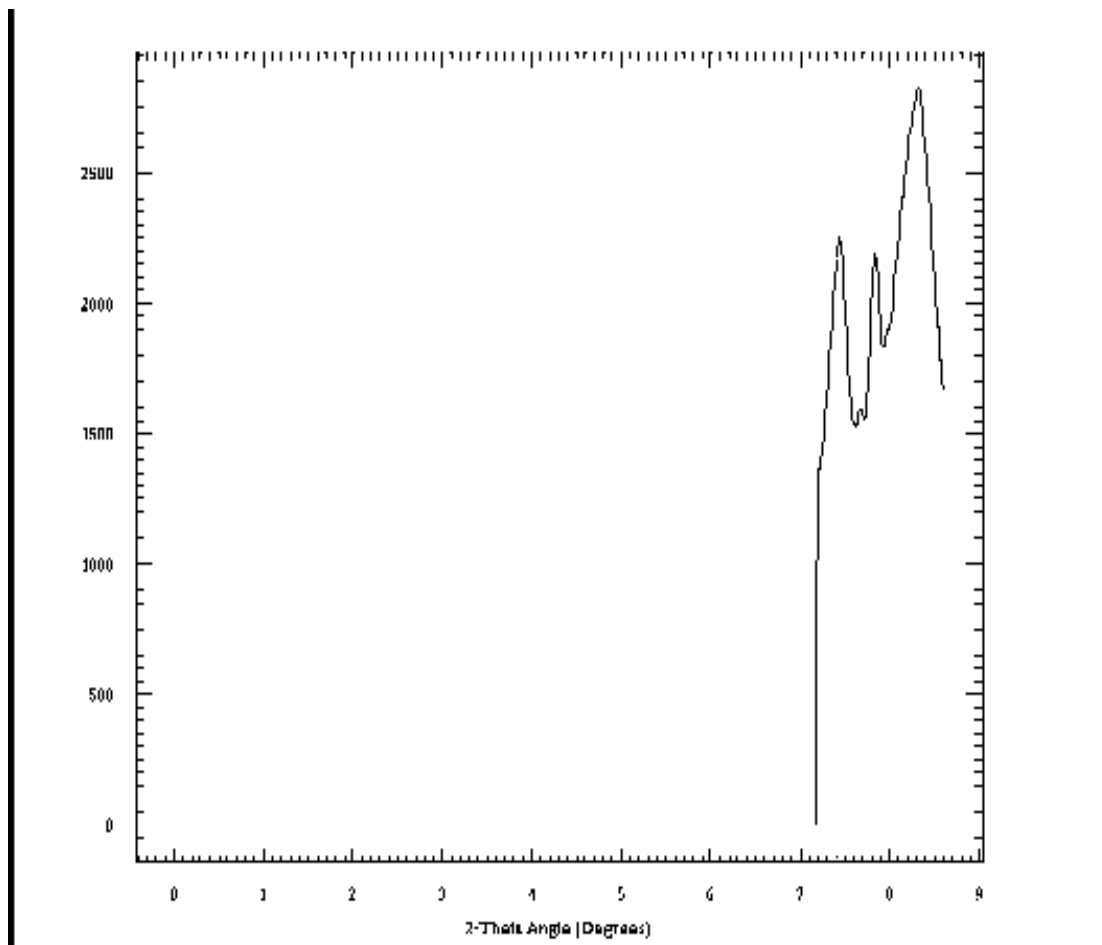


Figure 36. Two-theta scan in FIT2D of the three peaks from Figure 35. The  $d$ -spacings for each peak were obtained by positioning the cursor over the apex of the peak.

Next, a two-theta scan ASCII file is opened in the Jade graphic window, Figure 37, below.

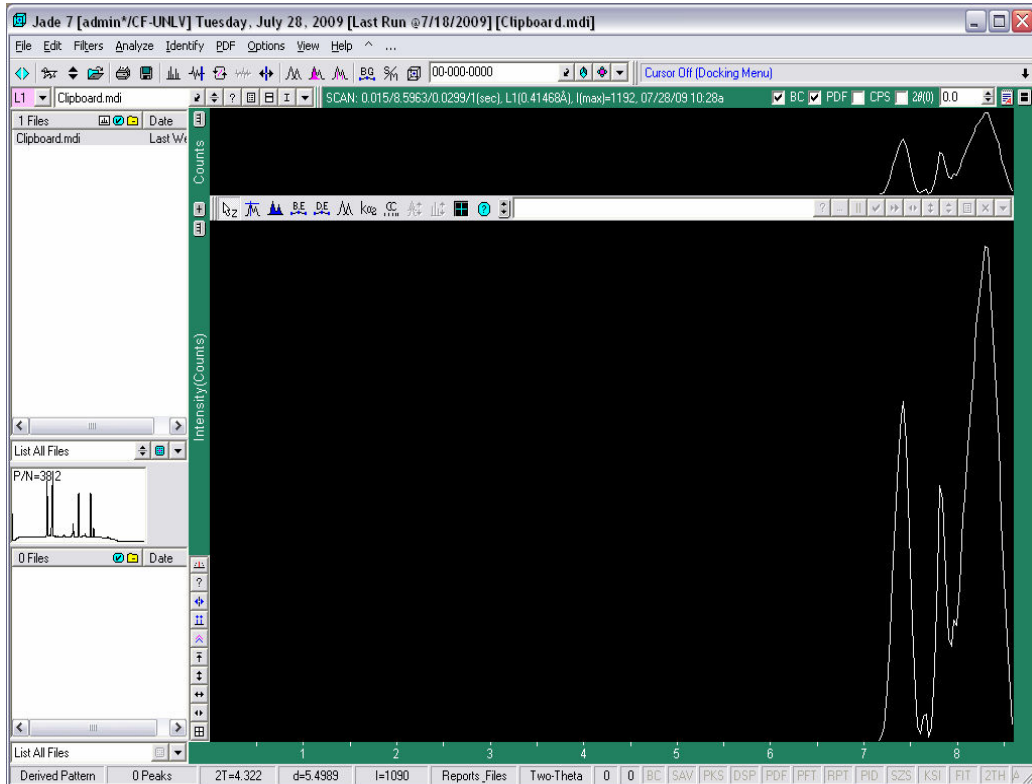


Figure 37.  $2\theta$  scan, background corrected, of the three peaks from Figure 35 displayed in the Jade graphic window.

The observed  $d$ -spacings obtained in FIT2D are then used to pick and label the diffraction peaks from Figure 35 in the Jade graphic window. The rhombohedral unit cell constants and angles were entered in the “Cell Refinement” window of the Jade graphic window and the initial set of  $hkl$  indices accompanying observed  $d$ -spacings of peaks are generated. The Jade graphic window, with “Cell Refinement” window, for the peak triplet from Figure 35 is shown in Figure 38.

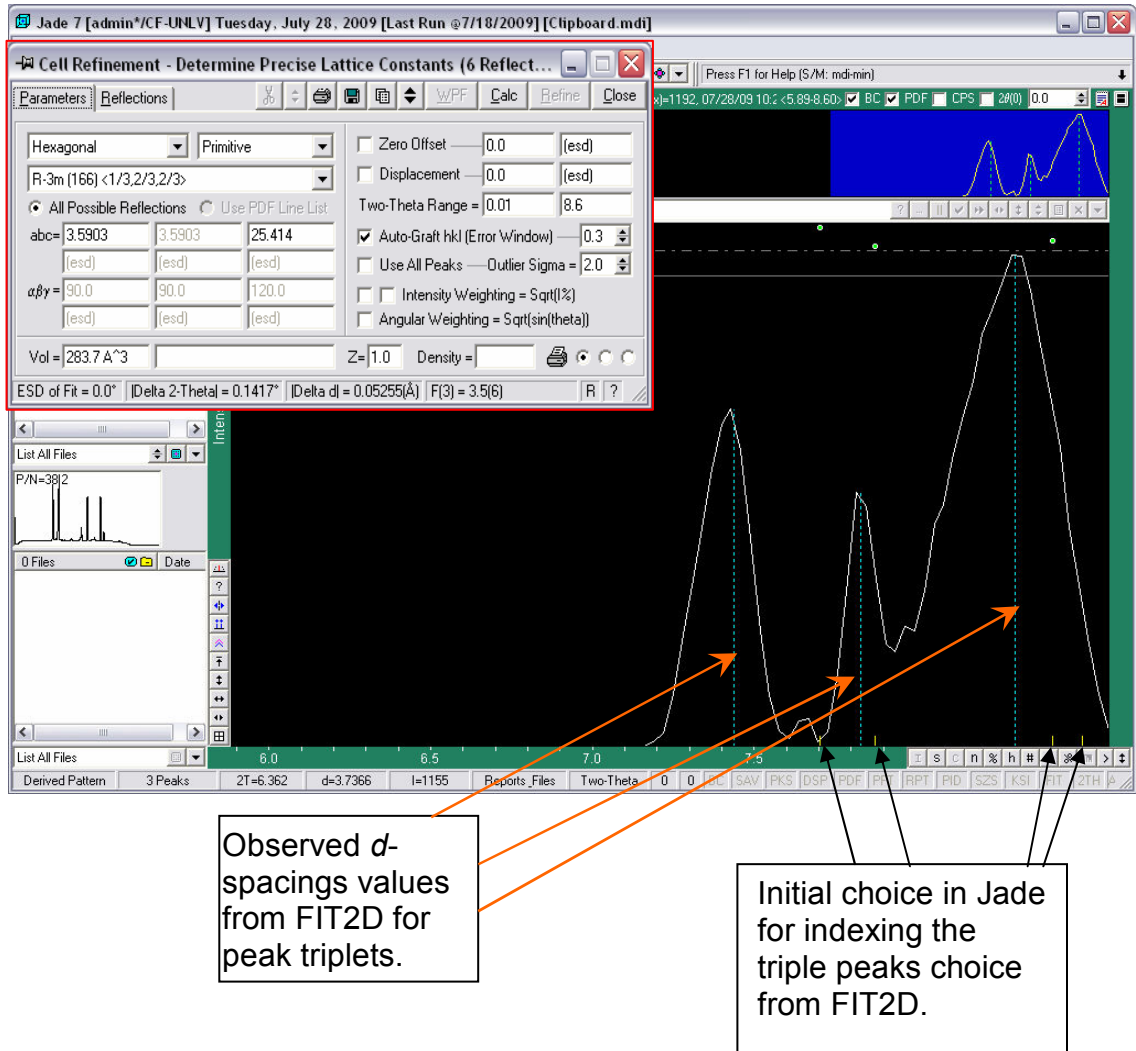


Figure 38. The initial indexing in Jade for Sm cell on the three peaks from Figure 35. The  $d$ -spacings of the peaks obtained from FIT2D are indicated by the orange arrows. The initial peaks indexing in Jade is labeled by the yellow tick marks, indicated by the black arrows. The peaks  $hkl$  indices are stored in the “Reflections” tab of the “Cell Refinement” window, labeled with a red border.

Procedure described in p. 72-75 above is then repeated; all the remaining chosen peak doublets and triplets from Figure 34, page 72 have the ASCII files of their two-theta scans generated, each of the ASCII files is opened in separate Jade graphic windows, and the initial set of  $hkl$  indices corresponding to

observed  $d$ -spacings of peak doublets and triplets are generated using a rhombohedral metric. Then, by adjusting the unit cell constants values in individual Jade graphic windows of the chosen set of doublets/triplets, observed  $d$ -spacings are matched to corresponding predicted  $hkl$  indices for Sm-type cell. With this approach, rhombohedral unit cell refinement and simultaneous indexing of all the picked sets of triplets/doublets from Figure 34, page 72 (12 sets in total) is tried. Since no cell refinement was found that could be used to index all sets of triplets/doublets, the rhombohedral metric could not be used to index all the observed diffraction peaks. However, all the predicted Sm cell  $hkl$  indices differed slightly from observed  $2\theta$  values. This small offset between observed and predicted  $d$ -spacings indicated that a distorted Sm cell could be used to index the observed peaks. To investigate symmetry metric relating to distorted Sm-type structure group-subgroup relationship was used.

For a particular family of related structures, the space group of highest symmetry within the family is identified as the *ideal type (aristotype)*. By removing a specific single symmetry element, from the *ideal type* as well as elements that are present as a combination involving the removed symmetry element, the maximal number of possible, if any, *subgroups* resulting from the deconstruction are identified. Often, the correct space group for a variant structure of lower symmetry can be found by examining the choice of *subgroups* given for the *ideal type*. Hence, to check for the structural relationship between the Sm-type and the lower symmetry cells, the possible subgroups of the Sm-type space group (space group number 166) are checked. The group-subgroup



theoretical relationship was investigated using the Bilbao Crystallographic Server [29] and the existence of only one such a relationship of index 3 (ratio of orders, number of symmetry elements, of a group and its subgroup) is found for the space groups numbers 166 (space group symbol  $R-32/m$ ) and 12 (monoclinic system, space group symbol  $C 1 2/m 1$ ). The group-subgroup relationship is shown in Figure 39.

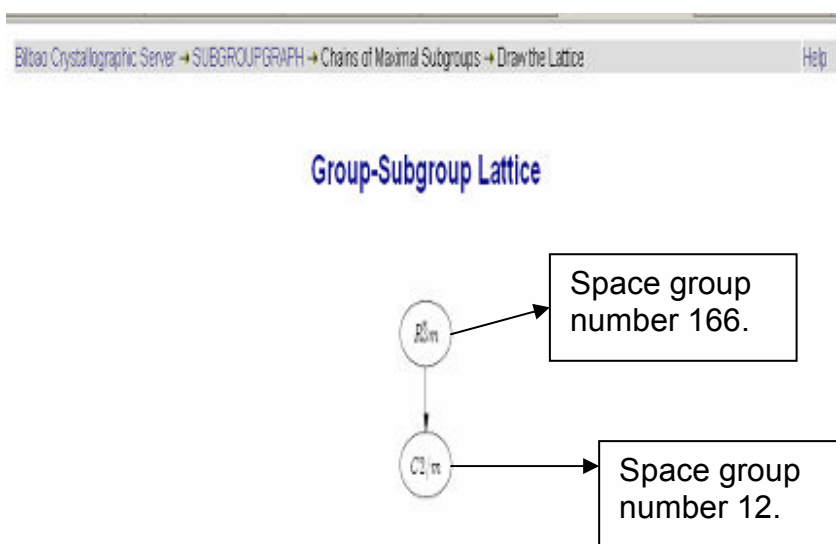


Figure 39. The group-subgroup relationship for the space groups 166-12. The group-subgroup relationship is indicated with an arrow between the two circles.

Therefore, the C-centered (a second lattice point is at the center of the face defined by the **a** and **b**-axes) monoclinic unit cell (the space group number 12, space group symbol  $C 1 2/m 1$ ) was used to index a majority of peaks (all but two observed peaks were not indexed). Afterwards, repeating the procedure described above in FIT2D and Jade, the indexing in monoclinic metric was done

for all the remaining pressure points. The indexing done in Jade for the peaks triplet from Figure 35 using a C-centered monoclinic cell is shown in Figure 40.

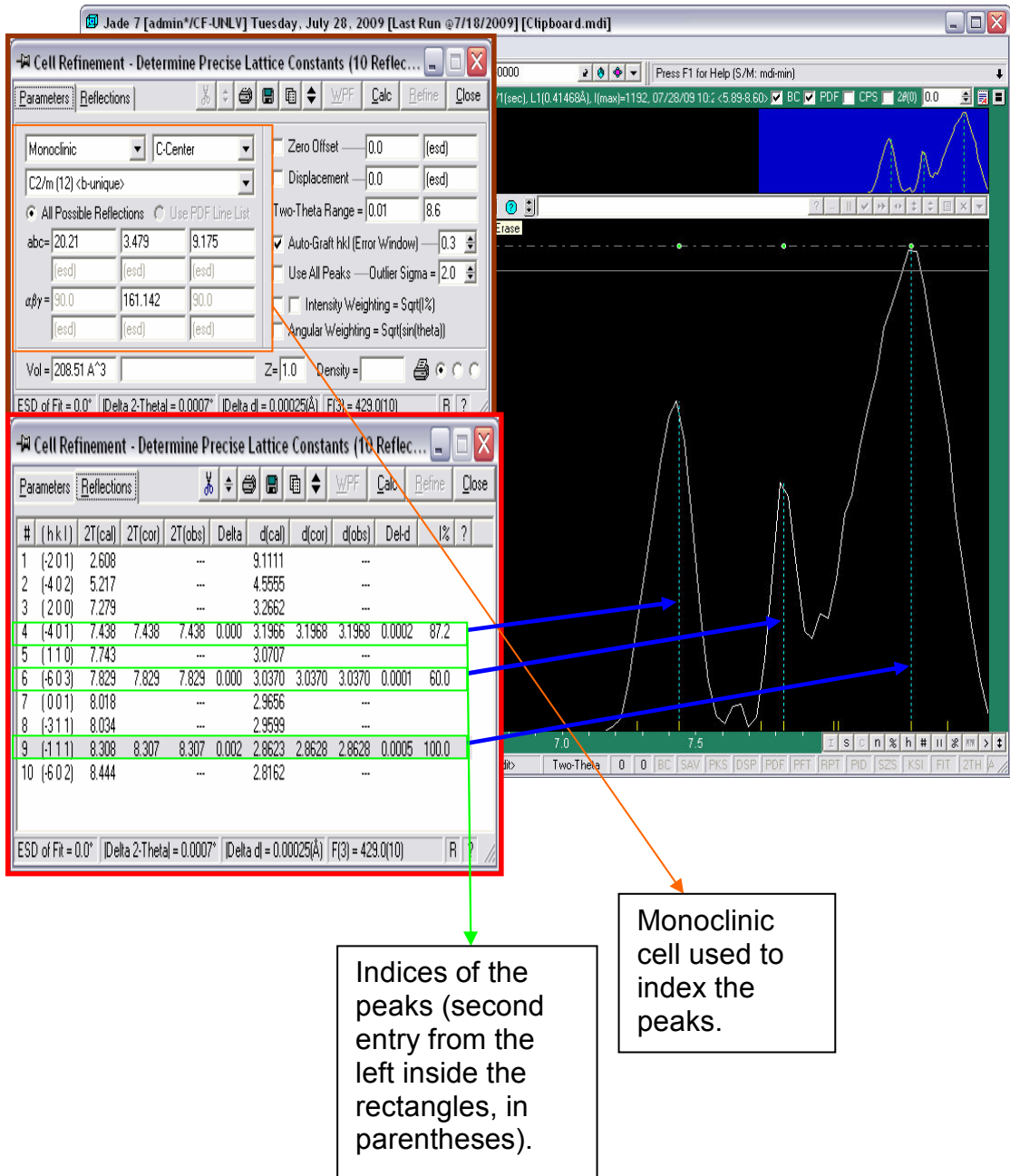


Figure 40. The final indexing in Jade for the Sm-type unit cell with a monoclinic distortion on the three peaks from Figure 35. The blue arrows indicate indexed peaks. The monoclinic cell constants and angles are indicated by orange arrow. Peak indices are indicated by green arrow.

## Reported Results

The peak indexing results are organized into two sections: results reported from manual indexing on a hexagonal metric done in CHAPTER 3 and results reported from the automatic indexing on a monoclinic metric in Jade, as written about in Diffraction Peaks Splitting section of this chapter. No results are reported on automatic indexing done with GSE and RSV software due to the inconclusiveness of indexing done in RSV software, which is a consequence of inability of GSE/RSV to deal with twinned diffraction patterns observed for the 0.7-3.8 GPa pressure regime.

### Results for Manual Indexing

The manual indexing was done for a 0.7-3.8 GPa pressure range, as described in CHAPTER 3. Diffraction peaks  $d$ -spacings, and indices for each pressure point are organized in the tables and together with accompanying pseudo-hexagonal unit cell constants, are presented under the separate headings. The reported unit cell constants for Dy ambient phase are:  $a = 3.5903$  Å and  $c = 5.6475$  Å and reported ambient pressure  $V = 63.0447$  Å<sup>3</sup> [27]. Note: The ambient pressure diffraction pattern for this particular sample was never collected due to a collapse of the gasket chamber upon release of pressure in the Four Pin cell.

## 0.7 GPa Diffraction Pattern

Experimental data shown in Table 4 below:

Table 4. Indexed peaks in 0.7 GPa diffraction pattern with accompanying errors in observed and reported  $d$ -spacings.

Pressure = 0.70±0.01 GPa			
$hk.l$	Observed $d$ -spacings (Å)	Reported $d$ -spacings (Å)	Error in $d$ -spacings ( $\sigma$ )
100	3.21	3.10929	0.03
-100	3.18	3.10929	0.02
103	1.601	1.61035	0.006
200	1.59	1.55465	0.02
-200	1.60	1.55465	0.03
203	1.204	1.19872	0.004
300	1.07	1.03643	0.03
-300	1.07	1.03643	0.03

The unit cell constants and unit cell volume with corresponding uncertainties are refined using UnitCell software [30], which implements the least square refinement on  $d$ -spacings of indexed diffraction peaks to obtain unit cell constants. The refined pseudo-hexagonal unit cell constants are:  $a = 3.7\pm 0.1$  Å,  $c = 5.58\pm 0.05$  Å; with  $\alpha = \beta = 90^\circ$ , and  $\gamma = 120\pm 3^\circ$ . The refined unit cell volume is  $V = 66\pm 1$  Å<sup>3</sup>.

## 1.74 GPa Diffraction Pattern

Experimental data shown in Table 5 below:

Table 5. Indexed peaks in 1.74 GPa diffraction pattern with accompanying errors in observed and reported  $d$ -spacings.

Pressure = 1.74±0.02 GPa			
$hk.l$	Observed $d$ -spacings (Å)	Reported $d$ -spacings (Å)	Error in $d$ -spacings ( $\sigma$ )
100	3.14	3.10929	0.01
-100	3.14	3.10929	0.01
103	1.600	1.61035	0.006
110	1.783	1.79515	0.007
112	1.54	1.51493	0.02
200	1.59	1.55465	0.02
-200	1.558	1.55465	0.002
203	1.200	1.19872	0.001
300	1.07	1.03643	0.03
-300	1.07	1.03643	0.03

The pseudo-hexagonal unit cell constants, refined using UnitCell software are:  $a = 3.66 \pm 0.07$  Å,  $c = 5.60 \pm 0.04$  Å; with  $\alpha = \beta = 90^\circ$ , and  $\gamma = 120 \pm 3^\circ$ . The refined unit cell volume is  $V = 65 \pm 1$  Å<sup>3</sup>.

## 2.74 GPa Diffraction Pattern

Experimental data shown in Table 6 below:

Table 6. Indexed peaks in 2.74 GPa diffraction pattern with accompanying errors in observed and reported  $d$ -spacings.

Pressure = 2.74±0.03 GPa			
$hk.l$	Observed $d$ -spacings (Å)	Reported $d$ -spacings (Å)	Error in $d$ -spacings ( $\sigma$ )
100	3.131	3.10929	0.007
-100	3.126	3.10929	0.005
103	1.600	1.61035	0.006
110	1.780	1.79515	0.008
112	1.513	1.51493	0.001
200	1.59	1.55465	0.02
-200	1.557	1.55465	0.002
203	1.194	1.19872	0.001
210	1.19	1.1752	0.007
300	1.039	1.03643	0.002
-300	1.041	1.03643	0.004

The hexagonal unit cell constants, refined using UnitCell software are:  $a = 3.64 \pm 0.03$  Å,  $c = 5.5 \pm 0.2$  Å; with  $\alpha = \beta = 90^\circ$ , and  $\gamma = 120 \pm 3^\circ$ . The refined unit cell volume refined is  $V = 63 \pm 2$  Å<sup>3</sup>.

### 3.8 GPa Diffraction Pattern

Experimental data shown in Table 7 below:

Table 7. Indexed peaks in 3.8 GPa diffraction pattern with accompanying errors in observed and reported  $d$ -spacings.

Pressure = $3.80 \pm 0.08$ GPa			
$hk.l$	Observed $d$ -spacings ( $\text{\AA}$ )	Reported $d$ -spacings ( $\text{\AA}$ )	Error in $d$ -spacings ( $\sigma$ )
100	3.12	3.10929	0.01
-100	3.130	3.10929	0.007
110	1.75	1.79515	0.03
112	1.46	1.51493	0.03
200	1.543	1.55465	0.007
-200	1.550	1.55465	0.003

The hexagonal unit cell constants, refined using UnitCell software are:  $a = 3.63 \pm 0.04$   $\text{\AA}$ ,  $c = 5.3 \pm 0.3$   $\text{\AA}$ ; with  $\alpha = \beta = 90^\circ$ , and  $\gamma = 120 \pm 4^\circ$ . The refined unit cell volume is  $V = 61 \pm 2$   $\text{\AA}^3$ .

## Indexed Diffraction Pattern - Hexagonal Cell

An example for 2.74 GPa pressure point is shown below:

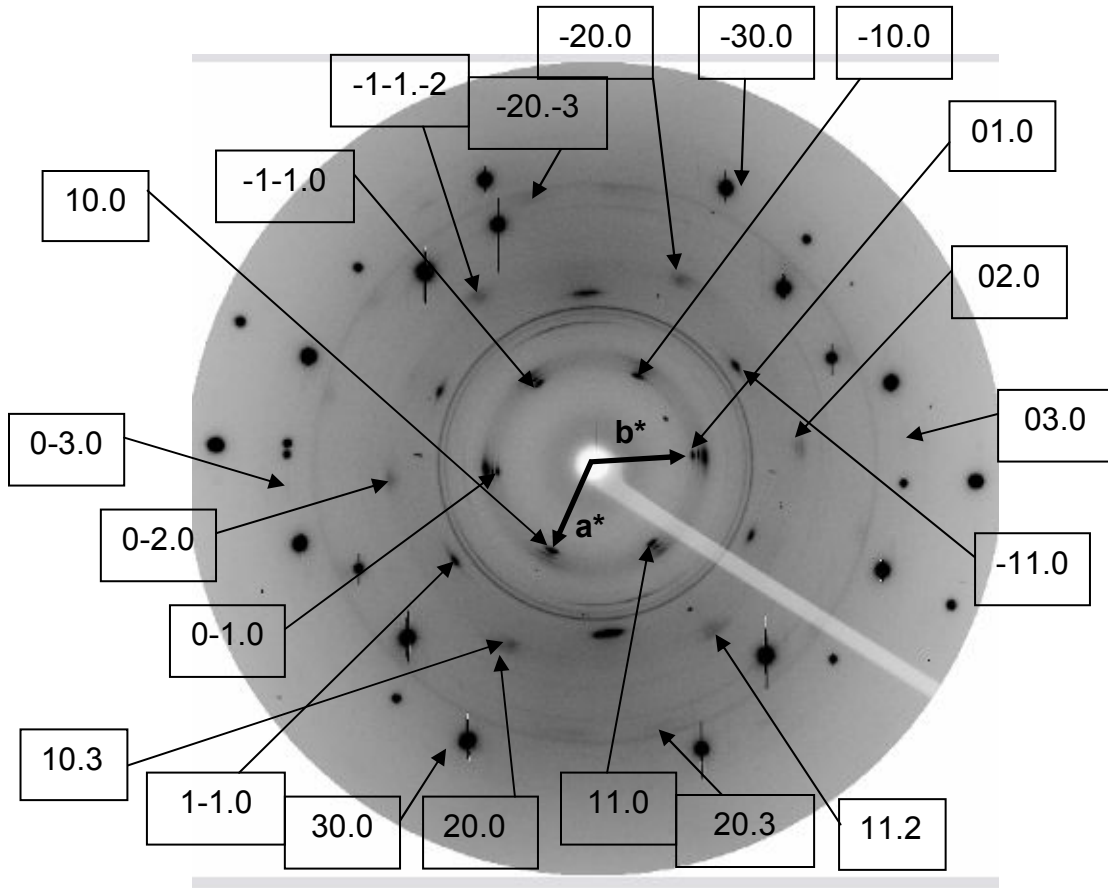


Figure 41. CCD image of a diffraction pattern of the Dy crystal in the DAC at 2.74GPa with majority of observed peaks, corresponding to pseudo-hexagonal symmetry of a twinned component, indexed manually. The peak indices are indicated by arrows and displayed in text boxes.

### Results for Indexing in Jade

The indexing was done in Jade for a 0.7-3.8 GPa pressure range, as described in this chapter. The monoclinic unit cell constants, diffraction peaks  $d$ -spacings, and indices for each pressure point are presented under separate



headings below. The reported unit cell constants for Dy ambient phase (metastable, Sm-type, becoming stable Sm-type at 7.5 GPa) are:  $a = 3.580 \text{ \AA}$  and  $c = 25.61 \text{ \AA}$  and reported ambient pressure  $V = 284.25 \text{ \AA}^3$  [31].

### 0.7 GPa Diffraction Pattern

Experimental data shown in Table 8 below:

Table 8. Indexed peaks in 0.7 GPa diffraction pattern with accompanying errors in observed and reported  $d$ -spacings.

Pressure = $0.70 \pm 0.01$ GPa			
$hkl$	Observed $d$ -spacings ( $\text{\AA}$ )	Reported $d$ -spacings ( $\text{\AA}$ )	Error in $d$ -spacings ( $2\sigma$ )
-401	3.2311	3.23296	0.0006
200	3.289	3.27846	0.003
001	2.9462	2.94462	0.0005
-914	1.887	1.88966	0.001
-511	1.874	1.87622	0.001
-11.15	1.609	1.60683	0.001
-715	1.2199	1.22018	0.0002
-603	3.231	3.24801	0.005
-111	2.885	2.90266	0.006
310	1.881	1.86896	0.007
-421	1.5744	1.57380	0.0004

The monoclinic unit cell constants, refined using UnitCell software are:  $a = 20.2 \pm 0.6 \text{ \AA}$ ,  $b = 3.60 \pm 0.02 \text{ \AA}$ ,  $c = 9.05 \pm 0.09 \text{ \AA}$ ; with  $\alpha = \gamma = 90^\circ$ , and  $\beta = 161.0 \pm 0.3^\circ$ . The refined unit cell volume is  $V = 214 \pm 9 \text{ \AA}^3$ .

### 1.74 GPa Diffraction Pattern

Experimental data shown in Table 9 below:

Table 9. Indexed peaks in 1.74 GPa diffraction pattern with accompanying errors in observed and reported  $d$ -spacings.

Pressure = 1.74±0.02 GPa			
$hkl$	Observed $d$ -spacings (Å)	Reported $d$ -spacings (Å)	Error in $d$ -spacings ( $2\sigma$ )
-401	3.214	3.22053	0.002
-603	3.042	3.01553	0.009
-111	2.8778	2.87938	0.0005
200	3.258	3.26192	0.001
001	2.9317	2.93049	0.0004
-914	1.88230	1.88221	0.00005
-511	1.864	1.86160	0.001
400	1.603	1.6212	0.009
310	1.875	1.86675	0.004
-2-20	1.5564	1.55672	0.0002

The monoclinic unit cell constants, refined using UnitCell software are:  $a = 20.2\pm 0.6$  Å,  $b = 3.54\pm 0.01$  Å,  $c = 9.0\pm 0.2$  Å; with  $\alpha = \gamma = 90^\circ$ , and  $\beta = 161.0\pm 0.4^\circ$ .

The refined unit cell volume is  $V = 209\pm 10$  Å<sup>3</sup>.

## 2.74 GPa Diffraction Pattern

Experimental data shown in Table 10 below:

Table 10. Indexed peaks in 2.74 GPa diffraction pattern with accompanying errors in observed and reported  $d$ -spacings.

Pressure = 2.74±0.03 GPa			
$hkl$	Observed $d$ -spacings (Å)	Reported $d$ -spacings (Å)	Error in $d$ -spacings ( $2\sigma$ )
-401	3.196	3.20049	0.002
-603	3.037	2.99295	0.009
-111	2.8623	2.88993	0.009
200	3.257	3.25044	0.002
110	3.0803	3.12021	0.01
001	2.92200	2.92180	0.00007
-914	1.8706	1.87005	0.0003
-511	1.85970	1.85976	0.00003
-11.15	1.599	1.60480	0.004
-421	1.565	1.56108	0.002
310	1.864	1.86682	0.002
-715	1.2103	1.20982	0.0003
-912	1.214	1.21851	0.004
400	1.6046	1.61741	0.008
220	1.56760	1.56765	0.00003
-401	3.232	3.21972	0.004
-311	3.053	3.02396	0.009
-602	2.893	2.87119	0.008
420	1.201	1.19958	0.001

The monoclinic unit cell constants, refined using UnitCell software are:  $a =$

$20.1\pm 0.8$  Å,  $b = 3.51\pm 0.03$  Å,  $c = 9.0\pm 0.2$  Å; with  $\alpha = \gamma = 90^\circ$ , and  $\beta = 161.0\pm 0.5^\circ$ .

The refined unit cell volume is  $V = 206\pm 7$  Å<sup>3</sup>.

### 3.8 GPa Diffraction Pattern

Experimental data shown in Table 11 below:

Table 11. Indexed peaks in 3.8 GPa diffraction pattern with accompanying errors in observed and reported  $d$ -spacings.

Pressure = 3.80±0.08 GPa			
$hkl$	Observed $d$ -spacings (Å)	Reported $d$ -spacings (Å)	Error in $d$ -spacings ( $2\sigma$ )
-401	3.199	3.20364	0.002
-111	2.851	2.85434	0.001
-914	1.8513	1.85104	0.0001
-511	1.8531	1.85177	0.0007
-11.15	1.583	1.58720	0.003
4-2-1	1.5404	1.54109	0.0004
200	3.189	3.20735	0.006
001	2.867	2.87887	0.004
400	1.590	1.60367	0.009
220	1.5468	1.54602	0.0005

The monoclinic unit cell constants, refined using UnitCell software are:  $a = 19.9\pm 0.06$  Å,  $b = 3.52\pm 0.01$  Å,  $c = 8.9\pm 0.1$  Å; with  $\alpha = \gamma = 90^\circ$ , and  $\beta = 160.9\pm 0.7^\circ$ . The refined unit cell volume is  $V = 203\pm 12$  Å<sup>3</sup>.

## Indexed Diffraction Pattern – Monoclinic Cell

An example for 2.74 GPa pressure point is shown below:

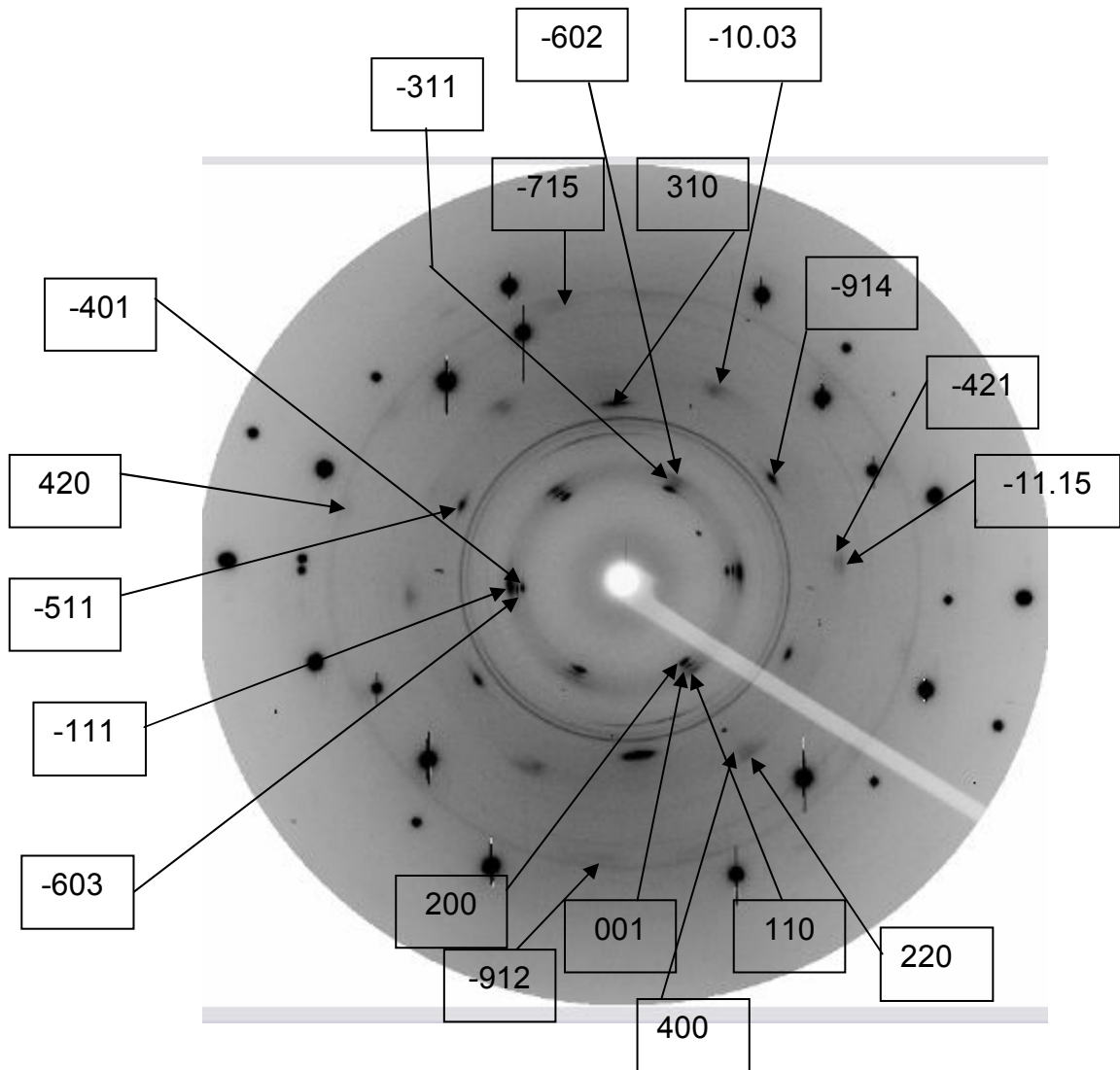


Figure 42. CCD image of diffraction pattern of Dy crystal in the DAC at 2.74GPa with all but two observed peaks (peak before -311 indexed peak and peak above image of the beam stop, next to the last diffraction ring recorded) indexed in Jade. The peak indices are indicated by arrows and displayed in text boxes. The centrosymmetric peaks (Fridel's pairs) are assumed to have  $-h-k-l$  indices, which are not labeled on the diffraction image to allow for visual clarity.

## Conclusions

All flux-grown Dy crystals studied in these experiments were twinned crystals. The principal type of all of these twinned crystals is known as transformation twins. Transformation twinning occurs when a preexisting crystal undergoes a transformation due to a change in pressure or temperature. This commonly occurs when, for the same crystal, different crystal structures and different symmetry exist at different temperatures or pressures, i.e. when the crystal is exhibiting polymorphism. The changes in temperature or pressure at which a new crystal structure and symmetry are stable, arrange different parts of the crystal in different symmetrical orientations, and thus form an intergrowth of one or more crystals. A crystal that is grown at a high temperature, upon cooling, undergoes a change from a higher to a lower symmetry structure. For example, twinning in quartz commonly forms this way during a decrease in temperature [15]. In the case of the Dy crystal indexed in this experiment, the polymorphism was observed for a change in temperature and pressure. The crystal twinned upon cooling from the flux growth temperature to ambient temperature (hcp twinning) and twinned again as the pressure in a DAC was increased (hcp -> distorted Sm-type cell, monoclinic distortion). If a crystal is subjected to different pressures and temperatures, the arrangement of atoms depends on the sizes of the atoms, and the sizes change with temperature and pressure. In general, as pressure increases, the volume of a crystal will decrease and a point may be reached where a more compact crystal structure is more stable. The crystal structure will then change to that of the more stable structure. Similarly, if the

temperature is increased, the atoms on the crystal structure will tend to vibrate more and increase their effective sizes. In this case, a point may be reached where a less compact crystal structure is more stable.

From the diffraction patterns collected in these experiments, for example Figure 34, page 72, it could be observed that the majority of diffraction spots are doublets or triplets, which is result of two or three reciprocal lattices for the twins not overlapping, due to different orientations. Twins with diffraction patterns characterized by multiple reflection spots are described as having twin lattice quasi-symmetry, TLQS [15]. Using manual indexing, one of the twin components was indexed in pseudo-hexagonal metric. For the twin lattice, which is the lattice with the smallest unit cell that is common to all individuals of the twin, semi-automatic indexing in Jade based on Sm-type unit cell was attempted. By lowering the space group R-3m symmetry, space group number 166, to space group C 1 2/m 1 symmetry, space group number 12, the monoclinic, **b**-axis unique, unit cell that allowed for indexing of the twin lattice reflections was found.

#### Pseudo – Hexagonal Lattice

Assuming the atoms to be hard spheres, the axial ratio  $c/a$  for a normal hexagonal close-packed (hcp) structure should be 1.633. Reported ambient phase unit cell constants of Dy [27], give an axial ratio of 1.573. From the present experimental pseudo-hexagonal ambient phase unit cell constants, an axial ratio of 1.54 is calculated. The hexagonal lattice is referred to as pseudo because of observation of monoclinic distortion near ambient pressure diffraction data, as discussed in the following section. The hcp rare earth metals, for

example: Sc ( $c/a = 1.594$ ), Y ( $c/a = 1.571$ ), Gd ( $c/a = 1.590$ ), Tb ( $c/a = 1.581$ ), Ho ( $c/a = 1.570$ ), and Lu ( $c/a = 1.585$ ) all have axial ratio values below a normal one, implying asymmetric unit cell atoms [27]. The lowering of the axial ratio is a consequence of the significantly smaller metallic radii of atoms lying along the  $c$ -axis, as opposed to the radii of the atoms lying in the unit cell basal plane [27]. The deviation of the experimental axial ratio from a normal hcp axial ratio indicates that the experimental pseudo-hexagonal lattice is a distorted structure, where distortion was due to temperature induced twinning. The plot of  $c/a$  ratio vs. pressure (P), given in Figure 43 below, indicates that around 2 GPa pressure point the sharp axial ratio decrease occurs to values as low as 1.46, the decrease being a result of pressure induced twinning.

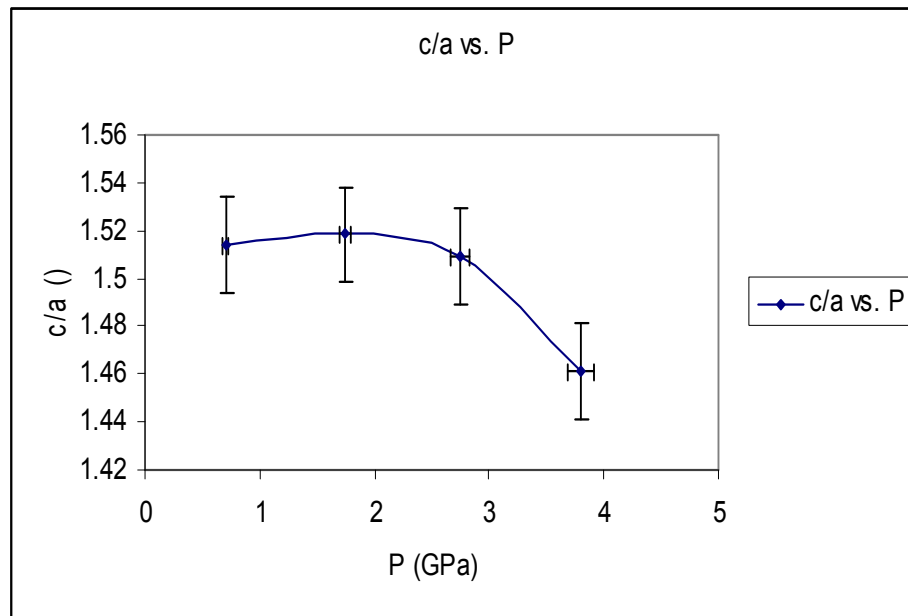


Figure 43. Plot of  $c/a$  vs. P for pseudo-hexagonal unit cell with the accompanying errors in  $c/a$  and P. The line through the points is drawn as a visual guide.



As was noted in CHAPTER 3, examining multi-crystalline diffraction patterns for the 6-9 GPa pressure range did not yield a conclusive result in respect to the first reported (Sm-type) high pressure phase of Dy [25]. So to investigate for a possible existence of a phase transition, the plot of evolution of the  $a$  and  $c$ -axes with pressure for the pseudo-hexagonal cell (given in Figure 44, below) is analyzed.

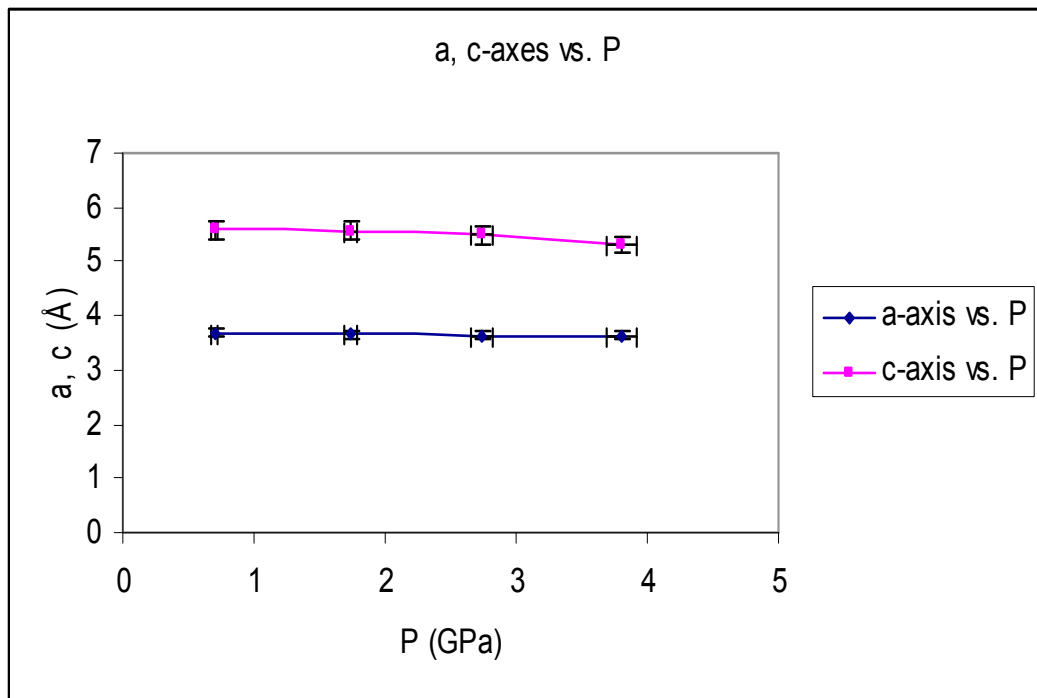


Figure 44. Plot of  $a$ ,  $c$ -axes vs.  $P$  for the pseudo-hexagonal unit cell with the accompanying errors in  $a$ ,  $c$ -axes and  $P$ .

Extending both curves from the plot to their intersection gives a possible phase transition around 10 GPa, which is larger than the pressure range of about 7 GPa reported for the first high-pressure phase transition [25].

Strain is induced during flux Dy crystal growth, as a crystal passes through phase change and twins. This strain, in turn, could influence the kinetics of the phase transitions, causing discrepancies in reported and experimentally observed phase transition pressure. Also, the disagreement observed is not unusual because a single crystal sample can act differently from powder samples, for example due to a single crystal being disordered. Thus the phase transition reported in powder diffraction data may or may not be observed in a single crystal diffraction case for the same sample and same pressure range. For example, Monazite [3, 13] in the same pressure range has different phase transitions for powder and single crystal X-ray diffraction.

To obtain bulk modulus, the pressure-volume data for the pseudo-hexagonal cell is fitted using the 3<sup>rd</sup> order Birch-Murnaghan (BM3) [32] and Vinet [33] EOS. The BM3 EOS fit to experimental pressure-volume (p-V) data, is presented in Figure 45, next page. Here, only the BM3 EOS fit is displayed, as curves for both EOS fits, once overlaid, are visually indistinguishable. Also, as an inset in Figure 45 the experimental p-V BM3 EOS fit in comparison to a few reported fits is given.

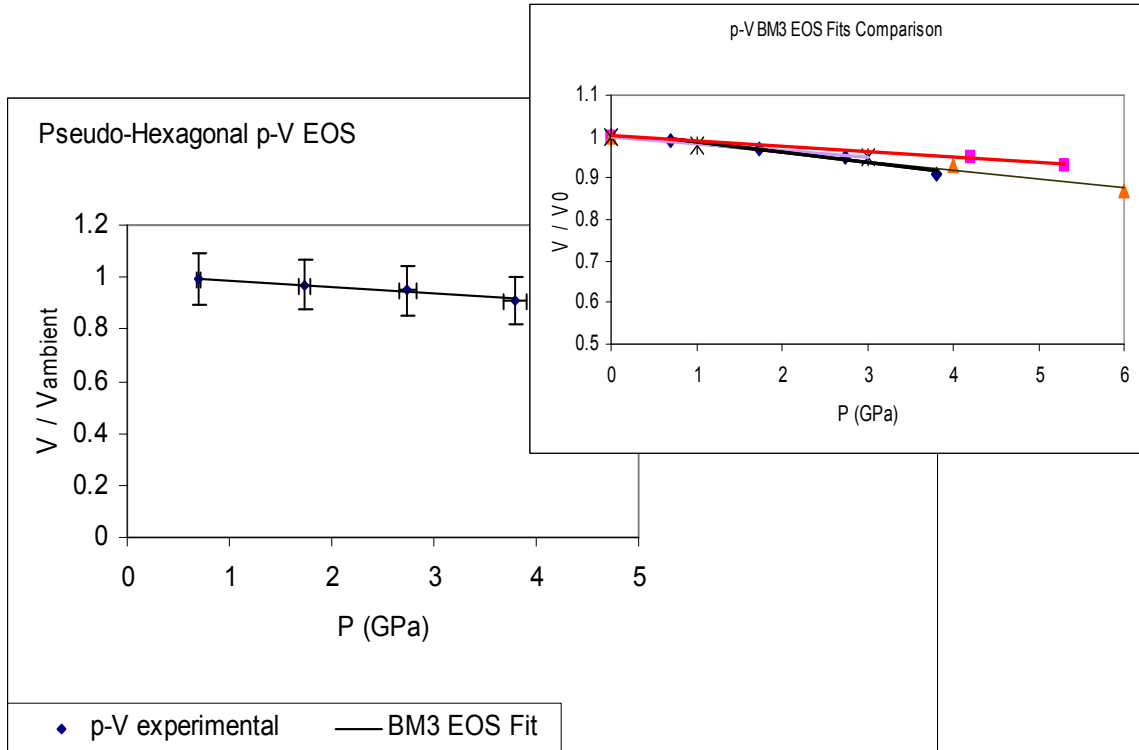


Figure 45. Pressure-volume data fitted with the BM3 EOS for the pseudo-hexagonal cell. The  $V$  - axis is normalized with  $V_{\text{ambient}}$  obtained from EOS fit. The right-hand corner inset shows reported BM3 EOS p-V fits up to 6 GPa in comparison to the experimental fit indicated by a black curve. The reported fits are: fit from [25] indicated by a red curve, fit from [34] indicated by an olive green curve, and fit from [26] indicated by a lavender curve.

The least squares fit was done in EOS-FIT software [35] and for pseudo-hexagonal cell the BM3 EOS yielded a bulk modulus value of  $K = 45 \pm 6$  GPa and a pressure derivative  $K' = 3.09 \pm 0.05$  with ambient pressure volume  $V = 66 \pm 7 \text{ \AA}^3$ . The Vinet EOS fit yielded a bulk modulus value of  $K = 41.5 \pm 5$  GPa and a pressure derivative  $K' = 3.15 \pm 0.06$  with ambient pressure volume  $V = 66 \pm 7 \text{ \AA}^3$ . This is in agreement (within a larger experimentally obtained uncertainty in  $V$  of  $\sim 10\%$ ) with a reported [34] bulk modulus value for Dy of  $K = 40$  GPa with  $K' = 2.9$  and reported [27] ambient pressure  $V = 63.0447 \text{ \AA}^3$ .

## Monoclinic Lattice

To investigate possible signs of phase transition in the twinned lattice, the evolution of  $a$ ,  $b$ ,  $c$ -axes with pressure is plotted in Figure 46, below, as well as the evolution of  $\beta$  angle with pressure in Figure 47, below Figure 46.

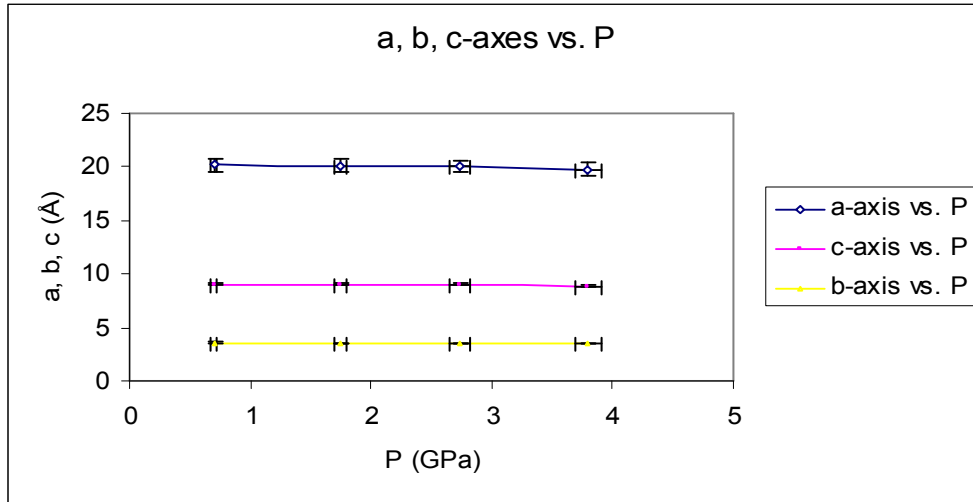


Figure 46. Plot of  $a$ ,  $b$ ,  $c$ -axes vs.  $P$  for monoclinic unit cell with the accompanying errors in  $a$ ,  $b$ ,  $c$ -axes and  $P$ .

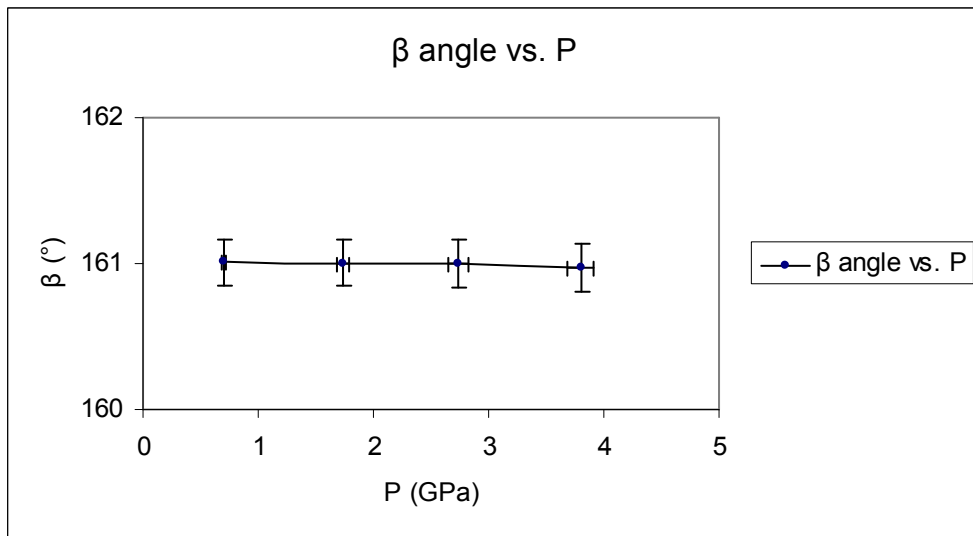


Figure 47. Plot of  $\beta$  angle vs.  $P$  for monoclinic unit cell with the accompanying errors in  $a$ ,  $\beta$  angle and  $P$ .

Because of the observed general trend in the plot in Figure 46; almost identical slopes due to parallel correlation in  $a$ ,  $b$ ,  $c$ -axes vs.  $P$  curves, the extrapolation does not indicate any upcoming symmetry distortion due to a phase change. Also, although the cell axes and  $\beta$  angle are evolving under the compression in plots from Figure 46 and Figure 47 respectively, their corresponding minimal rate of change is indicating static regime of behavior for unit cell volume. Manifestation of these experimental trends would imply that either the symmetry of the unit cell or the refined unit cell constants are incorrect. Because the continuous phase transition for the  $R-3m$  and  $C 1 2/m 1$  space groups, indicated by twinning of diffraction patterns reflections, has been verified with established group-subgroup relationship, the monoclinic unit cell constants and the  $\beta$  angle values are presumed to be not entirely correct. Most likely,  $\beta$  angle values evolving under pressure are underestimated. This is an artifact of using diffraction reflections  $d$ -spacings for indexing instead of reciprocal space vectors. Therefore, the indexing in GSE and RSV software of a recently collected set of Dy single crystal X-ray diffraction data will be attempted in the near future. Preliminary indexing done, under Prof. O. Tschauner's direction, for a couple of pressure points indicate greater monoclinic unit cell constants and  $\beta$  angle values than the ones found from diffraction peaks indexing done in Jade.

The bulk modulus of the monoclinic cell is found from fitting the pressure-volume data to the 3<sup>rd</sup> order Birch-Murnaghan (BM3) [32] and Vinet [33] EOS. The BM3 EOS fit to experimental  $p$ - $V$  data, along with the reported BM3 EOS fit

[25] are presented in Figure 48, below. For the same reasons as in the case of pseudo-hexagonal cell EOS fit, only the BM3 EOS fit is displayed.

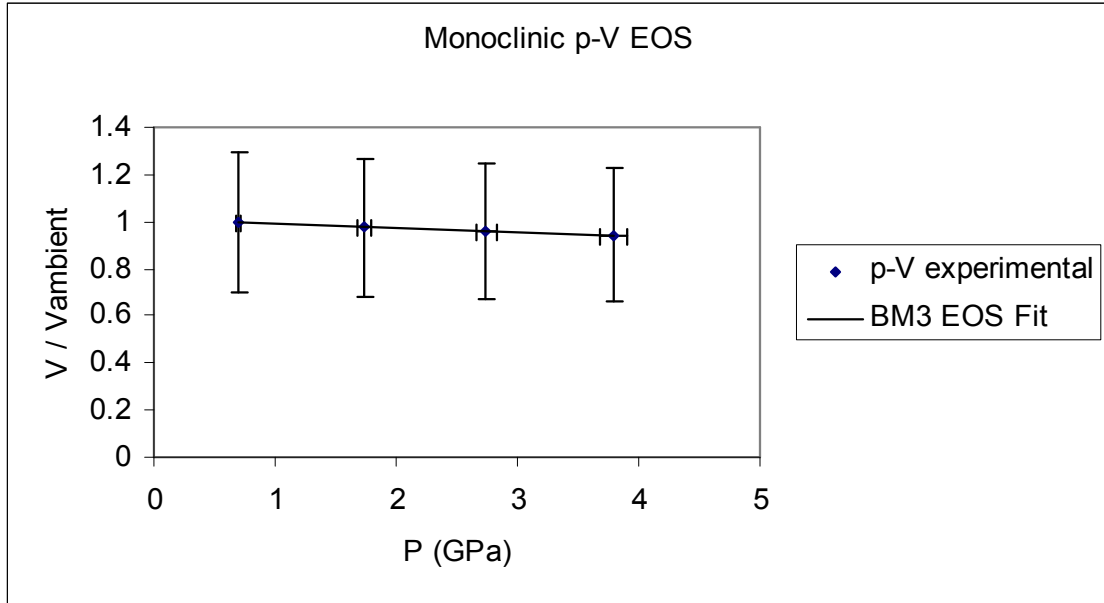


Figure 48. Pressure-volume data fitted with the BM3 EOS for the monoclinic cell. The V - axis is normalized with  $V_{\text{ambient}}$  obtained from EOS fit.

For the monoclinic lattice the BM3 EOS least squares fit done in EOS-FIT software [35] yielded:  $K = 74.2 \pm 7$  GPa,  $K' = 6.7 \pm 0.3$ , and ambient pressure  $V = 215 \pm 21$  Å<sup>3</sup>. While the Vinet EOS fit gave:  $K = 77.48 \pm 9$  GPa,  $K' = 7.1 \pm 0.7$ , and ambient pressure  $V = 215 \pm 23$  Å<sup>3</sup>. No comparison to reported data is presented due to insufficient p-V points statistics from [31] (only data for two p-V points are available: at ambient pressure and 7.5 GPa).

## Summary

The experimental work done in this thesis was subject to a considerable amount of uncertainty due to the necessary need to use the twinned or multi-crystal Dy samples. Although meticulous care was taken to pick flux grown Dy crystals that would be the best to use in a diffraction experiment, no crystal that was picked and tested in the X-ray beam had good quality. It was noted that, in general, the crystals grown and tested in the X-ray beam belonged to three main groups: twinned, multi-crystals, or crystals with finely granulated texture present on the crystal faces. The twinned and multi-crystals samples always exhibited, under visual inspection, uniform luster and well-defined faces. These crystals were, also, of the right size, measuring anywhere from 20 to 50  $\mu\text{m}$ , for use in single crystal X-ray diffraction experiments conducted by the author. The crystals with granulated texture were too big to use in the experiments, measuring anywhere from 100 to 500  $\mu\text{m}$  in size. These crystals grew into thin platelets and exhibited a powder diffraction pattern. Therefore, the most important direction for undertaking future work, would be to grow better crystals.

The development of a crystal depends on the relative rates of nucleation and growth (for metals usually rapid re-crystallization takes place at temperature above  $\frac{2}{3}$  of melting temperature) [15]. If the rate of nucleation is larger than the rate of growth, the result will be agglomerates of small crystallites. Also, a rate of growth that is too rapid may result in the inclusion of many faults in the crystal. Avoiding these problems is not straightforward, as once the initial single crystal growth is attempted, no prediction in advance could be formulated to describe

necessary relative rates of nucleation and growth that would induce good quality crystal development. Growing a single crystal of any element or compound requires a method of trial and error, with continuous refinement between attempts. One way of approaching the development of the single crystal growth method for Dy crystals in the future, would be to start from the current batch of crystals grown and use it as a seed for consequent growth, either with different type of fluxes or using another method altogether, like zone melting.

From everything written so far, one could conclude that growing a good single crystal is, in essence, more art than science. Thus, parallel to attempts in Dy single crystal growth another course of action could be explored. That would be to use a four-circle single-crystal diffractometer (the geometry of the diffractometer set-up is referred to in CHAPTER 2). Because the axes of rotations of  $\omega$ ,  $2\theta$ ,  $\varphi$ , and  $\chi$  diffractometer circles intersect within a sphere of error with a radius  $< 10 \mu\text{m}$ , a smaller crystal specimen in a DAC can be centered accurately in a point focus X-ray beam using computer controlled four-circle geometry. The precise centering and orienting on the diffractometer dictates accuracy of both the unit cell constants and the subsequent intensity measurement of the diffraction peaks of a crystal. The intensities of diffraction reflections are recorded with a point detector, which could be either a scintillation or a proportional counter. The detector is driven by  $2\theta$  circle allowing for surveying crystal diffraction reflections in reciprocal space point by point and recording of full and accurate individual reflection widths. Also, it is possible, using a diffractometer, to search for the reflections belonging to a single



reciprocal lattice and to sort out its corresponding orientation matrix for a single crystal of the multi-crystal structure [36]. And even in the case of twinned crystals, the diffraction pattern could be collected and resolved using the PILATUS detector [37], which is an area detector operating in a single-photon counting mode.

Currently at the UNLV X-ray laboratory there is a four-circle single-crystal diffractometer set-up under development. The author of this thesis is one of the members of the group (referred to as “we”) that includes Dr. David Schiferl and Prof. Oliver Tschauer that has been working on setting up the diffractometer in an operational and user friendly mode. Up to this point, we have assembled the diffractometer, as well as the vacuum system that will be used in oven annealing of the samples. The vacuum system with the oven has been tested and is ready to use. The X-ray source, a fine focus X-ray tube, which has a point focus beam with a high brilliance allowing for work with small samples inside the DAC, has been ordered from Inel, France. The author has developed in .NET suite, a programming environment that is interfacing and run-implementing crystal centering and diffraction peaks search algorithms, which were coded in QBasic programming language by Dr. Schiferl. This .NET environment has been tested and ready to interface with the diffractometer. The author has also provided a software control for the Omega temperature controllers, which has been tested and is available for implementing in oven annealing. The next task involves interfacing, via graphic user interface, diffractometer hardware, like micro stepper

motors, detector and temperature controllers into a PC controlled and robustly monitored system.

## REFERENCES

- [1] F. H. Spedding and A. H. Daane, *The Rare Earths* (John Wiley and Sons, Inc., New York and London, 1990).
- [2] J. W. Stewart, *The World of High Pressure* (D. Van Nostrand Company, Inc., Princeton, New Jersey, 1989).
- [3] W. M. Temmerman, Z. Szotek, and W. Winter, *Phys. Rev. B*, 47, 1184 (1993).
- [4] D. A. Young, *Phase Diagrams of the Elements* (University of California Press, Berkely, CA, 1991).
- [5] P. Soderlind, O. Eriksson, B. Johansson, J. M. Willis, and A. M. Boring, *Nature* (London) 374, 524 (1995).
- [6] *Lecture Notes in Physics: Critical Phenomena*, edited by J. Brey and R. B. Jones (Springer-Verlag Berlin-Heidelberg, Germany, 1976).
- [7] B. Johansson, *Journal of Alloys and Compounds* 223, 211 (1995).
- [8] O. K. Andersen, *Phys. Rev. B* 12, 3060 (1975).
- [9] J. C. Duthie and D. G. Pettifor, *Phys. Rev. Lett.* 38, 564 (1976).
- [10] U. Benedict, *Journal of Alloy and Compounds* 193, 88 (1993).
- [11] K. A. Gschneidner, Jr., *Journal of Alloys and Compounds* 1110, 165 (2003).
- [12] F. S. Galasso, *Structure and Properties of Inorganic Solids* (Pergamon Press, New York, NY, 1970).
- [13] V. E. Bean, *Physica* 139, 739 (1986).
- [14] K. Syassen, *High Pressure Research* Vol. 28, No. 2, June 2008.
- [15] Edited by C. Giacovazzo, *Fundamentals of Crystallography, Second Edition* (Oxford University Press, Oxford and New York, 2002).
- [16] <http://www.almax-industries.com/Boehler-Almax.html>.
- [17] J. G. Piermarini, S. Block, J. D. Barnett, R. A. Forman, *J. Appl. Phys.* 46, 2774 (1975).
- [18] S. R. Mulcahy, the UNLV Electron Microanalysis and Imaging Lab.
- [19] N. C. Cunningham, N. Vasiljevic, and Y. K. Vohra, *Phys. Rev. B* 71, 012108 (2005).
- [20] B. J. Baer, H. Cynn, V. Iota, and C-S. Yoo, *Phys. Rev. B* 67, 134115 (2003).
- [21] Private conversation with the APS beam line scientist, Stanislav Sinogeikin.
- [22] C. Hammond, *The Basics of Crystallography and Diffraction* (Oxford Science Publications, Oxford, 1998).
- [23] A. P. Hammersley, FIT2D V 10.9 Reference Manual V 4.7, 2003.
- [24] W. Kraus and G. Nolze, PowderCell V. 2.4, 2000.
- [25] Y. R. Shen, R. S. Kumar, A. L. Cornelius, and M. F. Nicol, *Phys. Rev. B* 75, 064109 (2007).
- [26] P. W. Bridgman, *Proc. Am. Acad. Arts Sci.*, 84, 112 (1955).
- [27] F. H. Spedding, A. H. Daane, and K. W. Herrmann, *Acta Cryst.* 9, 559, (1956).
- [28] International Tables for X-Ray Crystallography, Volume II, IUCr, 1991.
- [29] University of Bilbao, Spain, Bilbao Crystallographic Server, <http://www.cryst.ehu.es>, 2000.
- [30] Tim Holland and Simon Redfern, UnitCell, 2006.

- [31] E. Yu. Tonkov, I. L. Aptekar', V. F. Degtareva, and Yu. I. Krasavin, Doklady Akademii Nauk SSSR 230, 85, (1976).
- [32] F. Birch, J. Geophys. Res. 57, (1952).
- [33] P. Vinet, J. Ferrante, J. H. Rose, and J. R. Smith, J. Geophys. Res. 92, (1987).
- [34] W. A. Grosshans and W. B. Holzapfel, Phys. Rev. B 45, 5171 (1992).
- [35] R. J. Angel, EOS-FIT V5.2, 2001.
- [36] D. Schiferl, D. T. Cromer, L. A. Schwalbe, and R. L. Mills, Acta Crystallogr., B39, (1983).
- [37] Paul Scherrer Institut, Zurich, <http://pilatus.web.psi.ch/pilatus.htm>, 2009.

VITA

Graduate College  
University of Nevada, Las Vegas

Ognjen Grubor-Urošević

Degrees:

Bachelor of Science, Physics, 2004  
Purdue University Calumet, Hammond

Thesis Title: X-Ray Diffraction Study of Dysprosium (Dy) Single Crystal Samples  
in a Diamond Anvil Cell (DAC)

Thesis Examination Committee:

Chairperson Lon Spight, Ph. D.  
Chairperson Oliver Tschauner, Ph. D.  
Committee Member, Stephen Lepp, Ph. D.  
Committee Member, David Schiferl, Ph. D.  
Graduate Faculty Representative, Clemens Heske, Ph. D.